Max Planck Graduate Center
mit der Johannes Gutenberg-Universität

Disassembly of IM30 higher-order oligomeric structures enables phase separation

Dissertation zur Erlangung des Grades

„Doktor rerum naturalium“ (Dr. rer. nat.)

der Fachbereiche:

08 - Physik, Mathematik und Informatik,

09 - Chemie, Pharmazie und Geowissenschaften,

10 – Biologie und der

Universitätsmedizin

der Johannes Gutenberg-Universität Mainz

JG|U
JOHANNES GUTENBERG
UNIVERSITÄT MAINZ

Ndjali Quarta

geb. in Leipzig

Mainz, 2024

D77

1. Gutachter: [redacted]

2. Gutachter: [redacted]

Tag der mündlichen Prüfung:

I hereby declare that I wrote the dissertation submitted without any unauthorized external assistance and used only sources acknowledged in the work. All textual passages which are appropriated verbatim or para-phrased from published and unpublished texts as well as all information obtained from oral sources are duly indicated and listed in accordance with bibliographical rules. In carrying out this research, I complied with the rules of standard scientific practice as formulated in the statutes of Johannes Gutenberg-University Mainz to insure standard scientific practice.

Table of contents

with a little help from my family and friends

Table of contents

I. Table of contents

II. Summary

Cyanobacteria are the most ancient oxygenic photosynthetic organisms that can convert the energy from the sun into biochemical energy. The protein complexes that are involved in the light-driven reactions are embedded in a specialized internal membrane system, the thylakoid membrane (TM). For the most part, biogenesis and maintenance of the TM system remains mysterious, yet clearly involves the *inner membrane associated protein of 30 kDa* (IM30). IM30 belongs to a superfamily of proteins, all members of which form large homo oligomeric structures and are involved in membrane remodeling.

First, the structural changes upon disassembly of oligomeric IM30 structures at increasing urea concentrations were investigated. To follow the unfolding process on different levels, we applied static light scattering, tryptophane fluorescence spectroscopy, circular dichroism spectroscopy together with molecular dynamics simulations. By developing and applying a 3-state model for IM30 oligomer disassembly we could show that IM30 remains structured in its conserved coiled-coil region after barrel disassembly while the rest of the protein already unfolds.

In the next section of this thesis, we show that disassembly of higher ordered oligomers enables IM30 to form biomolecular condensates in vitro. Furthermore, IM30 variant that is deficient in the formation of prototypical higher order oligomers still accumulated into so called *punctae* in living cells an. These *punctae*, which appear to be important for the *in vivo* function of IM30, likely represent IM30 condensates forming *in vivo*.

In the last section of this thesis, the interconnections between truncated IM30 variants and their ability to form condensates *in vitro* and *punctae in vivo* was investigated. We found that the structured coiled-coil region, but not an intrinsically disordered region, drives condensate formation of IM30, and the N-terminal coiled-coil-containing region in fact is also sufficient for *puncta* formation *in vivo*.

III. Zusammenfassung

Cyanobakterien sind oxygen photosynthetisch aktive Organismen, welche die Energie der Sonne in biochemische Energie umwandeln können. Die Proteinkomplexe, die an den licht-abhängigen Reaktionen der Photosynthese beteiligt sind, sind in ein spezielles internes Membransystem, der Thylakoidmembran (TM), eingebettet. Obwohl noch immer unklar ist, wie genau TMs gebildet und/oder in Stand gehalten werden, so scheint doch das *Innere-Membran Protein von 30 kDa* (IM30) an diesen Prozessen essenziell beteiligt zu sein. IM30 gehört zu einer Superfamilie von Proteinen, deren Vertreter alle große homo oligomere Strukturen bilden und an der Umgestaltung interner Membranen beteiligt sind.

Zuerst wurden die strukturellen Änderungen bei der Disassemblierung von oligomeren IM30 Strukturen bei steigenden Harnstoff-Konzentrationen untersucht. Mittels statischer Lichtstreuung, Tryptophanfluoreszenz-Spektroskopie, Circulardichroismus-Spektroskopie und Molekular-dynamiksimulationen wurde der Entfaltungsprozess verfolgt. Mit Hilfe eines 3-Stufen-Modells für die Disassemblierung von IM30-Oligomeren konnten wir zeigen, dass IM30 die Struktur innerhalb der konservierten „coiled-coil“ Region stabil bleibt, während der Rest des Proteins entfaltet und die homo-oligomeren Strukturen disassemblieren.

Im nächsten Abschnitt der Arbeit zeigen wir, dass die Disassemblierung von höher geordneten IM30-Oligomeren dazu führt, dass IM30 *in vitro* biomolekulare Kondensate bildet. Außerdem konnten wir in *in vivo*-Untersuchungen zeigen, dass eine IM30-Variante, die keine prototypischen höher geordneten Oligomere mehr bildet, trotzdem *punctae* in lebenden Zellen bildet, Strukturen, welche als wichtig für die *in vivo* Funktion von IM30 betrachtet werden.

Im letzten Abschnitt beschreibe ich Untersuchungen zum Zusammenhang zwischen verkürzten IM30-Varianten und deren Fähigkeit zur Bildung von Kondensaten (*in vitro*) und punctae (*in vivo*). Wir konnten zeigen, dass die strukturierte “coiled-coil”-Region, nicht aber eine intrinsisch ungeordnete Region, die Kondensatbildung von IM30 antreibt, und dass die N-terminale “coiled-coil”-Region tatsächlich auch für die Bildung von *punctae in vivo* ausreichend ist.

1. Introduction

1.1 Cyanobacteria as model organisms for studying photosynthesis

Cyanobacteria are the oldest oxygen producers on earth[1–3]. Early cyanobacteria evolved on land occupying terrestrial and freshwater habitats[4–6]. They initiated the first great oxygenation event (GOE) where oxygen levels on earth increased for the first time and thus had an enormous impact on the biogeochemical cyle[7]. The rise of marine cyanobacteria in the open ocean led to the second oxygen event that eventually resulted in a much higher increase in atmospheric oxygen levels and resulted in the oxygen in the atmosphere that we breathe[8]. Cyanobacteria occupied fresh- and seawater as well as terrestrial habitats[5] and evolved to endure even harsh environments such as hot and cold deserts[9,10]. Phytoplankton in the ocean accounts for about half of the photosynthetic net primary production from carbon dioxide[11], with 10% contributed by cyanobacteria[12]. Today, cyanobacteria are discussed and investigated for biotechnological applications[13].

The endosymbiotic theory involves endosymbiotic incorporation of an α-proteobacterium into an archaeal cell with the acquisition of eukaryotic feature being debated to have occurred either after or prior to these events[14,15]. A mitochondrion-containing eukaryote was the host for a cyanobacterium that became the origin of plastids and this primary endosymbiotic event led to the common ancestor of red algae, glaucophyte algae, and green algae, which later evolved to land plants [14,15]. Because of this shared origin, the knowledge acquired by studying cyanobacteria is often applied to chloroplasts of higher plants.

The first completely sequenced genome of a photoautotroph organism was that of the cyanobacterial strain *Synechocystis* PCC 6803, made available by the Kazusa DNA Research Institute[16]. *Synechocystis* PCC 6803, hereafter referred to as *Synechocystis*, can grow heterotrophically in presence of glucose[17–19], is naturally competent [20], and can incorporate exogenous desoxyribonucleic acid (DNA) into its genome by heterologous recombination[18,20]. Due to these traits *Synechocystis* has become a model organism for the study of oxygenic

photosynthesis in laboratories all over the world. A schematic representation of a *Synechocystis* cell is shown in **Figure 1.1-1**.

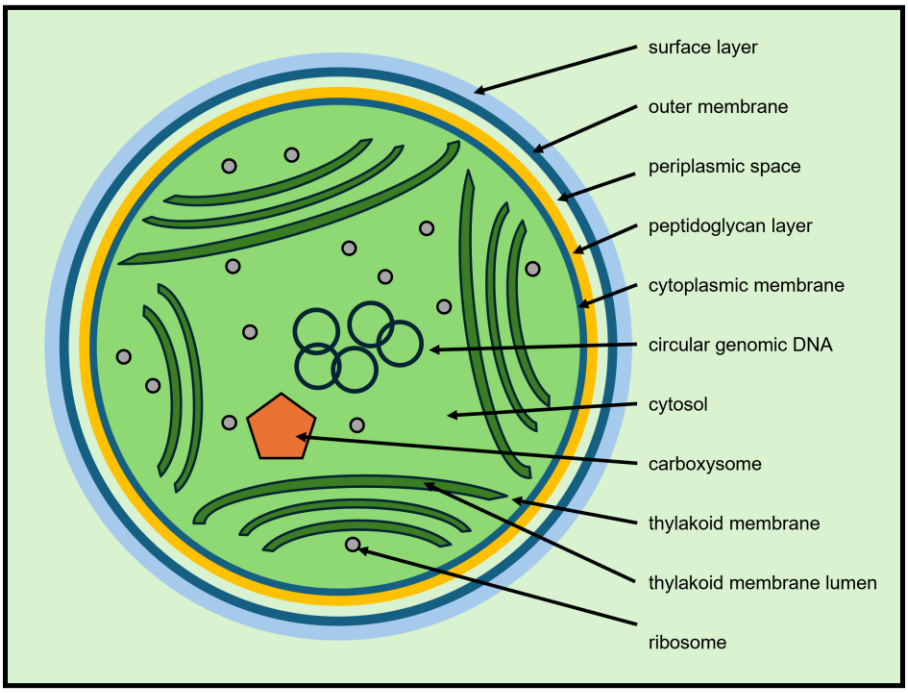

***Figure 1.1-1**: Schematic representation of the Synechocystis cell. The cyanobacterial cell is surrounded by the surface layer on top of the outer membrane followed by the periplasmic space, which is separated from the cytoplasm by the plasmamembrane on top of which sits the peptidoglycan layer. In the cytosol are shown the ribosomes, a carboxysome, the genomic DNA and the thylakoid membranes encapsulating the thylakoid lumen.*

Synechocystis contains multiple copies of their circular DNA[21], which is why DNA that is transformed into naturally competent *Synechocystis* cells requires multiple generations under selective pressure for the incorporation of the new DNA into all genomic copies. This process is then called complete segregation as opposed to partial segregation where at least a single original genome copy is retained due to insufficient selection pressure or nonviable cells after complete incorporation of the introduced genetic changes.

The cytoplasm of a *Synechocystis* cell is surrounded by the cytoplasmic membrane, followed by the peptidoglycan layer, the outer membrane, and in some cases the surface-layer (S-layer)[22]. Large molecular assemblies located in the cytoplasm are lipid bodies, phosphate bodies, cyanophycin granules, ribosomes and carboxysomes.

Carboxysomes are icosahedral proteinaceous compartments. They are found in CO_2 fixing bacteria as part of their CO_2 concentrating mechanism (CCM)[12]. The outside of carboxysomes consists of a protein shell that is selectively permeable for HCO_3^- but retains CO_2 inside[23]. The inner lumen contains carbonic anhydrase (CA) and RuBisCO (ribulose-1,5-bisphosphate carboxylase/oxygenase), which perform the enzymatic reactions needed for carbon fixation[24,25]. This colocalization is required for efficient photosynthetic carbon fixation and reduces oxygenation in favor of carboxylation[26]. The biogenesis of carboxysomes involves the formation of pre-carboxysome condensates[27] through phase separation, a process which will be described in section 1.1.2. This results in a concentration of CA and RuBisCO into pre-carboxysome condensates. Changes from a reducing environment in the cytosol to an oxygenic environment in late condensates results in redox regulation of the RuBisCO small subunit-like (SSUL) domain, demixing of protein components, and encapsulation of CA and RuBisCO within the protein shell[28]. In line with that, it should be mentioned here that the corresponding matrix of the CCM in eukaryotes, the pyrenoid, also involves phase separation of RuBisCO to enhance carboxylation and even undergoes a reversible phase transition during cell division[29].

The high efficiency of oxygenic photosynthesis and its widespread evolutionary success is linked to another cyanobacterial advancement, the thylakoid membrane (TM).

1.1.1. Cyanobacterial thylakoid membranes

TMs enable larger membrane area, and thus more space for the photosynthetic machinery, per cell, resulting in enhanced photosynthetic efficiency. The exception to the rule is presented by the cyanobacterium *Gloeobacter violaceus*, which does not contain any TMs[30] and instead harbors the protein complexes needed for photosynthesis in the CM resulting in very low photosynthetic activity compared to other cyanobacteria, and thus highlighting the importance of a TM system for efficient photosynthesis[31]. TMs form a separate intracytoplasmic membrane system that is disconnected from the plasma membrane[32,33]. Cyanobacteria across different species organize their TMs in diverse types of spatial arrangements including parietal, fascicular, radial, parallel, and irregular arrangements as well as combinations thereof[34]. Cyanobacterial TMs contain the protein complexes for both oxygenic photosynthesis and respiration[35,36]. A schematic representation of a cyanobacterial TM is shown in **Figure 1.1-2**.

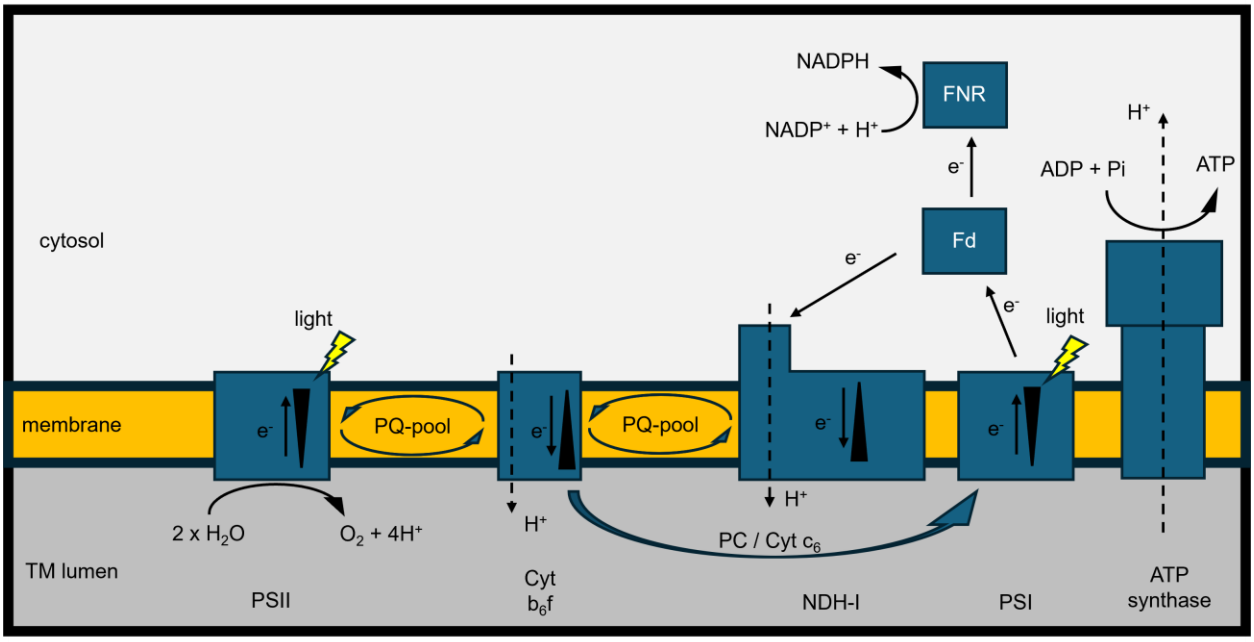

***Figure 1.1-2**: Schematic representation of a TM. PSII – photosystem II, PQ-pool – plastoquinone-pool, Cyt b_6f – cytochrome c_6, PC – plastocyanin, Cyt c_6 – cytochrome c_6, NDH-I – type-I NADPH-plastoquinone oxidoreductase, PSI – photosystem I, Fd – Ferredoxin, FNR – ferredoxin-NADP⁺ oxidoreductase. e^- alongside black triangles with arrows pointing up and down indicate the electrons being transferred up and down the energy gradient in the electron transfer chain, respectively. Dotted lines indicate the transfer of H^+ between cytosol and TM lumen.*

The light-dependent reaction involves water splitting at Photosystem II (PSII) to provide high energy electrons that are transferred from PSII, to quinone molecules (Q_A and Q_B), where reduced

Q_B gets released into the plastoquinone (PQ) pool in the TM. These hydrophobic electron carriers diffuse inside the TM and pass electrons to the membrane-integral cytochrome b_6f complex (Cyt b_6f), which subsequently transfers the electrons onto the electron carrier plastocyanin (PC) or cytochrome c_6 (Cyt c_6). PC and Cyt b_6f are water-soluble electron carriers that are located inside the thylakoid lumen and transport the electrons to PSI. There the electrons are excited again and transferred from PSI to ferredoxin (Fd) and finally to ferredoxin-$NADP^+$ oxidoreductase (FNR) resulting in reduction of the $NADP^+$ to NADPH. Electron transfer along the energy gradient generates an electrochemical gradient across the TM in the accumulation of protons in the TM lumen. This proton gradient is called the proton motive force (PMF) which is used by the ATP synthase to produce ATP[37]. The light-dependent electron transfer chain that starts at PSII is called the linear electron flow (LEF) and the water-splitting reaction which produces O_2 defines this type of photosynthesis as oxygenic. The generated energy in the form of NADPH and ATP is used to produce sugar in the Calvin-Benson-Bassham (CBB) cycle and results in recycled $NADP^+$ that is needed for continuous light-dependent reactions to take place[37]. Therefore, the processes that consume and produce NADPH depend on each other and the ratio of NADPH to ATP output is important for optimal photosynthetic performance and therefore regulated by additional pathways[38]. Cyclic electron flow (CEF) around PSI produces ATP without net reduction of $NADP^+$ and represents one way to balance the NADPH to ATP output[39,40]. Further regulation of photosynthesis is achieved by regulating the light-driven processes at the photosystems through their associated light-harvesting complexes. Cyanobacteria use special soluble light-harvesting complexes, called phycobilisomes, which contain light-capturing phycobilins, and function as light antennae that channel their excitation energy to the reaction center of PSI and PSII[41]. The PQ pool functions as a trigger for state transition, where phycobilisomes are coupled to PSII (state I transition) by oxidation of the PQ pool or decoupled from PSII (state II transition) by reduction of the PQ pool[42]. Components of the respiratory electron transport in the TM that can add to the reduction of the PQ pool are type-I NAD(P)H dehydrogenase (NDH-I) and succinate dehydrogenase (SDH), whereas cytochrome oxidase can oxidize the PC pool[37,41].

Despite the efforts to balance and control the photosynthetic reaction acceptor-site and donor-site photoinhibition of PSII can occur, which, in turn, increases the production of harmful reactive oxygen species (ROS) and leads to damaged PSII[43]. The repair PSII cycle, mainly for the PSII sub-unit D1, requires partial disassembly of PSII, exchange of damaged against newly synthesized

D1 and reassembly into PSII[43]. Key components of the PSII repair cycle and *de novo* biogenesis of PSII were localized in the CM in a study based on separation of membrane compartments by fractionation[44]. This led to an ongoing debate on how the exchange between the TM and the CM is realized[43,45,46]. Studies have shown that there is no evidence for a direct connection between TM and CM [32,33,47], Other studies reported on an additional membrane fraction containing the PSII assembly factor PratA, termed PratA-defined membrane (PDM), and suggested PDMs to form some type of connection or facilitate exchange between the TM and CM[45,48]. Finally, through advanced fractionation techniques it was shown that most PSII assembly factors are indeed localized in the TM, apart from PratA, which was suggested to require some kind of dynamic interaction between TM and CM[49]. However, the biogenesis and maintenance of the TM remains poorly understood and is still under investigation[50–53].

Both TM remodeling during cell division or adaptation to changing light conditions and biogenesis of new TMs, *e. g*. after nitrogen chlorosis[54], requires extensive membrane remodeling, including membrane fusion and fission. Examples for proteins in *Synechocystis* that were shown to have membrane remodeling activity *in vitro* are *Syn*IM30[55] , which will be introduced in section 1.2, *Syn*CurT, important for generating membrane curvature in TMs[56] and *Syn*DLP[57,] a bacterial member of the Dynamin-like protein family. However, not all cellular compartments rely on having a lipid membrane as discussed earlier for carboxysomes. Biomolecular condensates represent such membraneless compartments.

1.1.2. (Bacterial) membraneless organelles and the formation of biomolecular condensates

Membraneless organelles (MLOs) or biomolecular condensates are cellular compartments with specific functions which include and exclude molecules without a membrane[58,59]. They can be thought of as initially liquid droplets of varying viscoelastic properties that can fuse, dissolve, wet surfaces, and transition into more gel-like blobs or solid filaments on different timescales. Interactions between proteins, nucleic acids, and other molecules can lead to condensate formation. Different terms and combinations thereof are used to differentiate the mechanism by which biomolecular condensates can form, *e. g.* liquid-liquid phase separation (LLPS)[60], complex coacervation[61], and phase separation coupled to percolation (PSCP) [62,63]. To describe *in vitro* or *in vivo* observations without preliminary knowledge on the underlying mechanisms of their formation,

the simplified term “condensate” will henceforth be used in this study as a phenomenological description.

Protein LLPS was initially used to describe the phase transition of proteins above a critical saturation concentration, c_{sat}, that results in two liquid-like phases, *i. e.* a dense phase with high protein concentration and a dilute phase with low protein concentration[60]. However, the cellular environment itself and the formed condensates are not simple fluids and have viscoelastic properties[64,65]. Therefore, the term “liquid-liquid” has become misleading, resembling water-like fluidity in both phases, and should be avoided to describe complex biomolecular condensates[62]. Another mechanism describing condensate formation is the phase separation driven by complex coacervation. This process is driven by the electrostatic attraction between charged molecules or charged patches on a polymer and oppositely charged polymers or multivalent counterions[61]. A more recent description for condensate formation is PSCP[62,63], where multivalent interactions still drive phase separation at concentrations above c_{sat}, but additionally a network is formed inside the condensates, where the concentration has crossed the critical concentration for percolation, c_{perc}, and thus only occurs when $c_{perc} > c_{sat}$. In cases were $c_{perc} < c_{sat}$ the system would immediately undergo percolation and form gel without phase separation[63]. In contrast to classical complex coacervation, the multivalent interactions can be mediated by domains or motifs that are not limited to electrostatic interactions and can include hydrophobic, cation-π and π-π interactions as well as hydrogen-bonds and are summarized as stickers. These stickers are separated by non-interacting linkers to provide multivalency to the polymer and control the fluidity and solubility of the condensate[63,66]. In phase transitions driven by percolation, pre-percolation clusters can form below the c_{perc}, in contrast to phase separation where phase-separating macromolecules do not cluster below c_{sat}[62]. To summarize these mechanisms, phase separation++ (PS++) was introduced to describe phase separation that can be coupled to other phase transitions as in PSCP[62].

The requirement for transient multivalent interactions for reversible phase transitions makes intrinsically disordered region and proteins (IDRs/IDPs) inherently potent drivers and modulators for condensate formation[59,67,68]. These regions convey sequence-specific functions that can involve many-to-one and one-to-many binding[69], disorder-to-order transisiton[70], entropic springs[71], and many others by representing an ensemble of structures rather than taking a predefined structure[68].

Many important concepts for condensate formation and IDPs have been developed in polymer science and are now being increasingly applied to biological systems. Demands by life science researchers on the complexity of systems of biomolecular condensates pose new challenges for polymer scientists and stimulate interdisciplinary cooperations. Biomolecular condensates have become recognized as important organizers of cellular processes and the focus of research in life science during the last decades has shifted towards contributing to a profound understanding of their *in vivo* functions.

Many eukaryotic biomolecular condensates have been identified since the first description of P-granules[72], *e. g.* stress granules formed by the RNA-binding protein fused in sarcoma (FUS)[73], postsynaptic[74] and presynaptic[75] condensates near the membrane, the nuclear complex that acts as a selective barrier for molecules into and out of the nucleus[76], and even secondary condensates inside condensates as observed for nucleoli[77]. Condensate formation has also been described for membrane bound receptors, where the phase transition compared an order of magnitude lower in compared to condensates formed in solution[78]. Theoretical studies outlined the implications of membrane binding on prewetting transitions and possibility of condensate formation at membranes occurring prior to condensate formation in solution[79].

Bacterial biomolecular condensates present difficulties for experimental studies *in vivo* due to the smaller size of bacterial compared to eukaryotic cells and the diffraction limit of the light that is commonly used to visualize and probe the dynamic properties of condensates[80,81].

Examples of biomolecular condensates in bacteria include ATP-dependent biomolecular condensates[80,82], GTP-dependent reversible transitions between FtsZ-SlmA-SBS condensates and FtsZ-polymerization[83], bacterial RNP-bodies related to mRNA degradation with similar functions to eukaryotic stress granules[84], and the previously describe condensation during the assembly of carboxysomes[27,85]. Recent examples for the importance of condensate formation in cyanobacteria are condensation of the DEAD-box RNA helicase in response to abiotic stress[86] and the report on reversible phase transitions in response to the daily cycle[87].

The importance of biomolecular condensates for the spatiotemporal organization of processes inside bacteria is increasingly being recognized[81,88,89] and additional bacterial biomolecular condensates are likely to be identified soon.

1.2 The inner-membrane associated protein of 30 kDa

1.2.1. Discovery, mutant phenotypes, and origin of IM30

The *inner-membrane associated protein of 30 kDa* (IM30), also known as *vesicle-inducing protein in plastids 1* (VIPP1), was first described in plastids of pea where it occurred in clusters near the inner envelope membrane and the TM[90]. In *Arabidopsis thaliana im30* knock-down strains showed no vesicle budding from the inner envelope accompanied by the inhibition of TM formation[91], whereas *im30* knock-out strains showed complete absence of TMs [92] and both mutants were not viable outside of special growth medium after the seedling stage[92]. However, in the green algae *Chlamydomonas reinhardtii im30* mutants were still viable but had severely reduced concentrations of photosynthetic components and increased sensitivity against high light stress[93]. An attempted knock-out of *im30* in *Synechocystis* showed that cells did not segregate completely, retaining at least one functional copy of the IM30-coding gene, and loss of TM formation was observed[94]. This indicated that *im30* is essential in plants and in *Synechocystis*. The IM30 protein seemed to be crucially involved in the biogenesis and maintenance of TMs. In this study we will use the term IM30 synonymously with the *Syn*IM30 protein encoded in *Synechocystis* by the *sll0617* gene and references to IM30 proteins from other organisms will be explicitly indicated. Early studies already identified phage shock protein A (PspA) as potential predecessor and suggested IM30 evolved from PspA via gene duplication[95]. Structural models from our group and others now showed that both IM30 and PspA belong to the endosomal sorting complexes required for transport (ESCRT) - III superfamily of membrane remodeling proteins[96–98].

1.2.2. Structure of IM30

The IM30 protein takes an ESCRT-III like fold composed of helices α0-6, with helices α2 and α3 forming a single extended helix, and helix α5 connecting to a potential helix α6 by an extended flexible linker[96]. IM30 homo-oligomerizes spontaneously in solution into large barrel structures with varying point-symmetries, whereof C14 to C18 symmetries have been resolved in high resolution structures. Monomers of IM30 form point-symmetrical rings which stack into 6 (C14-C16) or 7 (C17, C18) layers of varying diameter. The middle layers have the largest diameter, whereas the topmost layer has smallest diameter giving the barrel structure a dome-like shape. The inside of the barrel is lined horizontally with the amphipathic helix α0 and the hydrophobic surfaces are facing the barrel lumen to mediate membrane interactions. The outside of the barrel shows the hairpin tips, formed by the closed end of the coiled-coil between α1 and α2, protruding

from the surface and forming a conserved interaction interface with α5, which is seen as horizontally aligned spikes. The C-terminal linker and putative α6 are not resolved in the model and probably cover the outside of the barrel. Across the different layers exists structural flexibility within the monomer to accommodate for the varying ring diameters and barrel sizes. This flexibility is enabled by 3 conserved hinge regions, named shoulder (between α2 and α3), elbow (linker region between α4 and α5) and wrist (linker region between α4 and α5) in accordance with ESCRT-III nomenclature[96,97,99]. Additionally, the N-terminal region of α5 in the topmost layer becomes part of the C-terminal region of helix α5 in lower layers. The presence of ADP bound between this flexible region in α4/α5 of layer 1 and positively charged residues in the coiled-coil from layer 2 revealed a previously unreported type of nucleotide binding-site of unknown function[96].

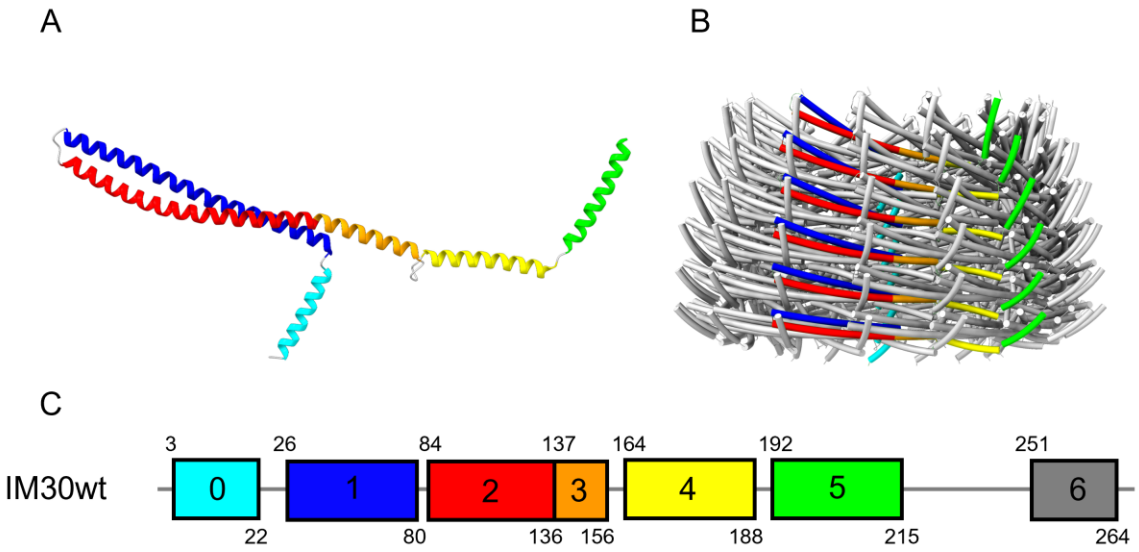

***Figure 1.2-1**: Structure of the IM30 protein. (A) Monomer structure of IM30 in layer 3 in cartoon representation with helices colored as in (C). (B) Barrel structure of C16 IM30 barrel shown in tube representation with helices of a single stack of IM30 monomers colored as in (C). (C) Helix definition for helices α0-6 of IM30 used in this study. Helices are represented by boxes with individual colors and helix numbers are specified inside the boxes. Amino acid positions indicating the beginning of the helix are shown at the top left corner of the box and the position of the last amino acid of each helix is marked at the bottom right corner of each box.*

There are several other ESCRT-like proteins that are being identified in relation to the recent structural classification of IM30 and PspA as bacterial ESCRT-III proteins[96–98] and due to the possibility to rapidly visualize and compare tertiary structures using AlphaFold models[100]. These proteins include the ESCRT-II like protein VIA1 of *Arabidopsis thaliana* (VPL3 in

Chlamydomonas reinhardtii) that is only found in the green lineage[101], the VPL2 protein of *Chlamydomonas reinhardtii* with an ESCRT-III-like hairpin only conserved in Chlorophyceae[50,101], and a protein of unknown function encoded by s*ll0162* in *Synechocystis*, which belongs to the TIGR04376 family, which is restricted to cyanobacteria[102] and also contains characteristic features of ESCRT-III proteins like the coiled-coil according to its AlphaFold model[103].

1.2.3. Function of IM30

IM30 has been proposed to occupy a dual function in maintenance and remodeling of TMs. In absence of Mg^{2+} IM30 forms carpet-like structures on lipid membranes and stabilizes membranes against proton leakage[104]. It was shown that Mg^{2+} triggered structural changes that led to the exposure of additional hydrophobic surfaces[105] and resulted in IM30-mediated membrane fusion *in vitro*[106]. Studies involving IM30 from *Synechocystis*, as well as from *Arabidopsis thaliana*[92] and *Chlamydomonas reinhardtii*[93] showed characteristic formation of *punctae*. In this study the term "*puncta"* will be used to refer to an accumulation of signal from fluorescently labeled proteins into distinct, approximately circular regions within the cell or chloroplast that are observed via fluorescence microscopy. Experiments using temporally controlled cytosolic trapping of IM30 indicated the necessity for dynamic formation and/or localization of *punctae* near the TM *in vivo*[107]. A recent study employing spatiotemporal control over induced photodamage in the cyanobacterium *Synechococcus sp. PCC 7002* expressing fluorescently labeled IM30 suggested accumulation of IM30 at sites of membrane-bound chlorophyll-a photo-damage, but not membrane-associated phycobilin photo-damage, via an unknown mechanism.[108]

To improve our understanding of the functions of IM30, increased effort needs to be made to determine the extent to which IM30 forms and participates in different supramolecular assemblies *in vivo*.

1.3 Objectives of this thesis

Previous studies had indicated that homo-oligomeric IM30 disassemble on membrane surfaces, and this disassembly process involves unfolding of a large part of the protein. In my studies I analyzed changes of the IM30 structure and a role of protein regions in the formation of IM30 assemblies different from the prototypical IM30 barrel structures.

The aims of my study can be summarized as follows:

1. Investigate the structural changes that follow upon disassembly of IM30 barrels.

   Understanding oligomer disassembly helps to understanding the reassembly and possible rearrangements of IM30 barrels. These barrels can be disassembled by the introduction of mutations in intermolecular conserved interfaces, but little is known about the disassembly of the wildtype IM30 protein. Therefore, we investigated destabilization of IM30 barrels by urea and followed structural changes via spectroscopic methods.

2. Investigate the ability of IM30 to phase separate.

   Many IDPs have been reported to drive and/or modulate phase separation. Therefore, when IM30 was found to largely unfold upon disassembly of large, homo-oligomeric barrel structures, the question arose whether the IDR in IM30 trigger phase separation (in vitro and/or in vivo). To answer this question, my first aim was to find out whether IM30 phase separates at all.

3. Identify regions of IM30 that drive phase separation.

   After establishing that IM30 can phase separate we wanted to understand the interactions that are important for this phase transition. Therefore, we next tested truncated IM30 variants to test our hypothesis that the extended IDR drives phase separation in IM30. We found that it is not essential for IM30 phase transition that is driven by its coiled-coil region, but instead modulates it.

4. Discuss the physiologically relevance of phase separation for IM30.

   This study focuses on the physiological relevance of observations made *in vitro* and discusses important aspects and potential functions of IM30 biomolecular condensates *in vivo*. Therefore, we investigated IM30 condensate formation at physiologically important parameters. We

identified the conserved structured coiled-coil region as the force driving phase separation *in vitro* as well as *in vivo*.

5. Compare observations made *in vitro* for phase separation and *in vivo* studies on protein localization

Different structural IM30 ensembles may have distinct function *in vivo*. Via analyzing mutated proteins as well as truncated IM30 variants that show differences in the ability to form defined assemblies, such as barrels, carpets and/or condensates, *in vitro* effects and impaired *in vivo* functions can (eventually) be aligned. Therefore, we investigated the ability of different truncated IM30 variants to form condensates *in vitro* and related the observation to observations made *in vivo* upon expressing truncated proteins in intact cells.

2. Materials and Methods

2.1 Materials

2.1.1. Chemicals and consumables

All chemicals and consumables were purchased from AppliChem GmbH (Darmstadt, Germany), Bio-Rad (Munich, Germany), Bruker (Billerica, MA, USA), Merck (Darmstadt, Germany), New England Biolabs (Frankfurt, Germany), Roth (Karlsruhe, Germany), Sarstedt (Nürnberg, Germany), Thermo Fisher Scientific (Waltham, MA, USA), and VWR International GmbH (Darmstadt, Germany). Lipids were purchased from Avanti Polar Lipids, Inc (Alabaster, AL, USA) and fluorescently labeled PEG was purchased from Biopharma PEG Scientific Inc. (Watertown, MA,USA).

2.1.2. Buffers and solutions

Table 2.1.2-1*: Buffers and solutions*

Protein purification and assay buffers	
Notation	Composition
HEPES buffer	20 mM HEPES pH 7.6 (NaOH)
Purification buffer	20 mM imidazole 300 mM NaCl 50 mM phosphate pH 7.6 (NaOH)
Elution buffer	500 mM imidazole 300 mM NaCl 50 mM phosphate pH 7.6 (NaOH)
Phase separation buffer	10 mM phosphate 10 mM HEPES pH value as indicated in the description with or without 100 mM NaCl, 10% (w/v) PEG-8000, and/or 3 M urea as indicated in the description

PEG-NaCl buffer	20 mM HEPES
	10 % (w/v) PEG-8000
	NaCl as indicated in the description
	pH 7.6 (NaOH)
SDS PAGE	
Stacking gel buffer	1.5 M Tris
	0.4% (w/v) SDS
	pH 6.8
Separation gel buffer	0.5 M Tris
	0.4% (w/v) SDS
	pH 8.8
10X SDS running buffer	0.25 M TRIS
	1.92 M Glycine
	1% (w/v) SDS
	pH 8.3
5X SDS sample buffer	0.25 M Tris
	10% (w/v) SDS
	0.2% Bromophenol blue
	50% (v/v) Glycerol
	0.5 M DTT
Coomassie staining solution	0.125% (w/v) Coomassie Brilliant Blue G-250
	40% (v/v) Ethanol
	2% (v/v) Phosphoric acid
Coomassie destaining solution	30% (v/v) Ethanol
	2% (v/v) Phosphoric acid
Agarose gel electrophoresis	
TAE	40 mM Tris
	1 mM EDTA
	20 mM acetic acid
	pH 8.3
6X loading buffer	50% (v/v) Glycerol

	0.2% (w/v) Bromophenol blue
	0.2% (w/v) Xylene cyanole
Gibbson assembly	
5x isothermal reaction mix	500 mM Tris
	50 mM $MgCl_2$
	1 mM dNTP mix
	250 mg/ml PEG-8000
	5 mM NAD^+
	pH 7.5
1.33x Gibson assembly master	26.67% (v/v) 5x isothermal reaction mix
	25 U/ml Phusion DNA polymerase
	4 U/ml T5 exonuclease
	4 U/ml Taq DNA ligase
AFM buffers	
Adsorption buffer	20 mM HEPES
	20 mM $MgCl_2$
	pH 7.6 (NaOH)

2.1.3. Media and bacterial strains

Table 2.1.3-1*: Media*

Notation	**Composition**
LB medium	10 g/l Tryptone
	5 g/l Yeast extract
	10 g/l NaCl
LB agar	1.5% (w/v) agar in LB medium
1000X Trace minerals	46.3 mM boric acid
	9.1 mM $MnCl_2 \cdot 4\ H_2O$
	0.77 mM $ZnCl_2 \cdot 7\ H_2O$
	1.6 mM $Na_2MoO_4 \cdot 2\ H_2O$

	0.32 mM $Co(NO_3)_2 \cdot 6\ H_2O$
	0.17 mM $CuSO_4$ x 5 H_2O
	3.1 mM citric acid
	24.5 mM $CaCl_2 \cdot 2\ H_2O$
	30.4 mM $MgSO_4 \cdot 7\ H_2O$
	0.28 mM $Na_2EDTA \cdot 2\ H_2O$
BG11 medium	5 mM HEPES, pH 8.2
	1X Trace minerals
	1X BG-FPC
	22.6 µM ferric ammonium citrate
	0.19 mM Na_2CO_3
	0.175 mM K_2HPO_4
BG11 agar	12.1 mM Na2S2O3 · 5 H2O
	15 g/l BD Difco Bacto agar in BG11 medium

Table 2.1.3-2*: Bacterial strains*

Bacterial strain	**Genotype**	**Origin**
Escherichia Coli		
E. Coli XL1 blue	recA1 endA1 gyrA96 thi-1 hsdR17 supE44 relA1 lac	Agilent Technologies (Santa Clara, CA, USA)
E. Coli BL21 (DE3)	F-ompT hsdSB (rB- mB-) gal dcm lon λ (DE3)	Novagen (Darmstadt, Germany)
Synechocystis sp. PCC 6803		
Synechocystis	wt	Conrad Mullineaux (London, UK)
pCK306 IM30-7GS-mVenus	Δsll0410::rhaBAD IM30-7GS-mVenus Km^R rhaS	This work
pCK306 IM30*-7GS-mVenus	Δsll0410::rhaBAD IM30*-7GS-mVenus Km^R rhaS	This work

pCK306 IM30$_{1-156}$-7GS-mVenus	Δsll0410::rhaBAD IM30$_{1-156}$-7GS-mVenus Km^R rhaS	This work
pCK306 IM30$_{157-267}$-7GS-mVenus	Δsll0410::rhaBAD IM30$_{157-267}$-7GS-mVenus Km^R rhaS	This work
pCK306 IM30$_{26-156}$-7GS-mVenus	Δsll0410::rhaBAD IM30$_{26-156}$-7GS-mVenus Km^R rhaS	This work
pCK306 IM30$_{26-136}$-7GS-mVenus	Δsll0410::rhaBAD IM30$_{26-136}$-7GS-mVenus Km^R rhaS	This work
pCK306 mVenus	Δsll0410::rhaBAD mVenus Km^R rhaS	This work
pCK306 7GS-mVenus	Δsll0410::rhaBAD 7GS-mVenus Km^R rhaS	This work

2.1.4. Plasmids and oligonucleotides

Table 2.1.4-1*: Plasmids*

Plasmid	Resistance	Origin
pRSET IM30	Amp^R	Schneider group
pRSET IM30*	Amp^R	Schneider group (BJ)
pRSET IM30$_{1-156}$	Amp^R	This work
pRSET IM30$_{157-267}$	Amp^R	Schneider group (BJ)
pRSET IM30$_{26-156}$	Amp^R	Schneider group (LS)
pRSET IM30$_{26-136}$	Amp^R	This work
pRSET IM30-Venus	Amp^R	Schneider group (JH)
pRSET IM30-7GS-mVenus	Amp^R	This work
pRSET IM30*-7GS-mVenus	Amp^R	This work
pCK306	Km^R	(Kelly et al. 2018)
pCK306 IM30-7GS-mVenus	Km^R	This work
pCK306 IM30*-7GS-mVenus	Km^R	This work
pCK306 IM30$_{1-156}$-7GS-mVenus	Km^R	This work
pCK306 IM30$_{157-267}$-7GS-mVenus	Km^R	This work

pCK306 IM30$_{26-156}$-7GS-mVenus	Km^R	This work
pCK306 IM30$_{26-136}$-7GS-mVenus	Km^R	This work
pCK306 mVenus	Km^R	This work
pCK306 7GS-mVenus	Km^R	This work

***Table 2.1.4-2**: Oligonucleotides*

Oligonucleotide	**Sequence (5'→ 3')**	**Application**
Gibson_pCK306_LP_fw	ggatccaaagccacgttgtgtctc	Gibbson assembly; generate linearized plasmid backbone
Gibson_pCK306_LP_reverse	ttctacctcctttgtatattataaacttacccgattc	Gibbson assembly; generate linearized plasmid backbone
Gibbson LP rev pCK306 7GS	AGATCCACTTCCTCCGGATCCCATttctacctcctttgtatattataaacttacccgattc	Gibbson assembly; generate linearized plasmid backbone
SLIC LP1 pRSET fw	ggatccggctgctaacaaagccc	Gibbson assembly; generate linearized plasmid backbone
SLIC LP2 pRSET rev	atgcttgtcgtcgtcgtcgatatgg	Gibbson assembly; generate linearized plasmid backbone
SLIC 157 H4 fw pRSET	ccatatcgacgacgacgacaagcatgggggcttaggtactag	Gibbson assembly; generate gene of interest
SLIC H7 rev pRSET	GGGCTTTGTTAGCAGCCGGATCCTTACAGATTATTTAACCGACGAC	Gibbson assembly; generate gene of interest
SLIC (h4-7) CFP pRSET rev	gggctttgttagcagccggatccttattgaattcccttgtacagc	Gibbson assembly; generate gene of interest
SLIC (H7) YFP pRSET rev	gggctttgttagcagccggatccttacttgtacagctcgtcca	Gibbson assembly; generate gene of interest
Gibson_7GS-XFP_fw	GGATCCGGAGGAAGTGGATCTGTGAGCAAGGGCGAGGA	Gibbson assembly; generate gene of interest

pRSET IM30 (136)-end to LP rev	GGGCTTTGTTAGCAGCCG GATCCttatttcttggttttagcttcgg	Gibbson assembly; generate gene of interest
Gibbson IM30 (136) 7GS rev	GGGCTTTGTTAGCAGCCG GATCCttatttcttggttttagcttcgg	Gibbson assembly; generate gene of interest
Gibbson XFP pCK306 fw	tttataatatacaaaggaggtagaaATG GTGAGCAAGGGCGAGGA	Gibbson assembly; generate gene of interest
Gibson_IM30H1-3(156)_7GSlinker_rev	AGATCCACTTCCTCCGGA TCCGAGGGTTTGCTGCAG TTCAGC	Gibbson assembly; generate gene of interest
Gibson_pCK306_IM30_H4_fw	tttataatatacaaaggaggtagaaATG GGGGGCTTAGGTACTAGC AGTGC	Gibbson assembly; generate gene of interest
Gibson_IM30_H7_7GS-linker_rev	AGATCCACTTCCTCCGGA TCCCAGATTATTTAACCG ACGACG	Gibbson assembly; generate gene of interest
QC_156 H3 Stop_fw	GCAGCAAACCCTCTAAGG CTTAGGTACTAGC	QuickChange; G157Stop
QC_156 H3 Stop_rev	GCTAGTACCTAAGCCTTA GAGGGTTTGCTGC	QuickChange; G157Stop
Gibson_F_pCK306_IM30_start26	tttataatatacaaaggaggtagaaATG GAAAAAGTTCTGGAACAG GCCG	Gibbson assembly; generate gene of interest
QC-mYFP_fw	CCTGAGCTACCAGTCCAA ACTGAGCAAAGACCCCAA CG	QuickChange; A206K in Venus to generate mVenus
QC-mYFP_rev	CGTTGGGGTCTTTGCTCA GTTTGGACTGGTAGCTCA GG	QuickChange; A206K in Venus to generate mVenus
f-hom-left-pCK306	ggcaggtattctggcta	segregation-check
r-hom-right-pCK306	gcaccaaggtggtaatt	segregation-check

2.1.5. Kits, enzymes, and marker

Kits were used by following the instructions in the accompanying manuals and any deviations are indicated in the following methods section.

***Table 2.1.5-1**: Kits*

Kit	Manufacturer
Agarose gel extraction NucleoSpin, Gel and PCR cleanup Kit	Machery Nagel, Düren, GER
Plasmid preparation NucleoSpin, Plasmid Kit	Machery Nagel, Düren, GER
Bradford reagent	Bio-Rad (Munich, Germany)

***Table 2.1.5-2**: Enzymes*

Enzyme	
DpnI restriction endonuclease	New England Biolabs (Frankfurt, Germany)
Phusion DNA polymerase	New England Biolabs (Frankfurt, Germany)
Q5 DNA polymerase	New England Biolabs (Frankfurt, Germany)
T5 exonuclease	New England Biolabs (Frankfurt, Germany)
Taq DNA Ligase	New England Biolabs (Frankfurt, Germany)

***Table 2.1.5-3**: Marker*

Marker	Manufacturer
DNA Ladder, GeneRuler 1kb	Thermo Scientific (Darmstadt, Germany)
Pierce, PageRuler unstained MW marker	Thermo Scientific (Darmstadt, Germany)

2.1.6. Instruments and software

***Table 2.1.6-1**: Instruments*

Instrument	Notation	Manufacturer

Atomic force microscope	Multimode 8 with J-scanner	Bruker (Billerica, MA, USA)
CD spectrometer	J-1500 with MTPC-490S	JASCO (Pfungstadt, Germany)
Centrifuges	Allegra X-15R	Beckmann Coulter (Krefeld, Germany)
	Avanti J-26XP with JA-25.50 and JLA-8.1 rotors	Beckmann Coulter (Krefeld, Germany)
	Centrifuge 5424	Eppendorf (Hamburg, Germany)
Fluorescence microscope	Axio Observer.Z1	Carl Zeiss (Jena, Germany)
Fluorescence spectrometer	FluoroMax-4	Horiba Scientific (Kyoto, Japan)
Gel documentation	Quantum-ST4 1100/26MX	PeqLab (Erlangen, Germany)
Gel electrophoresis chamber	Mini-Protean 3 Cell	Bio-Rad (Munich, Germany)
Gel electrophoresis power supply	PowerPac Basic	Bio-Rad (Munich, Germany)
Gel scanner	ViewPix 700	Biostep (Burkhardtsdorf, Germany)
Heating block/shaker	Thermomixer comfort	Eppendorf (Hamburg, Germany)
Heating plate/magnetic stirrer	MR Hei-Standard	Heidolph (Schwabach, Germany)
Horizontal shaker	Duomax 1030	Heidolph (Schwabach, Germany)
Incubator (*E. coli*)	Binder Inkubator Serie BF	Binder (Tuttlingen, Germany)
Incubator (*Synechocystis*)	Economic Delux, ECD01E	Snijders Scientific (Tilburg, Netherlands)
Photometer	Nanodrop 2000C	Thermo Scientific (Darmstadt, Germany)
pH meter	pH211 Microprocessor	HANNA Instruments (Vöhringen, Germany)

Plate Reader	FLUOstar Omega	BMG Labtech GmbH (Ortenberg, Germany)
Sonifier	Branson Sonifier 250	Heinemann Labortechnik, (Duderstadt, Germany)
Stopped-flow spectrometer	SX20	Applied Photophysics (Leatherhead, UK)
Thermocycler	Thermocycler TGradient 96	Biometra (Göttingen, Germany)

***Table 2.1.6-2**: Software*

Software	Version and websites	Application
Benchling	www.benchling.com	Sequence analysis
ChimeraX	1.6.1	Molecular visualization
Excel	Microsoft 365	Data analysis
FIJI / ImageJ	2.3 / 1.53q	Image analysis and editing
GIMP	2.10	Image editing
Gwyddion	2.58	AFM image and data analysis
Mendeley	1.19.8	Reference management
OriginLab 2020	9.7.0.188	Data analysis
PowerPoint	Microsoft 365	Figure editing
Word	Microsoft 365	Text editing

2.2 Methods

2.2.1. Cloning, expression, and purification of IM30

The construction of the plasmid containing the gene coding for IM30 of *Synechocystis* sp. PCC 6803 (pRSET IM30 wt) was described previously[110]. The construction of the plasmid for IM30*, containing the mutations E83A, E84A, F168A, E169A, R170A, and M171A was described earlier[104,111]. Quick changes, or site directed mutagenesis, usus an overlapping pimer pair with base pairs that are mitchmatching to the template to introduce mutations. Gibbson assembly cloning uses primers with partially overhanging regions that overlap to generate fragments with the genes

of interest and a linearized plasmid backbone that are subsequently combined and assembled in a reaction step after the PCR. The plasmid for expression of the truncated IM30 variant $IM30_{26\text{-}156}$ is based on pRSET IM30 wt and was constructed using QuickChange PCR to introduce a stop codon at the amino acid position 157 and Gibbson assembly cloning to remove the sequence coding for the first helix of *Syn*IM30 resulting in pRSET $IM30_{26\text{-}156}$ by [redacted] and kindly provided. Other plasmids and primers used in this study are listed in **Table 2.1.4-1** and **Table 2.1.4-2**. A glycine-serine linker with a length of 7 amino acids was inserted between IM30 variants and the mVenus fluorescence tag, which was shown to result in a functional fusion protein in other *in vivo* studies in Synechocystis[112].

All protein variants were expressed in *E. coli* BL21 (DE3) grown overnight in LB medium at 37 °C. Cells were harvested by centrifugation (3000 x g, 4°C), resuspended in 20 mM imidazole purification buffer (300 mM NaCl, 20 mM imidazole, 50 mM phosphate, pH 7.6) and lysed via sonification at 4 °C. Cell debris was removed by centrifugation (12000 x g, 4 °C) and His-tagged protein was bound to Ni-NTA columns and washed with increasing amounts of imidazole (20, 50, 100 mM). In the end, protein was eluted with purification buffer containing 500 mM imidazole. Buffer was exchanged using PD-10 columns or dialysis, and protein was concentrated using centrifugal filters (Merck, Darmstadt, Germany) with molecular weight cut-offs of 30 kDa for IM30wt and IM30-mVenus, 10 kDa for IM30* and IM30*-mVenus, and 3 kDa for the truncated IM30 variants $IM30_{1\text{-}156}$, $IM30_{157\text{-}267}$, $IM30_{26\text{-}156}$, and $IM30_{26\text{-}136}$. Protein concentration was determined using the Bradford test[113] using BSA as standard for the calibration curve and protein was frozen in liquid nitrogen and stored at -20 °C until use.

2.2.2. Sodium dodecyl sulfate polyacrylamide gel electrophoresis

Sodium dodecyl sulfate polyacrylamide gel electrophoresis (SDS PAGE) was used to validate the purity of the aliquoted protein samples. To this end, protein samples were mixed with SDS-buffer to get a solution of ~ 0.1 µg/ µl according to the determined protein concentration determined in the Bradford assay. Samples were then incubated at 95°C for 5 minutes. Next, SDS samples and marker samples were applied to 12 or 16 % acrylamide gels and run in a gel electrophoresis system (Bio-Rad, Munich, Germany) at 200 V for ~ 45 minutes until the dye almost reached or barely exits the bottom of the gel. Gels were subsequently washed with water, stained in Coomassie staining solution for 1 hour and excess dye was removed by at least 2 incubations for 30 minutes

in unstaining solution. Gels were scanned in a gel scanner and further processed for labeling in GIMP. The gel of an exemplary SDS-PAGE summarizing all different IM30 variants used in this study is shown in **Figure 2.2-1**.

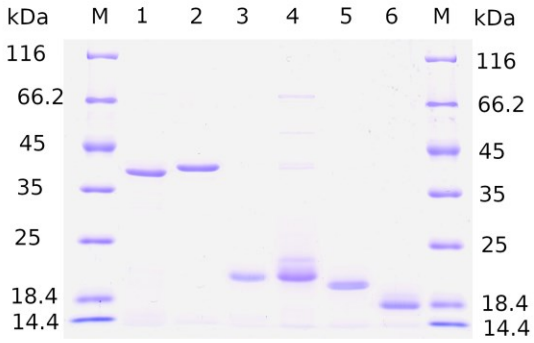

Figure 2.2-1*: Protein samples for all different IM30 variants used in this study were analyzed via SDS-PAGE after each purification. A representative gel summarizing the results for all protein variants in one gel is shown. Lanes indicated on top of the gel were loaded as follows: M - marker, 1 - IM30, 2 – IM30*, 3 - IM301-156, 4 – IM30157-267, 5 – IM3026-156 and 6 – IM3026-136. The molecular weight of the marker is indicated next to the marker bands on both sides in kDa.*

2.2.3. Agarose gel electrophoresis

Agarose gel electrophoresis was used to distinguish the sizes of PCR-products from transformed and untransformed Synechocystis cells, verify for the incorporation of the genes of interest and determine if complete or only partial segregation was achieved. Gels were prepared from 1% agarose dissolved in TAE buffer. Samples were diluted in loading dye buffer and applied to the gel together with a DNA marker (gene ruler 1 kbp). The agarose gel was run at 140 V for at least 30 minutes until the dye almost reached the end of the gel.

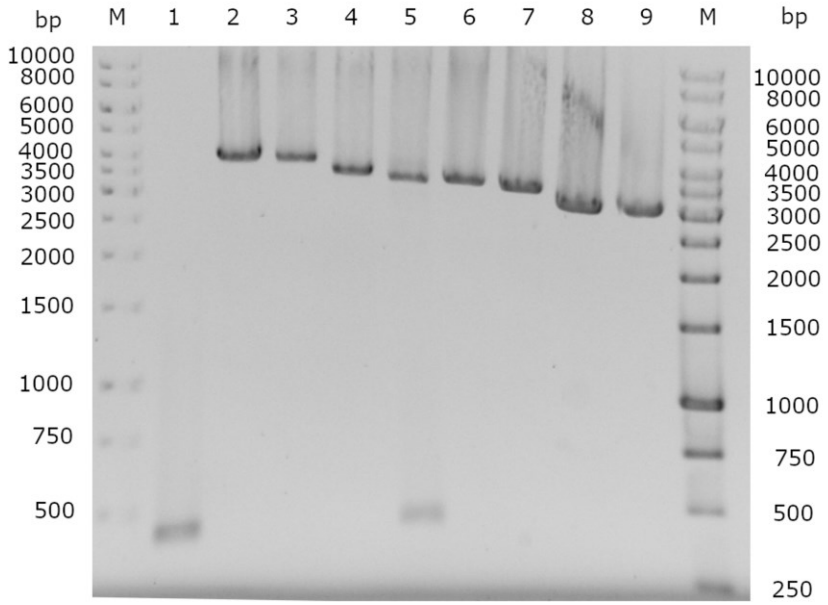

***Figure 2.2-2**: Agarose gel summarizing the PCR-check for all Synechocystis strains used in this study.Lanes indicated on top of the gel were loaded as follows: M - marker, 1 – Synechocystis wt, 2 – Synechocystis pCK306-IM30-7GS-mV, 3 – Synechocystis pCK306-IM30*-7GS-mV, 4 – Synechocystis pCK306-IM30$_{1-156}$-7GS-mV, 5 – Synechocystis pCK306-IM30$_{157-267}$-7GS-mV, 6 – Synechocystis pCK306-IM30$_{26-156}$-7GS-mV, 7 – Synechocystis pCK306-IM30$_{26-136}$-7GS-mV, 8 – Synechocystis pCK306-mV, 9 – Synechocystis pCK306-IM30-7GS-mV,. The number of base pairs(bp) of the marker DNA fragments is indicated next to the marker bands on both sides.*

Synechocystis transformed with pCK306-IM30$_{157-267}$-7GS-mVenus showed incorporation of the gene of interest but incomplete segregation. All other Synechocystis strains that were transformed with plasmids showed incorporated genes of the expected length and segregated completely. The lengths of the expected PCR fragments are listed in **Table 2.2.3-1** and the plasmids used for transformation were checked by sequencing before the transformation (Eurofins, Ebersberg, Germany).

***Table 2.2.3-1**: Expected lengths of the PCR-check fragments*

lane #	Synechocystis	expected length [bp]
1	wt	413
2	pCK306 IM30wt-7GS-mV	3917

3	pCK306 IM30*-7GS-mV	3917
4	pCK306 $IM30_{1-156}$-7GS-mV	3584
5	pCK306 $IM30_{157-267}$-7GS-mV	3452
6	pCK306 $IM30_{26-156}$-7GS-mV	3512
7	pCK306 $IM30_{26-136}$-7GS-mV	3452
8	pCK306 mV	3098
9	pCK306 7GSmV	3119

2.2.4. Static light scattering

Static light scattering was used to follow changes in IM30 particle size at urea concentrations ranging from 0 M to 7 M urea. 3.2 µM of protein were incubated for 15 minutes at 20 °C at the indicated urea concentration in 10 mM HEPES buffer pH 7.6. Scattering was measured at 20 °C using a FluoroMax fluorescence spectrometer (Horiba Scientific, Kyoto, Japan) instrument with excitation wavelength set to 600 nm, slid width 2 nm, and emission spectra were recorded from 200 to 700 nm in 1 nm steps, slid width 2 nm. Light scattering was evaluated as the 2^{nd} order Rayleigh scattering at 300 nm by measuring the average of the signal at 300 nm ± 5 nm for each urea concentration.

2.2.5. Tryptophane fluorescence measurements

Tryptophane (Trp) fluorescence was used to follow changes in Trp71 fluorescence resulting from changes in the Trp's environment at urea concentrations ranging from 0 M to 7 M urea. For each data point 3.2 µM of protein was incubated for 15 minutes at 20 °C in 10 mM HEPES buffer pH 7.6 at the indicated Urea concentration. Trp fluorescence was measured at 20 °C using a FluoroMax fluorescence spectrometer (Horiba Scientific, Kyoto, Japan) instrument with excitation wavelength set to 280 nm, slid width 1 nm, and emission spectra were recorded from 300 nm to 450 nm in 1 nm steps (slid width 3 nm). The resulting spectra were processed by applying a moving average of ± 5 nm. The fluorescence intensity at 335 nm, as well as the maximums wavelength of the spectrum were determined at each urea concentration. The Trp71 fluorescence intensity at 335 nm was normalized and both maximums wavelength and normalized intensity at 335 nm from at

least 3 independent measurements were averaged. Measurements of Trp fluorescence were performed directly after measuring the scattering signal with the same sample.

2.2.6. Circular dichroism spectroscopy

Circular dichroism (CD) spectroscopy was used to follow changes in the IM30 secondary structure at urea concentrations ranging from 0 M to 7 M urea. For each data point, 3.2 µM of protein (0.1 mg/ml for IM30 and IM30*; 0.07 mg/ml for $IM30_{26\text{-}156}$) was incubated for 30 minutes at 20 °C at the indicated urea concentration in 10 mM HEPES buffer pH 7.6. A CD-spectrum was measured at 20 °C using a J-1500 CD-spectrometer (JASCO Corporation, Tokyo, Japan) collecting spectra from 190 nm to 250 nm at a scanning speed of 100 nm/min in 1 nm steps, slid width 1 nm. The resulting spectra were processed by applying a moving average of ± 5 nm. The molar ellipticities at 208 nm and at 222 nm were normalized and the molar ellipticity ratio 222 nm to 208 nm was determined for each urea concentration. The results of at least 3 independent measurements were averaged.

2.2.7. Unfolding kinetics

The kinetics of unfolding in 4 M urea were monitored via following changes in Trp fluorescence and turbidity. To this end, 20 µM IM30 wt or IM30* in 10 mM Hepes/NaOH, pH 7.6 was rapidly mixed with 8 M urea in the same buffer in a 1:1 ratio, employing the SX20 instrument (Applied Photophysics, Leatherhead, UK). For all curves, a cut off filter at 320 nm was used on the emission side. For monitoring the change in Trp fluorescence, the excitation wavelength was set to 280 nm; for monitoring turbidity, it was set to 325 nm. For each condition, the same solution was used for measuring kinetics based on Trp fluorescence and turbidity, respectively. At least three kinetic curves were averaged for each condition. All unfolding kinetics experiments were performed and analyzed by [redacted].

2.2.8. Modelling urea-induced IM30 destabilization

We applied a three-state model for IM30 oligomer unfolding: the native state, namely the barrel (N), an intermediate monomeric state (I) and the final unfolded state (U). For IM30* and $IM30_{26\text{-}156}$ a two state model was used, with a native state (N') and unfolded state (U).

Our model is based on the linear combination of the signal Y (measured via light scattering, fluorescence and CD) from specific IM30 state, which can be expressed as:

$$Y = \sum_{i=1}^{2,3} f_i Y_i$$

Where Y_i is the maximum signal that could be produced by species i (i=N, N', I, U). For IM30 wt the first step is dissociation of the barrel, which makes a rigorous treatment difficult. However, based on the scattering signal we can estimate the overall fraction of non-oligomers, as demonstrated below, simplifying the model-based analyses:

Since the small oligomeric/monomeric states and unfolded states are indistinguishable in terms of the scattering signals ($S_I = S_U = S_{I,U}$), we find for the scattering signal of IM30:

$$S = f_N * S_N + (f_I + f_U)S_{I,U} = S_{I,U} + (S_{I,U} - 1)f_N \qquad \text{(eq. 1a)}$$

$$S_{norm} = \frac{S - S_{I,U}}{S_{I,U} - 1} = f_N \qquad \text{(eq. 1b)}$$

Thus, based on the normalized scattering data as a descriptor for the fraction of protein in the IM30 barrel state, we can replace f_N by S_{norm}, and only have to describe the denaturation process by an appropriate equilibrium constant.

The ratio between intermediate and unfolded protein can be expressed in terms of an equilibrium constant, K, as:

$$K = \frac{c_U}{c_I} = e^{-\frac{\Delta G^O}{RT}} = e^{-\frac{\Delta G^o_{H2O} - m[U]}{RT}} = e^{-\frac{C_{50} - [U]}{d}} \qquad \text{(eq.2)}$$

We used a similar method as previously described for the determination of ΔG^o_{H2O} [114] by applying the linear extrapolation model (LEM) to parametrize the effect of urea on the denaturation equilibrium constant K. Here, $C_{50} = \Delta G^o_{H2O}/m$, defining the urea concentration where K=1, and $d=RT/m$.

The fractions of smaller oligomeric/monomeric and unfolded states can then be expressed as:

$$f_I = \frac{c_I}{c_N + c_I + c_U} = \frac{1}{1+K}(1 - f_N) \quad \text{(eq.3a)}$$

and

$$f_U = K f_I = \frac{K}{1+K}(1 - f_N) \quad \text{(eq.3b)}$$

Here, c_N, c_I, c_U are the concentrations of the N, the I and the U state, and f_N, f_I, f_U the corresponding fractions of the total protein concentration.

For further analysis, we rearranged the equations describing the contributions of the different species to the fluorescence signal (F) and CD-signal (D), starting from:

$$F = f_N F_N + f_I F_I + f_U F_U \quad \text{(eq.4a)}$$

$$D = f_N D_N + f_I D_I + f_U D_U \quad \text{(eq.4b)}$$

In the next step, f_U was eliminated from eq.4a making use of $1 - f_N - f_I$, yielding

$$F = F_U + f_N (F_N - F_U) + f_I (F_I - F_U)$$

By normalizing so that at $F_N = 1$ for $f_N = 1$ we obtain:

$$F_{norm} = \frac{F - F_U}{F_N - F_U} = f_N + a f_I$$

where $a = \frac{F_I - F_U}{F_N - F_U}$.

Analogously, by eliminating f_N from eq. 4b and normalizing so that $D_{norm} = 1$ for $f_U = 1$, we get:

$$D_{norm} = b f_I + f_U$$

where $b = \frac{D_I - D_N}{D_U - D_N}$. Thus, the fit constants a and b express the differences between the specific fluorescence and CD signals. Thus, the following equations were fitted to the normalized signals simultaneously:

$$F_{norm} = S_{Norm} + a \frac{1}{1+K}(1 - S_{Norm})$$

$$D_{norm} = \frac{b+K}{1+K}(1 - S_{Norm})$$

In the cases of IM30* and $IM30_{26\text{-}156}$ we consider only two states, namely the smaller oligomeric/monomeric native state (N') and the unfolded state (U), and analogously we obtain the simplified equations:

$$F_{norm} = f_{N'} = \frac{c_{N'}}{c_{N'} + c_U} = \frac{1}{1+K}$$

and

$$D_{norm} = f_U = \frac{c_U}{c_{N'} + c_U} = \frac{K}{1+K}$$

The model was implemented in OriginLab 2020 and fitted using the Levenberg Marquard algorithm by setting all parameters as shared global fitting parameters for each respective IM30 variant. All fits converged and fit parameters are summarized in (

Suppl. table 8.1-1).

The model describing IM30 destabilization by urea was developed by [redacted].

2.2.9. Coarse-grained simulations

The simulation was run on a coarse-grained (CG) structure of the IM30 monomer. The residues in the sequence of IM30 (PDB 7O3Y) were mapped to the PLUM force field[115,116]. The PLUM represents each amino acid as three or four beads N, Cα, C' and Cβ for amide group, central carbon, carbonyl group and side chain respectively, with special consideration for Gly and Pro residues. This force field has two distinct advantages; it uses implicit solvent which allows for fast dynamics, plus has an explicit H-bond potential on the backbone.

The initial configuration of monomer for simulation was designed by the package HOOBAS[117]. The entire simulation was carried out on HOOMD-blue[118]. Simulations were run in the canonical ensemble (NVT) by means of Langevin dynamics. The time step was set to $\delta t = 0.01\ \tau$, where τ is the unit of time, corresponding to 10 fs. Each simulations was run for 10 μs in total. To study folding characteristics of the system, the potential depth for H-bond was varied by tuning epsilon

for respective bonding potential. A residue was deemed helical if the dihedral angles; phi (Φ) fall within the range of -160° to -20° and the psi (Ψ) fall within the range of -120° to 50°[119]. The simulations were carried out in triplicate for the full length (α0-6) protein as well as its fragments α0-3 and α4-6 separately and error bars represent standard deviations of three simulations.

All coarse-grained simulations were set up, performed and analyzed by [redacted] and [redacted] at the MPI-P.

2.2.10. Turbidity measurements and phase diagrams

Turbidity measurements were performed with an Omega plate reader (BMG LABTECH, Ortenberg, Germany) using 384-well plates (Cellvis, Mountain View, CA, USA). To maintain constant buffer concentrations at varying pH values we used phosphate buffer at empirically determined ratios of solutions of Na_2HPO_4, NaH_2PO_4 and H_3PO_4 resulting in a final buffer concentration of 10 mM phosphate and 10 mM HEPES at the indicated pH value. 60 µL of protein sample were prepared in either Phase separation buffer or PEG-NaCl buffer at the indicated concentrations of PEG, NaCl and if applicable urea. In order to ensure well mixed and rapidly equilibrated protein samples, the protein was pre-mixed in buffer containing neither PEG, nor NaCl, nor pH altering phosphate buffer, but if applicable with 4 M urea. Then the premixed protein was added to the phase separation buffer or PEG-NaCl buffer to reach the final composition for the experiment, mixed thoroughly by pipetting up and down. 50 µL out of the total 60 µL were transferred to the 384-well plate and allowed to incubate for 5 minutes at room temperature. Turbidity defined as the absorbance value at 350 nm after measuring as absorption in the range of 300 nm to 600 nm, 20 flashes per well, and 2 nm step width at room temperature. Samples were then subsequently imaged by DIC microscopy to distinguish between absorption arising from condensates or aggregates. Data from three independent turbidity measurements were combined to visualize condensate forming conditions in a phase diagram by setting a minimal measured turbidity value for indication of phase separation to 0.13 and a second value at twice the minimal value to give an indication for the changes at boundaries.

2.2.11. Differential interference contrast and fluorescence microscopy

Samples were prepared as described above for turbidity measurements and imaged after 15 minutes incubation time using Axio Observer.Z1 (Carl Zeiss, Jena, Germany) equipped with a 63x oil objective in differential interference contrast (DIC) mode, 500 ms acquisition time and 4.5-5.5 V lamp voltage. In case of fluorescently labeled crowder we used 12.5 µM (1 mol% in case of 10% PEG8k) Cy5-PEG (Biopharma PEG Scientific Inc., Watertown, USA) that was added to the PEG mixture for the condensate formation buffer. Fluorescence images were acquired using 3 ms acquisition time, 20% power of 630 nm LED light source for the Cy5 channel and 5 ms acquisition time, 20% power of 475 nm LED light source for the mVenus channel. The images were evaluated using the FIJI software[120] by automatically adjusting the brightness of the DIC and fluorescence images.

The images showing the fusion event were further processed for calculation of the aspect ratio. As opposed to fluorescence images where condensates are easily identified by setting a threshold above the background level, DIC images of condensates give signal above and below the image mean intensity. Therefore, using the FIJI software [120] a threshold was applied using the MEAN setting to yield binary images, followed by applying the MINUMUM filter (1 pixel), the MAXIMUM filter (12 pixel), two standard DILATION operations, the FILL HOLES operation and two standard ERODE operations. An ellipse was fit to the obtained particles using ANALYZE PARTICLES set to 3 decimal digits and limited to particles of > 100 pixels in size, obtaining the lengths of major and minor axis of the ellipse. The aspect ratio of the ellipse (A.R.) was calculated as $A.R. = \frac{\ell_{major}}{\ell_{minor}}$. Following an established protocol[121], an exponential function was used to fit the time dependence $A.R.(t) = 1 + (\mathrm{A.R._0} - 1)\exp(-\frac{t}{\tau})$, where t is the time after initiation if the fusion event, $A.R._0$ is the initial aspect ratio and τ is the characteristic relaxation time. The fit was preformed using the Levenberg-Marquardt algorithm implemented in OriginLab.

2.2.12. Fluorescence recovery after photobleaching measurements

For fluorescence recovery after photobleaching (FRAP) experiments sample chambers were assembled by lining two stripes of double-sided tape on a glass slide and covering it with a cover slide to form the chamber. Samples were prepared as described above for turbidity measurement while using 10% of the respective protein that was C-terminally fused to mVenus. FRAP experiments were performed on a Lyca SP5 confocal microscope using an FITC laser and 63x

glycerol objective at 1 % laser power for imaging. The sample was allowed to equilibrate inside the chamber for 15 minutes after mixing and regions of interest were selected for full-bleaching and partial bleaching of condensates. Image size was 41.33 µm x 41.33 µm with 128 x 128 pixels to enable fast frame rates of 0.06 s. Regions of interest (ROIs) were defined in the software to mark individual condensate areas for bleaching. The time series was set to 30 seconds of pre-bleach acquisition followed by 100% laser power bleach pulses for 10 frames (0.6 s) and 10 minutes of post-bleach acquisition. The FRAP experiments were evaluated using the FIJI software[120] by selecting and measuring the mean intensity over time in ROIs for the background, a control condensate and condensates that were bleached by the bleach pulse. For each experiment the background signal was subtracted, and the control condensate was used to correct for unwanted acquisition photobleaching. Normalized intensity was then calculated according to the following formulas:

$$I_{norm} = \frac{I - I_{min,post}}{I_{max,pre} - I_{min,post}},$$

$$c_{max,pre} = \max\,(c - bg),$$

$$I_{max,pre} = \max\,(\frac{I * c_{max}}{c} - bg),$$

$$I_{min,post} = \min\,(\frac{I * c_{max}}{c} - bg),$$

where *pre* and *post* refer to pre- and post-bleach time points being used for evaluation of extrema and *c* and *bg* are the mean intensities of ROIs from the background and the control condensate, respectively.

Comparing different condensate forming conditions and protein variants results in a variable size of condensates. Since variable condensates sizes can affect recovery times[122], we refrained from comparing recovery times and focused on recovered fractions after a certain time point.

2.2.13. In vivo localization and 3D rendering of fluorescently labeled IM30

Synechocystis cells grown in a shaker at 30 µEinstein in BG11-medium supplemented with 5 mM glucose and 100 µg/ml kanamycin were diluted at an OD_{750} > 2.0 to OD_{750} = 0.1 with addition of 1 mg/ml rhamnose for induction of the *rhaBAD* promoter and expression of the introduced genes.

After two days (OD_{750} = 0.4-0.6), cells were imaged using an Elyra 7 super resolution microscope (Zeiss, Oberkochen, Germany) using two track configuration, 642 nm for chlorophyll and 488 nm for mVenus, with the filter set to SBS LP 560 and simultaneous imaging by two cameras. Next, SIM2 processing was applied to generate super resolution images. For 3D rendering SIM^2 processing was applied to Z-stack raw data (slice interval 0.110 µm) and 3D rendering was done in Imaris (version 10.1.1). All *in vivo* fluorescence microscopy experiments shown in this study and corresponding 3D rendering were designed and performed in the Lab o [redacted] by [redacted] (University of Liverpool). We acknowledge the Liverpool Centre for Cell Imaging (CCI) for provision of imaging equipment and technical assistance.

Images for this study were further processed in ImageJ to set saturation levels and include scale bars.

2.2.14. Atomic force microscopy

Atomic force microscopy (AFM) was performed using a MultiMode 8-HR AFM (Bruker, Billerica, MA, USA) equipped with a J-scanner (Bruker, Billerica, MA, USA) at room temperature. The ScanAsyst-Fluid+ cantilever (Bruker, Billerica, MA, USA) with a nominal spring constant of 0.7 N/m, a nominal tip radius of 2 nm, and a resonance frequency of 150 kHz was mounted on a fluid cell (MTFML-V2). The fluid cell was assembled on top of freshly cleaved mica (12 mm diameter; grade V1, Ted Pella, Redding, CA, USA). The deflection sensitivity was calibrated on mica and spring constant was determined using thermal tune each day before starting the measurement. Lipid samples for the formation of supported lipid bilayers (SLBs) were prepared by mixing DOPG and DOPC in 4 to 6 molar ratio and drying a 1 mg lipid film inside a 2.5 ml glass vial under constant nitrogen flow and subsequent removal of residual organic solvent by incubation for at least 2 h in an exsiccator with vacuum applied. The lipid film was hydrated with 250 µl HEPES buffer, vortexed for 10 s, and the turbid liposome solution was transferred to an Eppendorf tube. The lipid sample was sonicated in water batch for at least 15 minutes with 3 short freeze-thawed steps separated by 5 minutes. This resulted in less turbid lipid samples containing higher amounts of small unilamellar vesicles (SUVs) and facilitated spriting of liposomes on mica. SLBs were prepared by first washing the fluid cell with adsorption buffer and then incubating 2 mg/ml lipid in adsorption buffer inside the fluid cell for at least 30 minutes. The fluid cell was finally washed with 1 ml HEPES buffer. Formation of a lipid bilayer was testes in ramp mode and testing for the

characteristic breakthrough force-distance curve of the tip that is piercing through the SLB. A 20 µm x 20 µm area was scanned to validate complete coverage of mica by the SLB in the imaging area. Protein was applied incubated at the indicated concentration for at least 5 minutes and washed with 1 ml HEPES buffer. Images were scanned from top to bottom with the scanning speed set to < 1 Hz and scans per line set to 256 or 512. The size of the scanned images was 5x5 µm or 20x20 µm and is stated in the image description. Data was processed in Gwyddion[123] (version 2.58) by applying a median filter and subtracting a plane fit from the background. Line profiles were analyzed in Gwyddion and exported as text files to generate graphs in OriginLab. AFM topographic images were generated with the scale set to 10 nm and using the Sky color palette in Gwyddion.

3. Results and Discussion

3.1 Monomer unfolding of a bacterial ESCRT-III superfamily member is coupled to oligomer disassembly

3.1.1. Abstract

The inner membrane associated protein of 30 kDa (IM30) is a member of the endosomal sorting complex required for transport (ESCRT-III) superfamily and crucially involved in the biogenesis and maintenance of thylakoid membranes in cyanobacteria and chloroplasts. In solution, IM30 assembles into various higher oligomeric barrel- or tube-like structures, whereas upon membrane binding it forms large, flat carpet structures. Dynamic localization of the protein in solution, to membranes and changes of the oligomeric states are crucial for its *in vivo* function. ESCRT-III proteins are known to form oligomeric structures that are dynamically assembled from monomeric/smaller oligomeric proteins, and thus these smaller building blocks must be assembled sequentially in a highly orchestrated manner, a still poorly understood process. The impact of IM30 oligomerization on function remains difficult to study due to the high intrinsic tendency to homo-oligomerize. Here, we used molecular dynamics simulations to investigate the stability of individual helices in IM30 and identified unstable regions that may provide structural flexibility. Urea-mediated disassembly of the IM30 barrel structures was spectroscopically monitored, as well as changes in the protein´s tertiary and secondary structure. The experimental data were finally compared to a 3-state model that describes oligomer disassembly and monomer unfolding. In this study we identified a highly stable conserved structural core of ESCRT-III proteins and discuss the advantages of having a flexible intermediate structures and their putative relevance for ESCRT-III proteins.

3.1.2. Introduction

The *Inner Membrane-associated protein of 30 kDa* (IM30), also known as Vipp1 (the *vesicle-inducing protein in plastids 1*), is found in organisms/organelles that perform oxygenic photosynthesis and contain thylakoid membranes (TMs), *i.e.* cyanobacteria and chloroplasts [90,91,95]. While its exact physiological function still is under debate, IM30 clearly is essential for the biogenesis and maintenance of the TMs that contain the complexes of the photosynthetic electron transfer chain[55].

IM30 likely evolved via duplication of the gene coding for the *phage shock protein A* (PspA), a protein found in bacteria where it appears to be involved in maintenance and repair of the cytoplasmic membrane [124–126]. When compared to PspA, IM30 has a prolonged C-terminus, which likely is a determinant for its distinct function in TM biogenesis and maintenance[106]. While in bacteria solely PspA or PspA-like proteins, such as LiaH in *Bacillus subtilis*, are encoded and chloroplasts exclusively contain IM30, many cyanobacterial genomes encode both, PspA plus IM30[126,127].

Both PspA and IM30, together with canonical eukaryotic ESCRT-III proteins, belong to the ESCRT-III superfamily[96–98], where all superfamily members share key structural elements[99]. All superfamily members have a structural core of fife α-helical segments, all contain a coiled-coil formed by helices α1-2, as well as have a pronounced tendency to form large oligomeric barrel/rod structures[96–98,127]. While the sequences of IM30 and PspA of the cyanobacterium *Synechocystis* sp. PCC 6803 (from here on: *Synechocystis*) share a similarity of only 51% [128], the monomer structures of the proteins are highly similar[96,98] with a largely conserved structure of the PspA-domain, formed by helices α0-5. However, as mentioned before, IM30 contains the extra helix α6 at its C-terminus.

In solution, IM30 of *Synechocystis* as well as of *Nostoc punctiforme* form large homo-oligomeric, dome-shaped barrel structures with various symmetries, albeit the protein can also form rod structures [129–131]. Within these oligomers, the PspA domains are organized in stacked layers where the protomers within one layer and between layers are connected by conserved intermolecular interfaces [98,99]. Within a barrel, a single monomer can interact with up to 15 other monomers that are up to one layer away along the symmetry axis and as far as three stacks away in a different symmetrical unit[96]. The recently solved structures of the two different cyanobacterial IM30

proteins confirmed that the structural features and monomer interactions within the ESCRT-III superfamily are conserved, involving the central coiled-coil formed by helices α1-2, conserved flexible hinge regions, and defined inter-and intramolecular interfaces [96–98,132]. When part of an oligomeric assembly, the *Synechocystis* IM30 protein is largely α-helical, with 5 α-helices (helices α0-5) being resolved in the cryo-EM structures[96]. Yet, in an IM30 variant that does not form stable homo-oligomeric structures anymore (IM30*), the regions forming helices α0 plus α4-7 in the oligomer appear to be unstructured, whereas the coiled-coil formed by helices α1-2, as well as helix α3, which is a prolongation of α2 and also interacts with α1-2, remain structured[104]. This observation indicates that ring disassembly coincides with partial unfolding of IM30 monomers, or, *vice versa*, ring formation involves the formation of α-helical segments in previously disordered regions. However, IM30* contains mutations that disturb inter-monomer contacts, and it cannot be excluded that these mutations might also destabilized the protein secondary structure [104] .

Members of the ESCRT-III superfamily do not only share common structural features[97,99], all members of the ESCRT-III superfamily appear to be involved in membrane remodeling processes[51,133,134]. IM30 binds to negatively charged membrane surfaces[111] and forms membrane-covering carpets *in vitro*[104]. The formation of carpets has been shown to involve (i) adhesion of IM30 barrels at membrane surfaces and (ii) subsequent disassembly of the barrels[104]. How exactly these observations relate to the *in vivo* function of IM30 is still largely unknown, although membrane binding as well as formation of large membrane-attached IM30 assemblies has been observed *in vitro* upon membrane stress[107,112,131]. For ATP production driven by the pH gradient established across the TM in the light, the integrity of the TM must be maintained, and IM30 carpets were suggested to protect membranes against proton leakage[104,135]. Interestingly, IM30* forms carpets rapidly and appears to protect membranes more effectively than IM30 wt, at least *in vitro*[104], indicating that IM30 oligomerization counteracts membrane binding and protection[111] . Thus, the availability of mono- *vs*. oligomeric IM30 likely needs to be fine-tuned *in vivo*. The structural dynamics (monomer *vs*. oligomer) as well as soluble *vs*. membrane-attached IM30 populations are likely crucial for the IM30 *in vivo* function[136] . In fact, soluble as well as membrane-attached IM30 fractions have been observed *in vivo*[107,112].

In contrast to wt IM30, which forms large oligomeric barrels in solution, IM30* is monomeric or forms small homo-oligomers with only the helices α1-3 coiled-coil remaining structured and the

rest of the protein becoming largely disordered[104]. Furthermore, the isolated helices α4-6 (Fig. 1A), are largely unfolded in solution[137]. Thus, the C-terminal half seems to have no high propensity to form α-helices or even oligomers in absence of helices α0-3. Yet, very little is known about the processes controlling IM30 oligomer formation. Since the IM30 function appears to be coupled to its dynamic cellular localization, involving different IM30 folding states[136], it is crucial to understand the structural dynamics in greater detail to be able to eventually control the formation of specific IM30 states for more detailed *in vitro* analyzes.

Thus far, the impact of the IM30 oligomeric state on its *in vitro* and *in vivo* activity has been studied mainly via generation and analyzes of truncated IM30 variants as well as variants carrying destabilizing mutations[104,106,137]. Yet, to better understand the thermodynamic principles guiding oligomer formation in solution and/or on membrane surfaces, it clearly is advantageous to understand oligomerization of the wt protein. Luckily, after unfolding IM30 by urea, the protein refolds, forms the prototypical IM30 oligomeric structures[105,106,138] and binds to lipid membranes as observed with the protein purified under native conditions[138]. These observations now enabled us to study individual steps during urea-mediated unfolding of IM30 (oligomers).

We now show that unfolding of a significant part of wt IM30 monomers is coupled to disassembly of the large, homo-oligomeric ring structures. Yet, when the oligomeric IM30 barrel structures disassemble into smaller oligomers and/or monomers, the structure of the α1-2 coiled-coil is retained. Based on our experimental data and a derived theoretical model we demonstrate that it is impossible to disassemble all oligomeric barrel structures completely using urea without simultaneously unfolding the IM30 monomers. Eukaryotic ESCRT-III proteins are also known to form oligomeric structures that are dynamically assembled from monomeric/smaller oligomeric proteins, a process that is still poorly understood. Based on our analysis of a manageable ESCRT-III model, we generally discuss the advantages of having a flexible intermediate structure and its potential relevance for ESCRT-III superfamily proteins.

3.1.3. Results and Discussion

3.1.3.1. In silico unfolding of IM30

Based on previous observations, it is feasible to assume that the structure of IM30* mimics the structure of the IM30 wt protein when the protein is not part of an oligomeric assembly. Yet, a direct comparison with the structure of the IM30 wt in a monomeric form is not possible, since this cannot be isolated under native conditions because of its strong intrinsic propensity to homo-oligomerize (**Figure 3.1-1**).

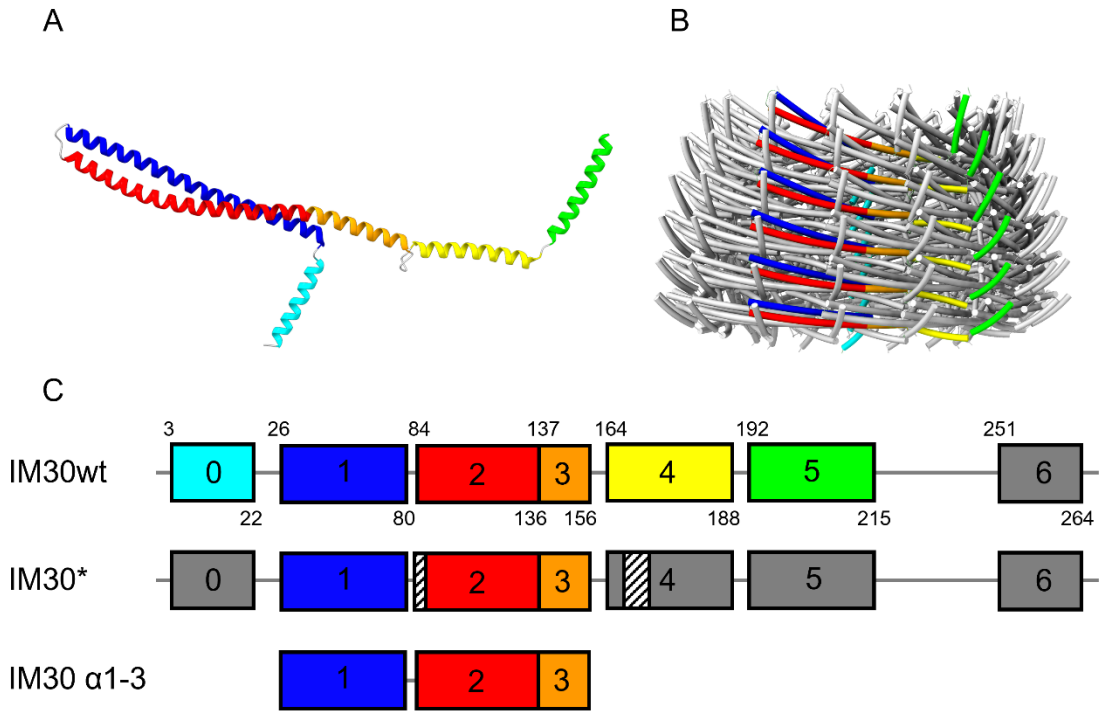

***Figure 3.1-1**: IM30 structure and schematic representations of truncated IM30 variants. (A) Structure of an IM30 monomer without the C-terminal flexible region containing α6 (PDB: 7O3Y). The colors are as in (C). (B) Model of IM30 rings in cylinder cartoon representation (PDB:7O3Y). (C) Schematic representation of full-length and truncated IM30 variants analyzed in this study. Numbers inside the boxes represent numbers of helices, and colors in boxes correspond to colors of helices in the model. Grey color indicates flexible and disordered regions. Small numbers above and below boxes represent beginning and end of regions defined in this study as helix. The position of mutated amino acids in IM30* are indicated by white boxes with black stripes.*

Therefore, we first utilized the power of molecular dynamics (MD) simulations to precisely follow the unfolding transition of the mainly α-helical IM30 wt structure upon *in silico* destabilization. Since H-bonds are the main interactions stabilizing α-helices, we performed MD simulations at decreasing H-bond strength to destabilize the protein secondary structure and followed the changes in the propensity of individual amino acids to be part of an α-helix. At 100% H-bond strength, 60% and 80% of the α0-3 and α4-6 regions were α-helical, and by lowering the H-bond strength to 75%, the α-helical propensity was drastically reduced to 10% (**Figure 3.1-2**).

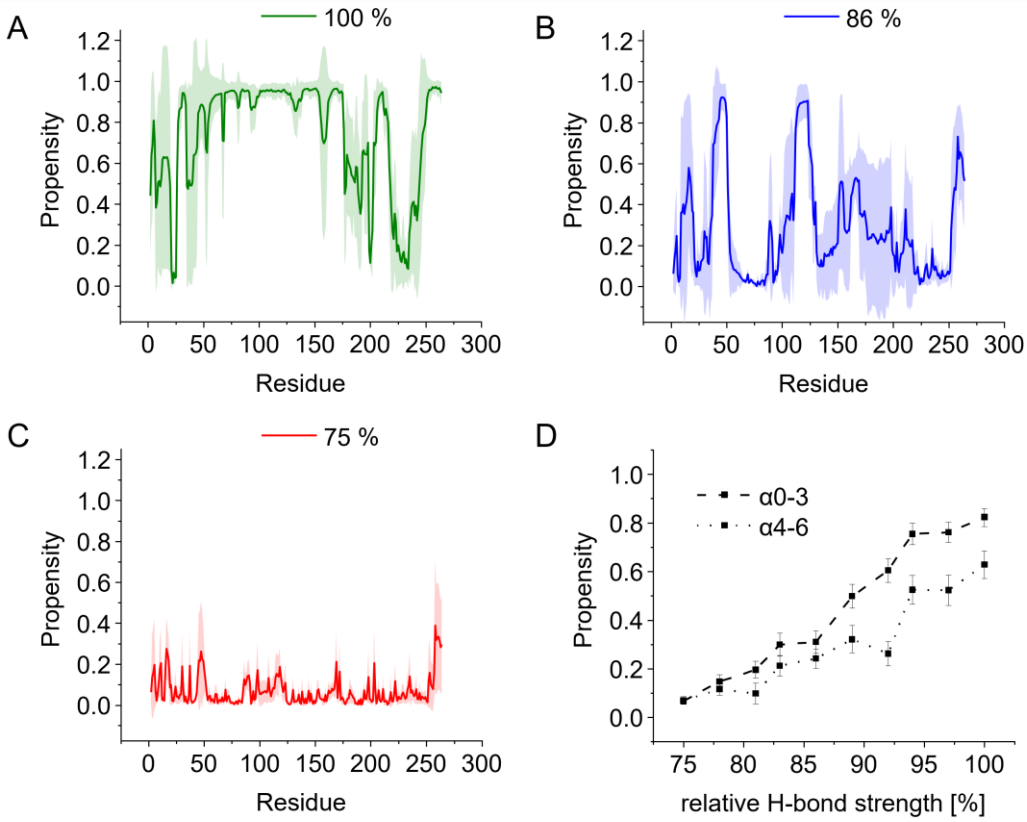

***Figure 3.1-2**: Influence of relative H-bond strength on the α-helicity of IM30 monomers determined via coarse-grained simulations in solution. Sequence propensity vs. amino acid position of full-length protein, at (A) 100, (B) (86%) and (C) 75% H-bond strength (D) Helical propensity of α0-3 and α4-6 within the full length α0-6. Coarse-grained simulations were set up, performed and analyzed by* [redacted] *and* [redacted].

Further analyses revealed that the coiled-coil forming region α0-3 showed a consistently higher propensity to form α-helices compared to α4-6 at equal H-bond strength, indicating a higher stability of the helices involved in coiled-coil formation (**Figure 3.1-2**D). These differences

prompted us to experimentally investigate the changes in the IM30 structure upon disassembly of higher oligomers.

3.1.3.2. Urea-induced destabilization of the oligomeric IM30 structure

Due to our simulation results and the low helix-forming propensity of the C-terminal helices α4-6[104,137], structure formation of this part of the protein might be coupled to homo-oligomerization of the full-length protein, *i.e.* to the formation of stabilizing contacts. Thus, to determine whether (partial) unfolding of the IM30 wt monomer precedes, is paired with, or follows oligomer disassembly, we monitored changes in the secondary and tertiary structure as well as in the oligomeric assembly state at urea concentrations in the range 0 –7 M.

To first monitor changes in quaternary structure, we measured the scattering signal of IM30 wt at increasing urea concentrations. Due to the large size, IM30 barrels show a strong scattering signal in the absence of urea (**Figure 3.1-3**).

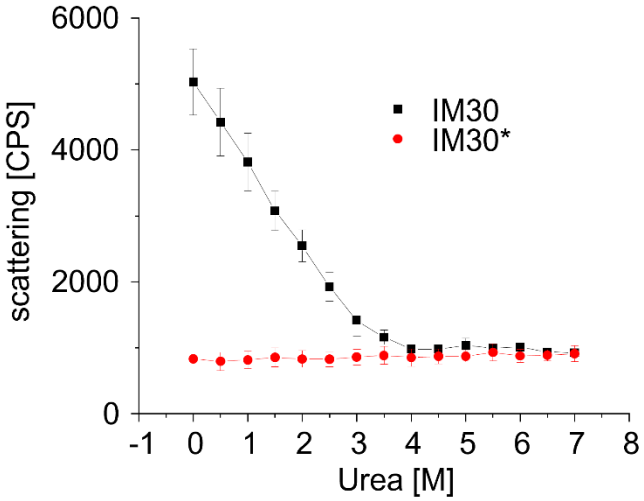

Figure 3.1-3*: Scattering signal of IM30 at increasing urea concentrations. IM30 wt (black squares) and IM30* (red circles). The error bars represent SD, n=3.*

Upon increasing the urea concentration from 0 to 3.5 M urea, the scattering signal decreased nearly linearly until it reached a constant level which was about six times lower than the scattering signal observed at 0 M urea. This suggests that the barrel structure is continuously destabilized until a concentration of ~ 3.5 M urea is reached. Yet, for a well-defined system of only one oligomer type

one would expect a sigmoidal curve for disappearance of the barrels in presence of a chemical denaturant. However, since IM30 forms barrels of different sizes, and also stacks of barrels and even tubular structures[129–131,139], the observed linear decrease in scattering clearly reflects different dissociation processes.

In contrast to the wt, the scattering signal determined for the IM30* variant that does not form large oligomers, remains essentially constant at all urea concentrations and is equal to the level that the wt protein reached at urea concentrations >3.5 M.

3.1.3.3. Monitoring IM30 denaturation via changes in Trp fluorescence emission

Changes in Trp fluorescence characteristics can be used to monitor variations in the polarity of a Trp´s environment, such as exposure of Trp residues to a more polar aqueous environment due to protein unfolding, leading to a redshift of Trp's emission maximum. Therefore, we measured Trp fluorescence emission spectra at increasing urea concentrations to monitor alterations of the Trp environment, induced by changes in the tertiary and/or quaternary structure of IM30.

IM30 contains a single Trp residue in position 71 on helix α1 (**Figure 3.1-4**). This residue is part of the structured core of IM30, *i.e.* the coiled-coil formed by helices α1 and α2, and is facing away from the barrels outer surface to the inside of the barrel.

In the coiled-coil, Trp71 is sandwiched between the helices α1 and α2. In the barrel, the accessibility of Trp71 is further confined by protomers of neighboring layers. Residues from these neighboring protomers form together a small pocket around Trp71, from here on referred to as the

Trp-pocket. Thus, in the IM30 wt barrel structures Trp71 is primarily confined by the formation of the coiled-coil plus further buried in a Trp-pocket formed by multiple protomers (**Figure 3.1-4**).

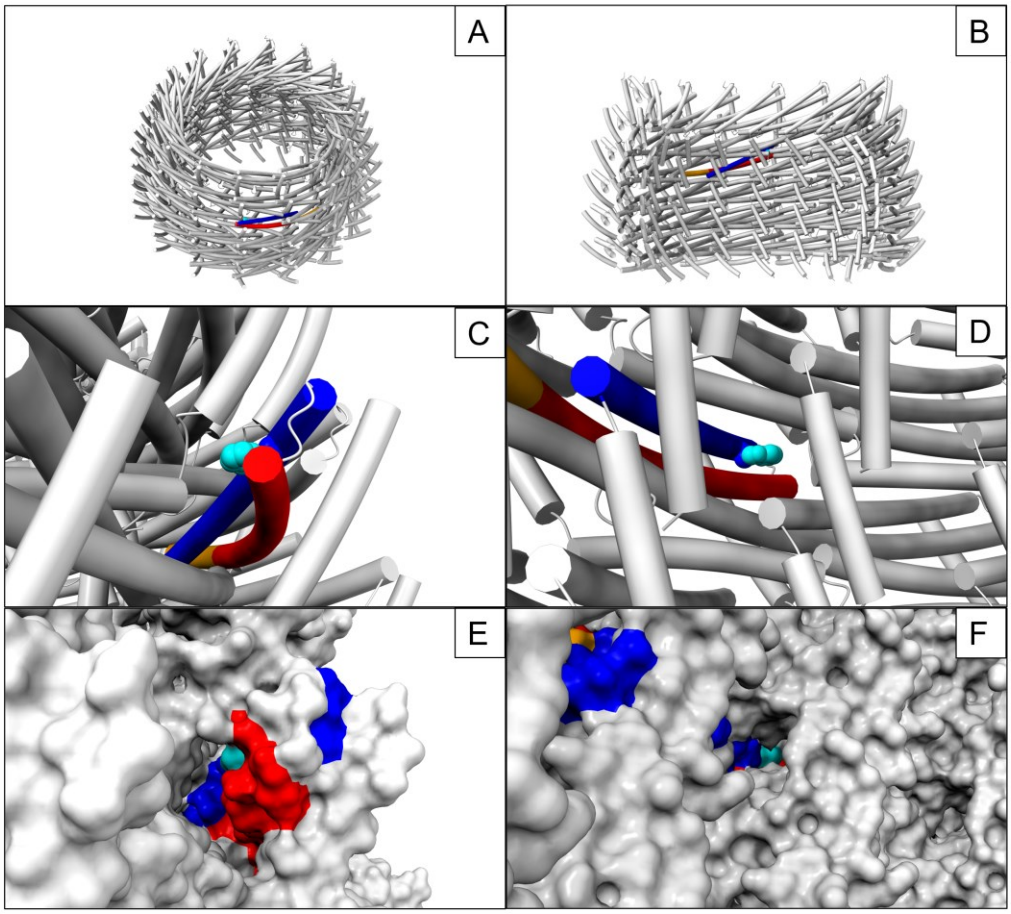

Figure 3.1-4*: The IM30 Trp71 pocket; (A) Location of a coiled-coil in layer 3 of the IM30 barrel structure in tube representation (PDB: 7O3Y). (B) Cut-view of the inside of the barrel structure in tube representation. (C-F) Solvent access to the Trp71 pocket as seen from the outside (C+E) and inside (D+F) in tube representation (C+D) and surface representation (E+F). α--Helices α1 (blue), α2 (red) and α3 (orange). Trp side chain atoms are shown as spheres, and the indole ring atoms and its corresponding surface are colored in cyan.*

Although the Trp residue is somewhat buried within the barrel, solvent can access the Trp pocket from both the outside and the inside of the barrel (**Figure 3.1-4**E, F). From the outside, solvent access is provided in all layers through a large gap near the closed end of the coiled-coil hairpin below the adjacent α5 of the monomer i^{+3} (**Figure 3.1-4**C, E), another gap between α2 of the coiled-coil and α3 of monomer *i* in layer L^{-1} and also between α3 and α2 of monomer *i* in layer L^{+1}. From the inside there is solvent access to the Trp pocket through an elongated opening (**Figure 3.1-4**D, F) that is also found in all layers of the barrel structure.

When calculating the accessible area of the Trp´s indole ring surface in the barrel structure (78 Å^2), the isolated coiled-coil (100 Å^2) and α2 by itself (166 Å^2), it becomes evident that the solvent accessible area of the Trp surface increases only by 24% upon barrel disassembly, when the coiled-coil is still intact, compared to an increase of >100% in the isolated α2 helix. It has been shown by MD simulation that the wavelength of maximal emission correlates with the solvent accessible area[140]. Therefore, we expect that barrel disassembly has a much smaller effect on Trp's emission spectrum than opening and/or unfolding of the coiled-coil.

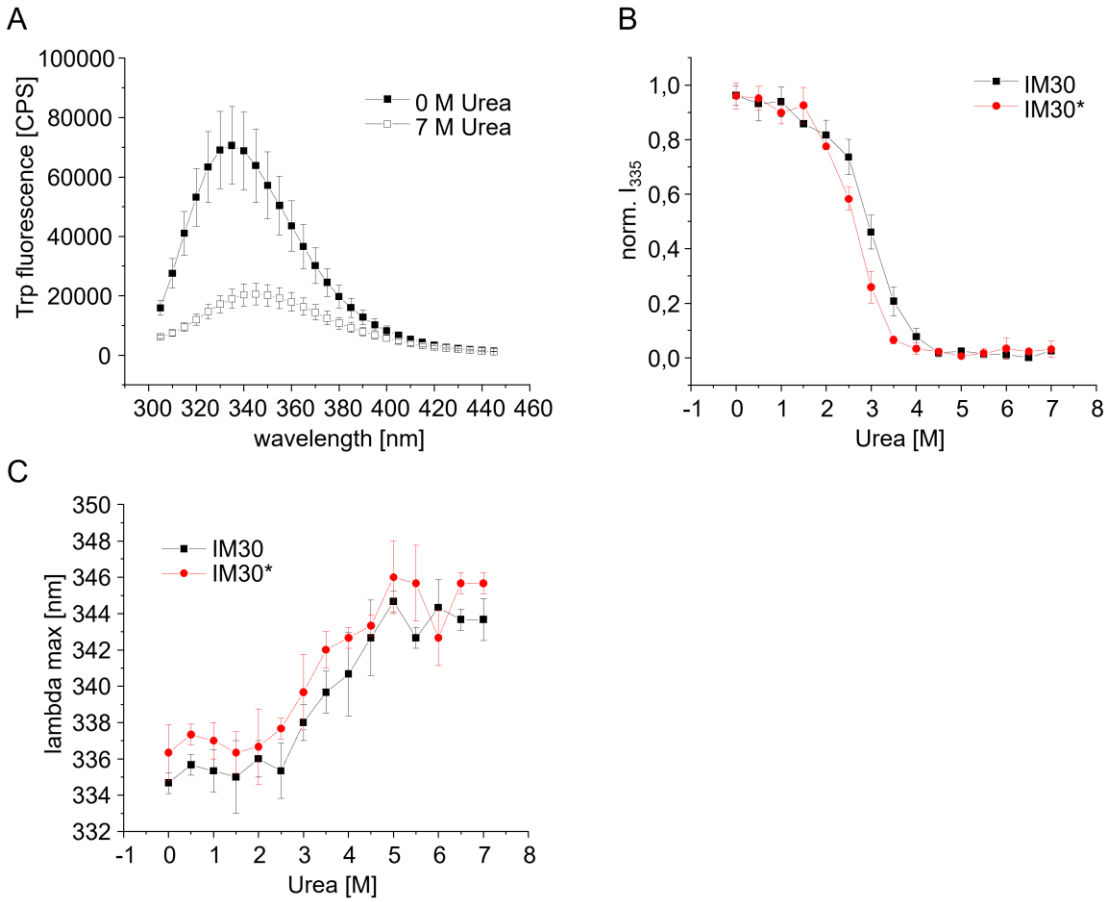

Figure 3.1-5*: Tryptophan fluorescence emission of IM30 at increasing urea concentrations. (A) Trp fluorescence emission spectra of IM30 at 0 M urea (full squares) and 7 M urea (empty squares). (B) Fluorescence intensity at 335 nm, IM30wt (black squares) and IM30* (red circles). (C) Wavelength of emission maximum IM30wt (black squares) and IM30* (red circles). See suppl. Figure 2 for non-normalized data. The error bars represent SD, n=3.*

This assumption is supported by the observation that the fluorescence emission maximum of IM30 wt is only slightly lower than that of IM30* (334.7 ± 0.6 nm and 336.3 ± 1.5 nm, respectively),

while the emission maximum of the unfolded protein is strongly increased (344 ± 1 nm) (**Figure 3.1-5**C). Also, the fluorescence intensity is strongly decreased at a urea concentration of 7 M compared to the intensity in absence of urea (**Figure 3.1-5**A). In order to monitor the urea-induced denaturation of IM30 wt and IM30*, the relative intensity at 335 nm (I_{335}) and the position of the emission maximum (λ_{max}) was monitored (**Figure 3.1-5**B, C). The decrease in the Trp fluorescence intensity and the shift in λ_{max} (**Figure 3.1-5**B, C) can be divided into 3 stages for both variants: at low urea concentrations from 0 to 2 M, the Trp fluorescence intensity decreases moderately. The relative intensity is about 85 ± 5% for IM30 and 80.6% ± 0.6% for IM30*. From 2.5 M to 4.5 M urea a pronounced change is observed. whereas above 4.5 M urea the characteristics of the Trp's environment appear not to change further. The changes of λ_{max} at increasing urea concentrations follow a similar pattern, yet between 0 and 2 M urea the λ_{max} value does not change at all. The pronounced change in Trp's spectral characteristics between 2.5 and 4.5 M urea indicates a considerable exposure of Trp71 to a more polar environment, likely due to unwinding of the helix α1/2 coiled-coil (as further analyzed and discussed below).

Taken together, the observations indicate that the urea-induced solvent exposure of Trp71 is similar for IM30 wt and IM30*, with a slight right-shift of the curve in case of IM30 wt, which might be due to the stabilization of the protein structure by barrel formation.

3.1.3.4. Urea-induced destabilization of the IM30 secondary structure

In order to analyze whether between 2.5 and 4.5 M urea mainly the coiled-coil helices unfold, as hypothesized based on the fluorescence measurements, CD-spectroscopy was employed, allowing to monitor changes in the protein´s secondary structure.

In the absence of urea, the IM30 wt protein shows a strong CD-signal with minima at 208 and 222 nm, as characteristic for a mainly α-helical protein (**Figure 3.1-6**A), in line with the solved structure[96]. The shape of the spectrum is different for IM30* when compared to IM30 wt (**Figure 3.1-6** B), and the fraction of protein adopting an α-helical structure is smaller in IM30*, in agreement with earlier studies[104]. The difference in shape is also reflected in the different value for the ratio of the CD signal at 222 nm and 208 nm in absence of urea (**Figure 3.1-6**D), which illustrates changes in the general shape of the CD spectrum.

The overall dependence of the CD signal at 222 nm on the urea concentration is quite similar to the changes of the Trp fluorescence emission observed at increasing urea concentrations (**Figure 3.1-6**C), both for IM30 wt and IM30*: between 0 and 2 M only a small change is observed, followed by a pronounced decrease in ellipticity between 2.5 and 4.5 M, and a constant ellipticity above 4.5 M urea. For both proteins, the ratio of the CD-signals at 208 nm and 222 nm remains essentially constant between 0 and 2 M urea (Figure 3.1-6 D) and starts to drop at about 2.5 M urea. Of note: the corresponding ratio determined at urea concentrations > 4.5 M have to be excluded from the analysis and discussion, due to a low signal-to-noise ratio at 208 nm caused by high Measured turbidity ofof urea as indicated by high detector voltages.

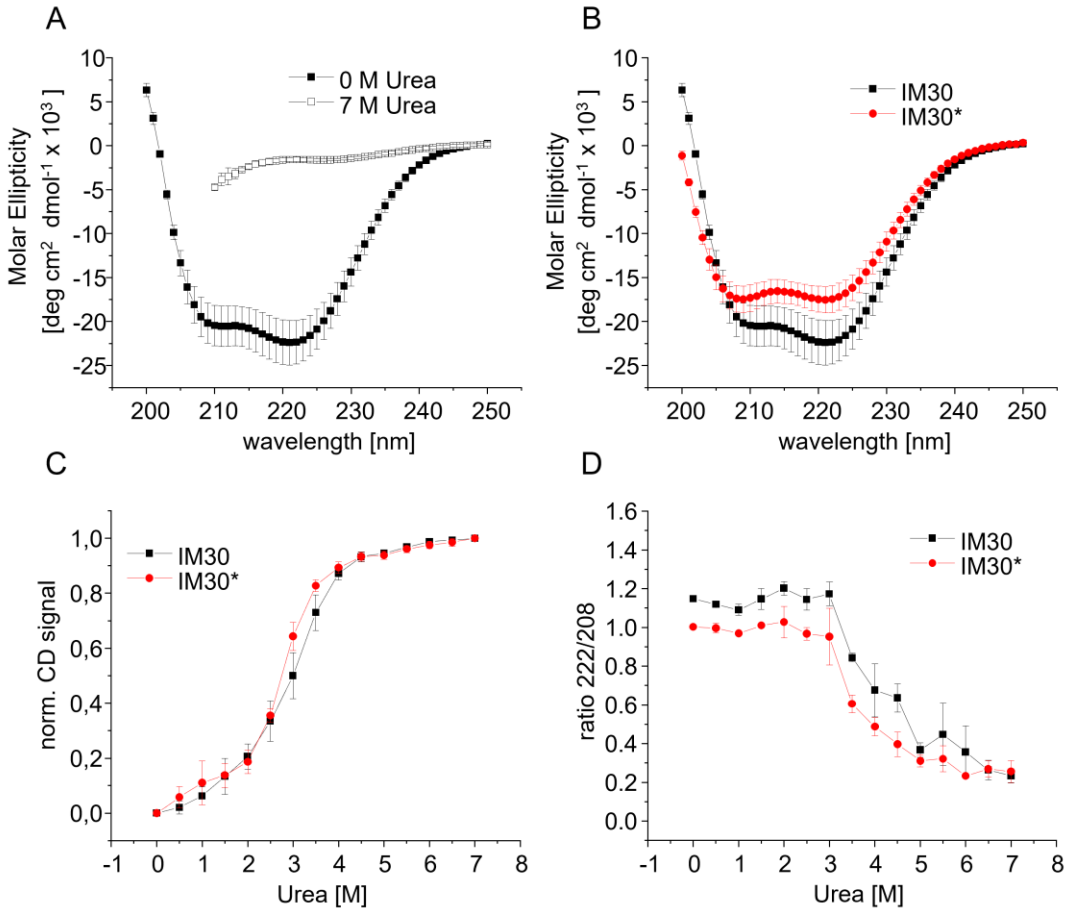

***Figure 3.1-6**: CD signal changes at increasing urea concentrations. (A) CD spectrum of IM30wt at 0 M urea (full squares) and 7 M Urea (empty squares). (B) CD Spectrum of IM30wt (black squares) and IM30* (red circles) at 0 M urea; (C) Normalized CD signal at 222 nm at increasing urea concentration for IM30wt (black squares) and IM30* (red circles). See suppl. Figure 2 for non-normalized data. (D) CD signal ratio 222 nm to 208 nm at increasing urea concentrations for IM30wt (black squares) and IM30* (red circles). The error bars represent SD, n=3.*

Together, these observations indicate that for both IM30 wt and IM30* between 2.5 and 4.5 M urea most α-helical regions unfold. As in IM30* helices α0 and α4-6 are largely disordered, the unfolding curve likely is dominated by the coiled-coil formed by helices α1-3.

3.1.3.5. In silico unfolding of isolated IM30 regions

To test our assumption that the coiled-coil forms a stable structured core whereas the C-terminal region is disordered upon barrel disassembly, we next carried out coarse grained simulations of isolated protein segments while varying the H-bond strength in our simulation, mimicking the destabilizing effect of urea. Again, with decreasing relative H-bond strengths we observed a general decrease in the propensity to form α-helices and the decrease consistently required a stronger reduction in H-bond strength for the α0-3 region compared to α4-6 (**Figure 3.1-7**A). This effect was observed for simulations of both the full-length protein as well as the individual truncated variants (α0-3 and α4-6) (**Figure 3.1-2**D, **Figure 3.1-7**A).

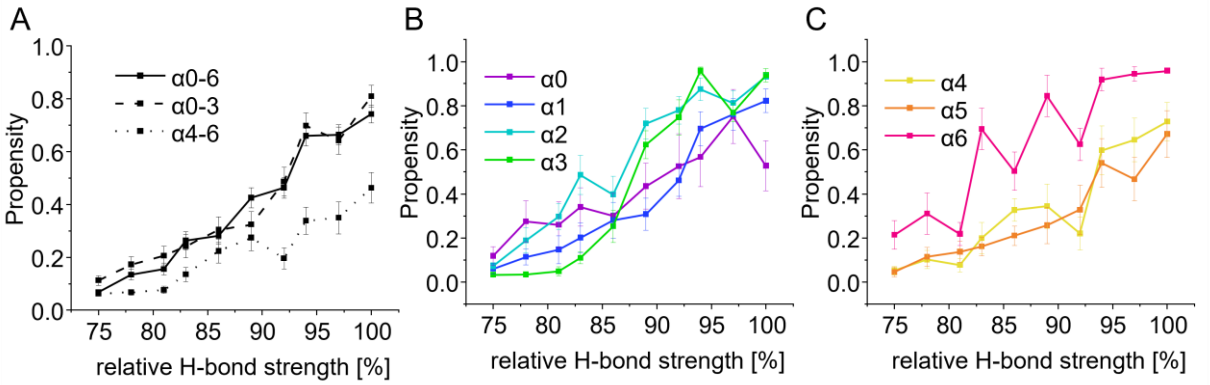

***Figure 3.1-7**: Influence of relative H-bond strength on propensity of IM30 in coarse-grained simulations of monomers in solution.(A) Propensity of the full length (α0-6) and its fragments (α0-3) and (α4-6) simulated separately. (B) Helical propensity of each helix of the α0-3 fragment calculated from simulating the structure α0-6 with respect to relative H-bond strength; (C) Helical propensity of each helix within the fragments α4-6 of simulating structure α0-6. Coarse-grained simulations were set up, performed and analyzed by* [redacted] *and* [redacted].

Next, we analyzed the stability of individual regions that form α-helices in the barrel structure at varying H-bond strength. The helices of the N-terminal region show an α-helical propensity above 40 % at 92% H-bond strength (**Figure 3.1-7**B), in contrast to the C-terminal helices α4-6 where

the α-helicity is already drastically decreased at 92% H-bond strength compared to 100% (**Figure 3.1-7**C). Taken together our simulations support the hypothesis that IM30 retains its coiled-coil structure while other regions of the protein become disorder upon barrel disassembly.

3.1.3.6. The IM30 coiled-coil core remains intact upon barrel disassembly

The above presented results and simulations indicate that at low urea concentrations for both, IM30 and IM30*, a state with a structured α-helical region exists. The central coiled-coil formed by helices α1-3 is a conserved structural motif found in all members of the ESCRT-III protein superfamily. This coiled-coil is the only region that remains structured in IM30*, where most of the protein is disordered in solution[104]. In order test the assumption that between 2.5 and 4.5 M urea unwinding and unfolding of this structured core is observed independently of helices α0 and α4-α6, we next analyzed the stability of the isolated helical hairpin formed by the helices α1-3 ($IM30_{26-156}$), to investigate its contributions to the structure and stability of the full-length IM30 monomer.

The scattering signal of $IM30_{26-156}$ was as low as observed before for IM30* (**Figure 3.1-3**) and remains constant in the range of 0 to 7 M urea (**Figure 3.1-8**A). This is perfectly in line with the simulations (**Figure 3.1-7**) and the recent observation that the isolated coiled-coil does not form large oligomeric structures in solution.[104,137]

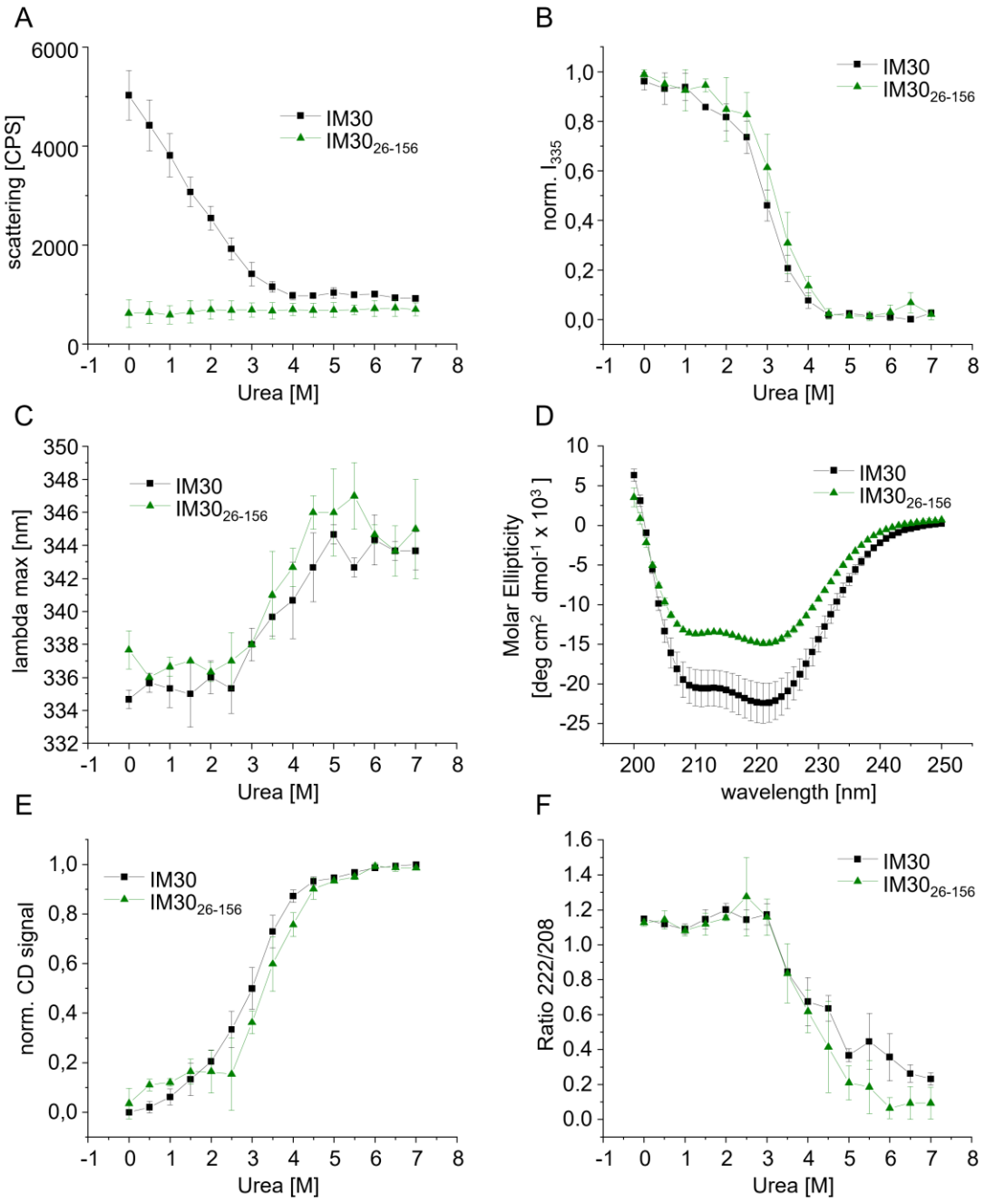

Figure 3.1-8*: The structure of IM30$_{26-156}$ at increasing urea concentrations. (A) Scattering, (B) normalized Trp Fluorescence intensity at 335 nm, (C) maximum wavelength, (D) CD spectrum, (E) normalized CD-Signal at 222 nm, and (F) CD signal ratio 222 nm to 208 nm at increasing urea concentrations for IM30 (black squares) and .IM30$_{26-156}$ (green triangles). See suppl. figure 2 for non-normalized data. The error bars represent SD, n=3.*

The Trp fluorescence emission characteristics of IM30$_{26-156}$ change only slightly at low urea concentrations followed by a strong decrease in intensity and a red-shift in the fluorescence

emission maximum at concentrations above 2.5 M urea (**Figure 3.1-8**B, C), exactly as observed before for the wt and IM30* variant (**Figure 3.1-5**). This strongly supports the conclusion that the Trp71 environment inside the isolated coiled-coil remains largely unaltered at low urea concentrations (0-2.5 M), whereas the Trp environment becomes more polar at higher urea concentrations due to exposure of Trp71 to the aqueous solution caused by unwinding and possible unfolding of the coiled-coil, visible as a red shift in the Trp emission maximum. After a strong change in the fluorescence characteristics between 2.5-4.5 M urea, the fluorescence intensity and the fluorescence emission maximum remained constant from about 4.5 M urea on, as also observed for IM30 and IM30*. This indicates that increasing the urea concentration did not result in further protein unfolding. Unfolding of the coiled-coiled structure between 2.5 and 4.5 M urea was also shown by CD-spectroscopy, indicated by a very sharp decrease in the amplitude of the CD-signal at 222 nm (**Figure 3.1-8**E). Again, as observed for the other two variants, the decrease in the CD-signal amplitude at 222 nm is mirrored by the decreases in the Trp emission intensity, strongly supporting the hypothesis that the loss of tertiary interactions in the coiled-coil coincides with the loss of remaining α-helical structure in IM30. In fact, also the CD-signal ratio of 222 nm-to-208 nm decreased (**Figure 3.1-8**F), as observed for IM30 and IM30* at similar concentrations (**Figure 3.1-6**D). A 222/208 ratio > 1 is a well-known indication for coiled-coil formation, or, more generally, for interaction of α-helices[141,142], and thus, the coiled-coil appears to unwind at urea concentrations > 3 M (**Figure 3.1-8**F). Unwinding of the coiled-coil, which leads to solvent exposure of Trp71, is coupled to unfolding of the α-helices (**Figure 3.1-5**, **Figure 3.1-6**, **Figure 3.1-8**). As for IM30 and IM30*, the CD-signal at 222 nm reached a plateau at ~4.5 M urea where the coiled-coil-forming helices are entirely unfolded.

Together, the analyses of the isolated helical hairpin strongly support the assumption that the helix α1/α3 coiled-coil is the most stable structure in the wt protein and only unfolds at high urea concentration, i.e. at conditions where IM30 oligomers are already disassembled and helices α0 and α4-α6 unfolded.

3.1.3.7. Barrel disassembly of IM30 wt is rate limiting in unfolding kinetics

While the scattering data indicate that the IM30 wt barrels are largely disassembled at urea concentration <3 M, the fluorescence and CD data suggest unfolding of α-helices at urea

concentrations >3 M, indicating that barrel disassembly has to take place before tertiary structure changes near Trp71 occur.

To further scrutinize this assumption, we next investigated the kinetics of unfolding IM30 or IM30*, respectively. To this end, solutions containing the protein in buffer were rapidly mixed 1:1 with a solution containing 8 M urea. The reaction was monitored on one hand based on Trp fluorescence as indicator for tertiary structure changes and on the other hand by measuring the change in scattering to follow barrel disassembly (Figure 9). In order to determine the respective signal of the initial, native state, the proteins were mixed with urea-free buffer in a separate experiment (control). For comparison of the different curves, the measured values were normalized to the initial value of the respective control.

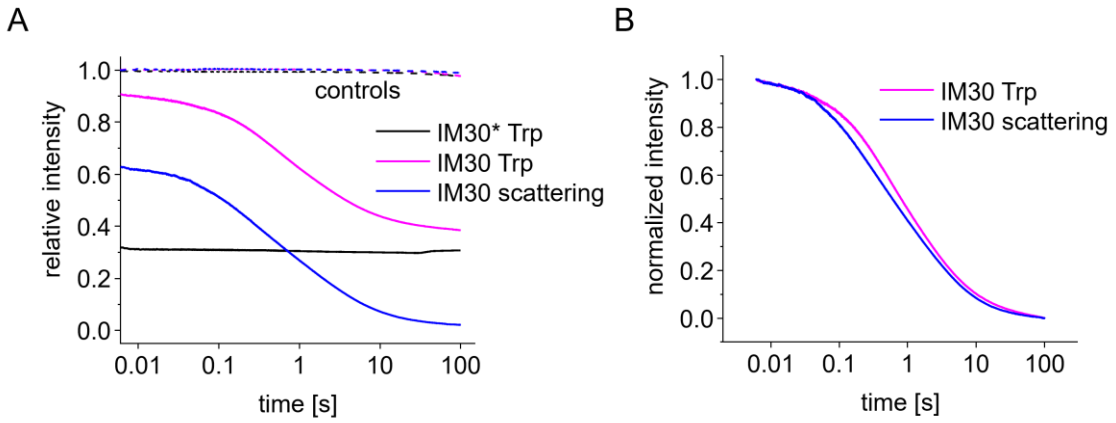

***Figure 3.1-9**: IM30 unfolding monitored by turbidity and Trp fluorescence. IM30 wt (dark and light blue) and IM30* (black) was mixed 1:1 with 8 M urea (solid lines) and with buffer as control (broken lines). The unfolding process was followed by Trp-fluorescence (black and dark blue) for both proteins and by turbidity at 325 nm for the IM30 wt (magenta). (A) The measured detector signal was normalized to the signal obtained at t= 6ms (dead time of the instrument) in absence of urea for better comparison. (B) For IM30 wt, additionally the signals were normalized to the value at 6 ms and 100 s, respectively, to highlight the slight lag in the fluorescence signal. All kinetic unfolding experiments were conceptualized and performed b* [redacted]

The change in Trp-fluorescence is a very fast process in case of IM30*. Most of the signal decay is lost in the dead time of the instrument (about 6 ms). The final fluorescence is about 30% of the value obtained with the control, in reasonable agreement with the values measured after 15 min in the steady-state fluorescence measurements (Figure 4B). In contrast, the fluorescence signal

decays much slower in case of IM30 wt, and, importantly, slightly lags behind the scattering signal (Figure 9B). This clearly shows that tertiary structure changes occur only after disassembly of the large IM30 oligomers. In the case of the wt protein, ring disassembly, measured via scattering, and monomer unfolding, determined via Trp fluorescence changes, occur nearly simultaneously, at least after 6 ms (Figure 9B), indicating that IM30 wt immediately unfolds at 4M urea, if not part of the barrel, as *e.g.* observed as the fast Trp fluorescence decay in case of IM30*.

3.1.3.8. A 3-state model describes IM30 unfolding

The experimental data indicate that denaturation of IM30 wt occurs in two major steps: (i) oligomer disassembly at low urea concentration and (ii) protein unfolding at higher urea concentrations. In order to support this interpretation, we analyzed our experimental data based on a two-step model. In this model, the different species adopted by the wt protein are the native, oligomeric state (N), an intermediate state (I) and a completely unfolded state (U).

In the analyses we used the relative scattering signal as approximation for the barrel still present (N). With this approach, barrel disassembly itself does not have to be modeled.

The ratio between the intermediate state (I) and the unfolded state (U) is defined by an equilibrium constant K, which depends on the urea concentration (see the Methods section). The urea concentration at which K=1, thus I and U are present at equal concentrations, is referred to as c_{50}.

Fitting our model to the normalized Trp fluorescence and CD signals simultaneously yielded a c_{50} of 3.0 ± 0.1 M for IM30 wt. The fraction of IM30 in the intermediate state (I) is maximal at 2.5 M urea amounting to about 60 %. Thus, when using urea to destabilize the IM30 structure it is not possible to solely disassemble IM30 barrels completely without simultaneously starting to unfold I further into U, at least under equilibrium conditions.

In case of IM30* and $IM30_{26\text{-}156}$, the N state (absence of urea) corresponds to small oligomers, at most tetramers[104]. Here, we tentatively applied a simplified two state model between a native (N') and an unfolded state (U).

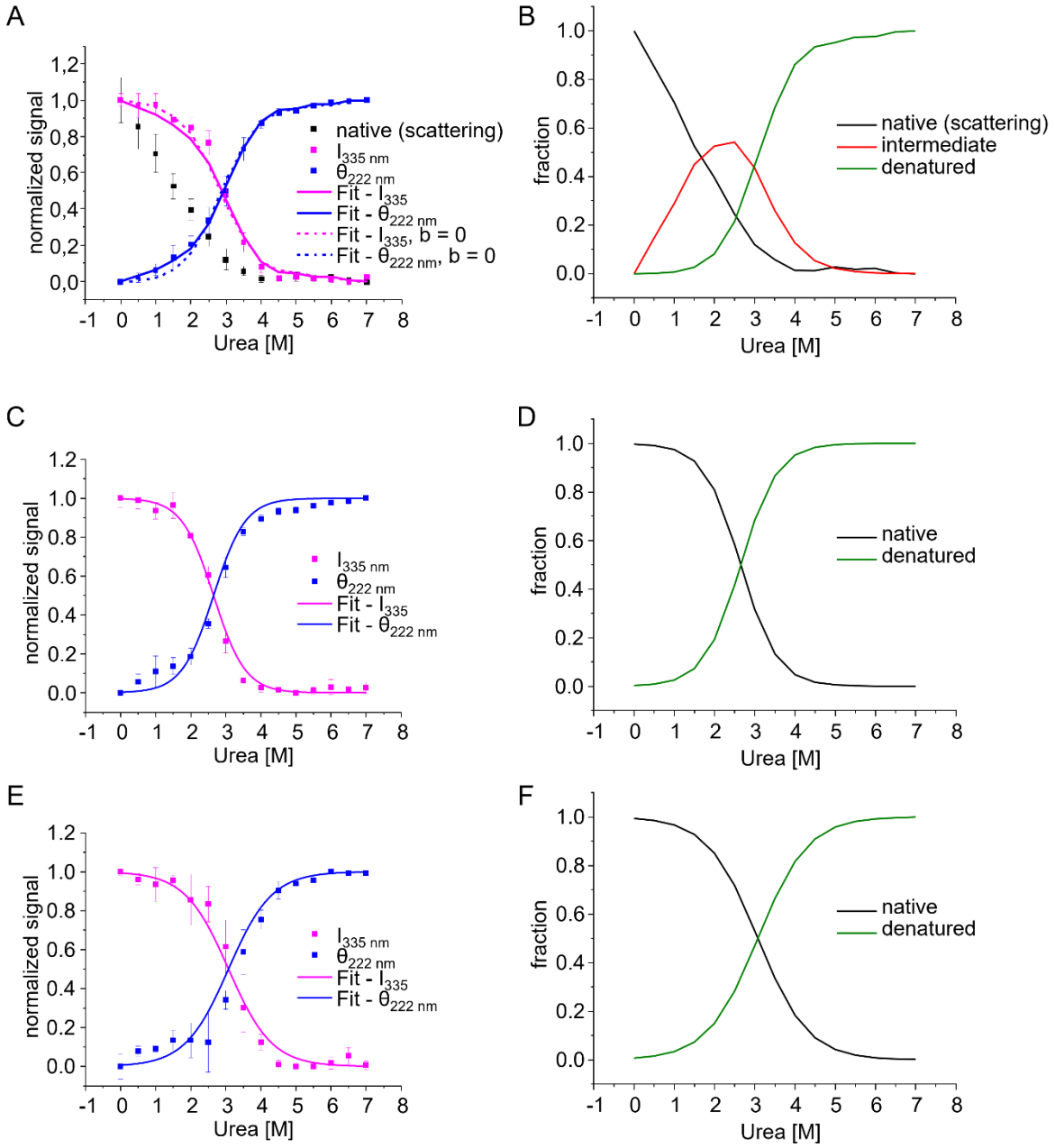

***Figure 3.1-10**: Global fit of experimental data to a 3-state model of urea induced IM30 destabilization. (A) Global fit of a 3 state model for IM30 wt (A, B) and a 2 state model for IM30* (C, D) and IM30$_{26\text{-}156}$ (E, F). (A, C, E) normalized Trp intensity and CD signal at 222 nm with normalized experimental data (squares) and corresponding fits (line). (B, D, F) Calculated fractions of IM30 states at increasing urea concentrations based on fitting results. Oligomeric barrel structure – native state, equivalent to the normalized scattering signal (black), monomer – intermediate state (red), denatured state (green). The error bars represent SD, n=3.*

Thus, any potential contribution of dissociation of small oligomers to the observed denaturation curve was not taken into account in the model. Yet, considering the complete dissociation of the large barrel at 3 M urea, it appeared likely that tetramers or smaller sized oligomers are dissociated well below this urea concentration. We termed the initial state in this case N' in order to distinguish it from the initial, oligomeric state of IM30 wt (N). Indeed, this simplifying model describes the measured curves very well in both cases.

Overall, the denaturation curves of IM30* and $IM30_{26\text{-}156}$ are quite similar. However, the analyses revealed slight difference in the stability towards urea: the transition from (N`) to (U) was observed at c_{50}=2.65 ± 0.03 M urea for IM30* and at c_{50}=3.1 ± 0.1 M urea for $IM30_{26\text{-}156}$. For the IM30 wt, a value similar to $IM30_{26\text{-}156}$ was determined with c_{50}=3.0 ± 0.1 M.

Taken together, our model is able to capture the characteristic transitions observed in our experiments (Figure 10). Unwinding of the coiled-coil, monitored by Trp fluorescence changes, and unfolding of the helices occur simultaneously, with a c_{50} of around 3 M in all three investigated IM30 variants. A similar unfolding behavior of IM30* and $IM30_{26\text{-}156}$ was expected, since in both cases the folded entity is mainly the coiled-coil region. However, the higher molar ellipticity of IM30* compared to the truncated variant indicates that parts outside of aa 26-156 contain short or temporary α-helical structures. In case of the wt, the observation that the unfolding process is very similar to unfolding of the truncated variant suggests that the intermediate I is a monomer/small oligomer with largely unfolded helices α4-6. If these regions were still folded after disassembly of the ring, they would have to be similarly stable as the coiled-coil region in helices α1-3 to adhere to the observed two-step unfolding mechanisms. This appears unlikely, considering the structure of IM30* with its largely unfolded helices α4-6[104] and the completely unfolded structure of the truncated variant α4-6[137]. Furthermore, the analyses of the experimentally determined curves also indicate that the secondary structures of monomers incorporated in the ring (N) *vs*. the intermediate (I) differ. In the fitting process not only c_{50} was obtained but also two parameters (*a* and *b*) which contain information about the relative value of the specific magnitude of fluorescence (*a*) and CD (*b*) for the different states. The fitted parameter *a*=0.81 ± 0.03 reflects $(F_I\text{-}F_U)/(F_N\text{-}F_U)$, suggesting that for IM30 wt about 80% of the total fluorescence change measured between 0 and 7 M urea occurs upon unfolding of I, while 20% occurs upon disassembly of the barrel. In this case, based on the analysis of solvent accessibility of Trp71 in the ring and the monomer, indeed some change

observed in the steady-state fluorescence characteristics (**Figure 3.1-5**) can be rationalized. Also, the fluorescence of IM30* in absence of urea seems to be somewhat lower than for IM30 wt (Suppl. Figure 2). The fitted parameter b=0.24 ± 0.03 reflects $(c_I\text{-}c_N)/(c_U\text{-}c_N)$, and thus about 24% of the total change in CD signal measured between 0 and 7 M urea occurs upon disassembly of the barrel, while 76% occurs upon unfolding of I. When the intermediate I reflects a monomer that is as structured as in the ring, the parameter b would be zero. To test whether a monomer with secondary structure indistinguishable from the wt (when embedded in the ring) is compatible with the data, we modified the fitting routine, and set b = 0. The corresponding fitted curves did not capture the changes in secondary structure observed at low urea concentrations (blue dashed curve in **Figure 3.1-10**A). Furthermore, the 24% decrease in the relative CD signal between N and I nicely agrees with the differences in CD spectra observed at 0 M urea for IM30 wt and IM30*: here, IM30 wt has a molar ellipticity about 29% higher than IM30* (**Figure 3.1-6**B), which likely reflects changes between the monomer embedded in the ring (wt) *vs*. the released monomer (IM30*). Overall, these findings strongly support the assumption that the IM30 helices α4-6 unfold independently and unfolding of helices α4-6 is not (directly) connected to unfolding of the structured core formed by the helical hairpin α1-2. Furthermore, the data suggest that helices α4-6 are folded only in the context of barrel formation.

3.1.4. Conclusion

Despite initial studies involving chaperone-mediated disassembly and destabilizing mutations[130,143], assembly and disassembly of IM30 oligomeric structures are poorly understood. Yet, to eventually elucidate the IM30 function, these processes need to be delineated. While partial unfolding of IM30 monomers during (or after) barrel disassembly was indicated, based on analyzes of IM30 variants, it remained unclear whether α-helix formation and assembly of oligomeric structures are coupled. Our results now show that the IM30 protein retains the structure of its α-helical coiled-coil domain during and after disassembly of the higher-ordered oligomer. Furthermore, the helices α4-6 are unstructured when not assembled in a barrel, in excellent agreement with recent analyses of the isolated α4-6 fragment[104,137]. Even though it is possible using urea to disassemble oligomeric structures and liberate protomers, our results clearly show that it is

impossible to fully destabilize all oligomeric structures without also starting to unfold the coiled-coil structure in the monomer.

IM30, as well as PspA, are bacterial ESCRT-III superfamily members and can serve as manageable models to understand assembly of ESCRT-III proteins in general. Based on the here presented analysis, great care must be taken when trying to select experimental conditions involving destabilized ESCRT-III-oligomers, since an equilibrium between oligomeric, intermediate, and unfolded states may need to be accounted for.

Furthermore, the here described analyzes of a bacterial ESCRT-III protein has important implications for understanding the assembly and dynamic structural (re)arrangements of ESCRT-III proteins in general. The driving force for ESCRT-III-mediated membrane remodeling in eukaryotes has been suggested to involve protomer exchange in hetero-oligomeric assemblies by Vps4 coupled to ATP-hydrolysis[144–147]. This was hypothesized to lead to changes in the tendency of membrane bound ESCRT-III proteins to form flat spirals, buckling spirals and rod-like structures[148–150]. It is still under debate how protomers are recycled after removal from the oligomer by Vps4 and our understanding of these processes is still rather macroscopic and lacks molecular detail[151]. Likely, for efficient refolding some residual structure that is stable also outside the oligomeric structure, needs to be preserved that can be recognized, leading to binding and incorporation into an oligomer. Our results now show that such a stable intermediate structure exists (at least) for the ESCRT-III family member IM30 after destabilizing the oligomeric structure by urea and that it is constituted by a conserved feature of the ESCRT-III protein family, the helices α1-3 coiled-coil. The unstructured part of the monomer, on the other hand, leads to an entropic penalty in the process of barrel formation. This is expected to lower the thermodynamic stability of the barrel compared to formation from monomers with preformed helices. Since dynamic oligomer (dis)assembly appears to be crucial for the function of ESCRT-III proteins, the barrel should be not too stable, in agreement with the now observed barrel disassembly at low urea concentration. Thus, the here noted formation of a stable, structured core (helices α1-3) in combination with highly destabilized parts (helices α0, α4-6) likely ensures proper and dynamic (dis)assembly of IM30 oligomers *in vitro*, and likely also *in vivo*.

3.2 IM30 monomers form biomolecular condensates upon barrel disassembly

3.2.1. Introduction

The inner membrane associated protein of 30 kDa (IM30), also known as the *vesicle inducing protein in plastids 1* (VIPP1), is involved in the biogenesis and maintenance of thylakoid membranes (TM) in cyanobacteria and chloroplasts [90,91,95]. IM30 monomers have a high intrinsic propensity to oligomerize spontaneously[138]. IM30 homo-oligomerization results in the formation of a variety of large barrel and/or tube structures which bind to negatively charged membranes[96,129,139]. Changes in the Mg^{2+} concentration[105] or pH[135] affect the protein structure and enable IM30 to mediate membrane fusion, at least in *in vitro*[55]. IM30 oligomers rearrange upon binding to model membranes to form large, membrane-stabilizing carpet structures[104]. Furthermore, in solution lipid bilayers are soaked into IM30 barrels/rods, and the membrane surfaces bind to the inner side of barrel-/tube-like structures[129]. IM30 has recently been identified to be a bacterial member of the ESCRT-III superfamily, members of which form large homo- and hetero-oligomer structures that are crucially involved in membrane remodeling[96,97,99].

The *endosomal sorting complex required for transport* (ESCRT) is crucially involved in membrane sealing[134] and both normal-[152,153] and inverse-topology [153,154] membrane scission for many different processes throughout the cell including the biogenesis of multivesicular bodies, cytokinesis, release of viruses from host cells and membrane repair[145,151,155]. The ESCRT family consists of 5 core complexes ESCRT-I, -II, -III, ALIX, and the AAA+-ATPase VPS4[151,154,156]. ESCRT-0 is despite its name not a part of the core machinery for scission but involved in regulated membrane targeting[155–157]. ESCRT-I can bind to upstream components such as ESCRT-0, CEP55, and Gag and it binds downstream to ESCRT-II which functions as bridging and activator component to recruit ESCRT-III via its winged helix (WH) domain, whereas ALIX by itself is also capable of binding upstream components and represents an alternative pathway for recruitment of ESCRT-III proteins via its BRO1 domain[151,154,158]. Finally, the ESCRT-III complex is directly involved in the membrane budding and scission process involving ESCRT-III polymer remodeling and disassembly by the AAA+-ATPase VPS4[151,154–156]. The structures formed by ESCRT-III proteins have been exhaustively studied in the recent years and guided the understanding of membrane scission by ESCRT-III polymers[145,155,159].

Central to all ESCRT-III proteins is a coiled-coil formed by helices α1 and α2[99]. All ESCRT-III superfamily members have at least four, maximal seven, α-helical regions. The structure of the IM30 monomer consists of seven α-helical regions (α0-6), with α1 and α2 forming the coiled-coil structure conserved in all ESCRT-III superfamily members. Helix α3 is a direct extension of α2, and the exact boarder between these helices is ill defined. Helix 6 is located after a flexible linker region at the very C-terminus and is unresolved in the recently published structural models of IM30 barrels[96].

The models for IM30 barrels have rotational symmetries ranging from C14 to C18 consisting of 6 (C14-16) or 7 (C17-18) layers with varying diameter across each layer. The upper most layer is always the narrowest while mid layers have the largest diameter giving the structure a dome-like shape. The inside of the barrel is lined with hydrophobic surfaces provided by the horizontally stacked amphipathic helix 0. The outside of the barrels shows characteristic spikes of helix 5 protruding from the barrels surface and forming a conserved contact side with the hairpin end of the coiled-coil on the third next monomer of the same layer. Multiple contacts at interfaces conserved in the ESCRT-III superfamily connect individual protomers inside barrel-layers, as well as across different layers. Conserved hinge regions as well as flexibility in the presence and position of individual helices, especially helices 4 and 5, result in different monomer structures inside a single barrel-type oligomer, plus allow the formation of oligomers with a variety of sizes and symmetries[96,99].

Instead of barrel structures, the model of PspA, another bacterial ESCRT-III member, shows the formation of tube-like structures, which resemble the reported models of eucaryotic ESCRT-III polymers[98]. The *Phage Shock Protein* (Psp) response in *E. Coli* is activated in response to phage infections and other stress conditions to maintain the proton motive force (PMF) across the cytoplasmic membrane[124]. It involves sensing of stress signals by membrane integral proteins PspB and PspC which then bind to PspA[160], resulting in dissociation of the PspA-PspF complex and activation of the sigma 54 dependent expression of the *pspABCDE* operon by PspF[161–163]. Furthermore, PspA binds to negatively charged membranes[164] and was shown to protect membranes against various stress conditions[125,165,166], including proton leakage[167], all traits that were similarly shown to be shared with IM30 in the context of thylakoid membrane maintenance[55,92,104,168–170].

Eukaryotic ESCRT-IIIs and IM30 have been shown to interact with VPS4-ATPase and HSP70/DnaK, respectively, which results in disassembly of the large oligomeric structures *in vivo* as well as *in vitro*[130,143,146,147]. IM30 oligomer disassembly results in unfolding of all helices except the central coiled-coil-forming helices α1-3, resulting in a largely unstructured monomers with an extended intrinsically disordered region (IDR)[104]. *In vivo,* IM30 forms *punctae* near the TM, which are dynamically forming and dissolving with increased occurrences after high light stress[107,112]. Similar stress induced formation of punctae at the plasma membrane of bacteria was also observed for other bacterial members of the ESCRT-III family, *i. e.* PspA[171,172] and LiaH[173]. While a dynamic (re)localization of cytosolic *vs*. membrane-bound IM30 appears to be important for the protein´s *in vivo* function[107], the nature and exact role of the observed *punctae* still remains unspecified.

In this study we aimed to elucidate the effect of IM30 oligomer destabilization on the formation of *punctae* by applying fluorescence microscopy to labeled IM30 variants expressed in *Synechocystis* cells. We then continued to discuss a type of supramolecular assembly hitherto unreported to be formed by IM30, or any other ESCRT-III family member to our knowledge and assessed the physiological relevance of the required conditions for its formation.

3.2.2. Results

3.2.2.1. In vivo formation of IM30 punctae does not require an IM30 barrel structure

In living cyanobacterial cells, IM30 has been shown to form *punctae* in close proximity to internal membranes[107,112], a feature conserved in all bacterial members of the ESCRT-III superfamily analyzed thus far[171–173]. Consequently, when we transiently expressed C-terminally mVenus-labeled IM30 in *Synechocystis*, formation of fluorescent IM30 *punctae* was observed (**Figure *3.2-1***). Nevertheless, the exact nature of these *punctae* and their assembly structure are still ill defined, as well as their *in vivo* function.

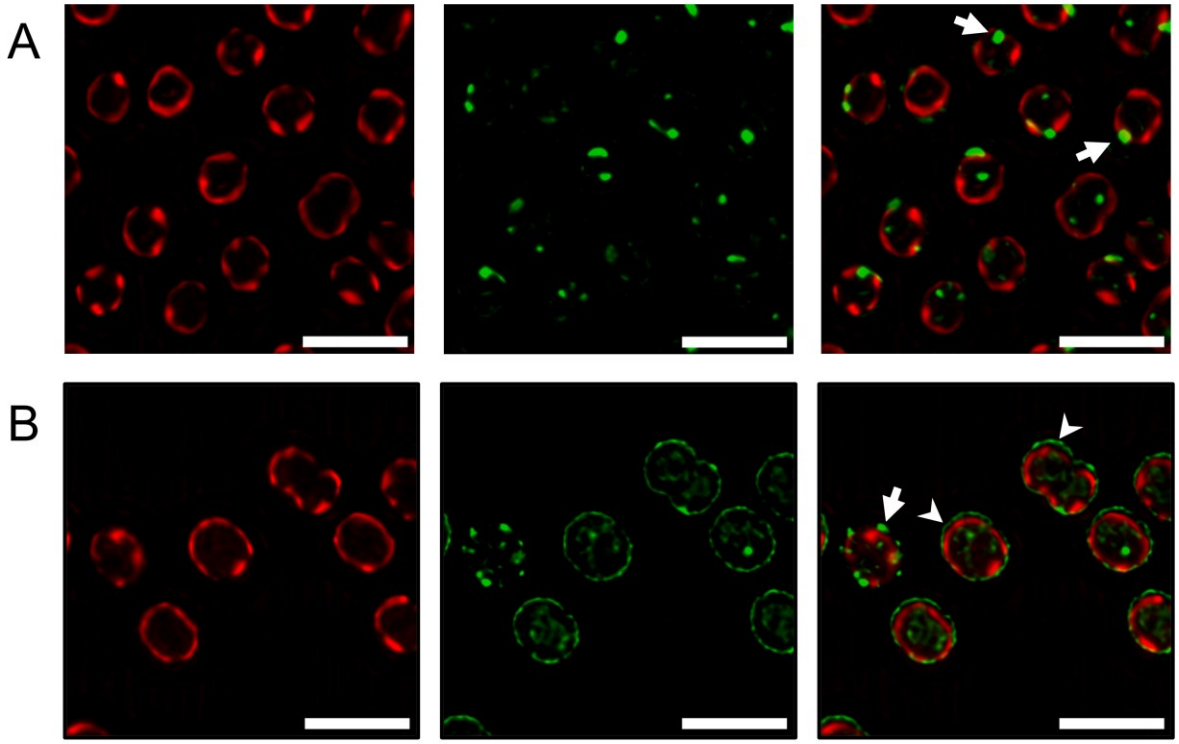

Figure 3.2-1: Fluorescence microscopy images of *Synechocystis* cells expressing mVenus-tagged IM30 or IM30*. *Synechocystis* expressing IM30-mVenus (A) and IM30*-mVenus (B). Shown are the thylakoid channel in red (left), mVenus channel in green (middle) and an overlay of both channels (right) of structured illumination evaluated images (SIM^2 strong). White arrows mark *punctae*, white arrowhead indicates a patches and sheet-like protein localization near the plasma membrane. The scale bar is 3 µm. All *in vivo* fluorescence microscopy experiments were conceived and performed in collaboration with [redacted] nd [redacted] (University of Liverpool, UK).

As all members of the PspA/IM30 family appear to bind to membranes, it may well be possible that the observed *punctae* structures in fact represent membrane-covering protein carpets, as observed *in vitro* when the *Synechocystis* IM30 protein binds to solid supported membrane surfaces[104]. Furthermore, all members of the ESCRT-III family appear to form large

supercomplexes in solution[99,158], and thus the observed *punctae* might simply represent large, assemblies of such supercomplexes.

To first test whether the formation of higher-ordered oligomers, *i.e.* rings and/or rods, is required for the *in vivo* formation of *punctae*, we transiently expressed C-terminally fluorescently labeled IM30* (IM30*-mVenus) in *Synechocystis*. IM30* contains mutations in a region that mediates contacts between IM30 monomers, and thus, the protein does not form large, ordered protein supercomplexes anymore[111]. As observed before for the wt protein, upon expression of IM30* in *Synechocystis* we also observed the formation of *punctae,* and thus, *punctae* formation does not depend on the propensity of IM30 to form the prototypical, large, structured supercomplexes (**Figure *3.2-1***).

However, it has recently been shown that IM30 barrels disassemble when binding to membrane surfaces[104], and as the *punctae* observed *in vivo* are in close proximity to internal membranes, these structures might represent membrane covering carpets.

To better visualize the exact structure and localization of the *in vivo* formed *punctae*, we next analyzed *punctae* formation in *Synechocystis* via super-resolution microscopy. Based on fluorescence image stacks and the 3D-rendered images of *Synechocystis* cells expressing IM30wt-mVenus, the *in vivo* forming *punctae* are located close to internal membranes, yet do not form membrane covering carpets, at least not under the tested experimental conditions (**Figure *3.2-1***, **Figure 3.2-2**). In fact, the *in vivo* formed structures have a globular shape, which resemble the spherical shapes of membraneless organelles (MLOs). MLOs are condensates that form *in vivo* in several organisms due to phase separation, which can be coupled to additional phase transitions, and their formation often involves intrinsically disordered proteins (IDPs) or protein domains consisting of intrinsically disordered regions (IDRs)[58,89,174]. Importantly, also with the IM30*

protein we observed *punctae* formation, demonstrating that the contacts that mediate the formation of and stabilize IM30 barrels are not crucial for *punctae* formation.

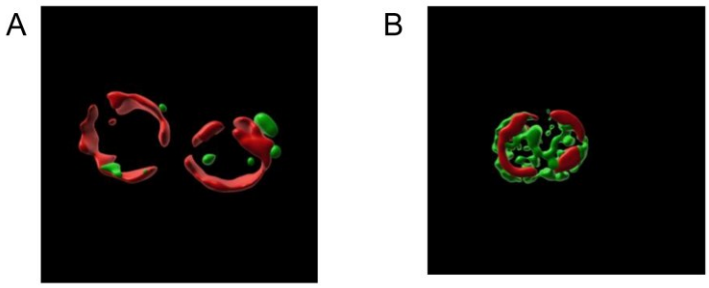

Figure 3.2-2*: 3D-rendering of TM and mVenus fluorescence signals. (A) Synechocystis cells expressing IM30wt-mVenus with the TM in red and mVenus signal in green. (B) Synechocystis cells expressing IM30*-mVenus with the TM in red and mVenus signal in green.* All *in vivo* fluorescence microscopy experiments were conceived and performed in collaboration with [redacted] and [redacted] (University of Liverpool, UK).

3.2.2.2. IM30 condensate formation in vitro requires barrel disassembly

Biomolecular protein condensates are assemblies of proteins in solution which can form through the separation of the solution into a phase of high protein concentration (observed as condensates) and a phase of low protein concentration. Condensate formation requires a minimal critical protein concentration and can be induced by changes of the environmental conditions, for example changes in pH, ionic strength, molecular crowding, or temperature, all resulting in altered intermolecular interactions between biological polymers and/or the solvent [58,174–176].

Generally, the cytoplasm of a cell is a crowded environment filled with macromolecules that occupy 20-30% of the cell's volume[177]. Therefore, *in vitro* studies considering a cellular environment typically use macromolecular crowding agents, such as polyethylene glycol (PEG) to mimic crowding as observed within a cell, and the effect of crowding has become recognized as an important factor for the study of biomolecular condensates[178]. The macroscopic demixing of fluids inside these crowded environments is observed as the formation of liquid-like condensates. Multivalent proteins as well as disordered proteins drive the formation of liquid-like condensates by multivalent, transient intermolecular interactions[58,175,176]. Yet, IM30 monomers are involved in multiple stable intermolecular interactions resulting in the formation of oligomeric barrel structures[96]. Furthermore, these IM30 oligomers can stick to each other, stack, and even form rods in solution[129–131,139], which can be promoted by other additives such as Mg^{2+} ions[105]. Consequently,

large aggregates formed when protein-protein interactions were promoted under crowding conditions and the solubility of the protein was reduced by lowering repulsive electrostatic interactions at intermediate ionic strength and shifting the solution closer to the proteins isoelectric point at pH 5.5 (pI_{IM30*} = 5.75) (**Figure 3.2-3**A, B).

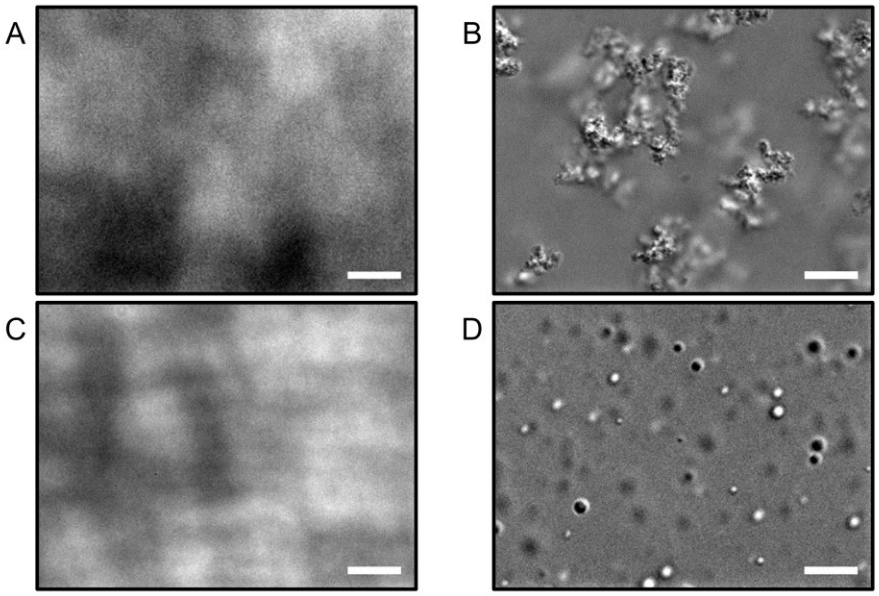

Figure 3.2-3*: Condensate formation of IM30 wt in absence and in presence of 3M urea visualized via DIC. 32 µM IM30wt at pH 7.5 (A) and at pH 5.5, 100 mM NaCl, 10 % PEG (B) in 10 mM phosphate, 10 mM HEPES. IM30wt at pH 7.5 (C) and at pH 5.5, 100 mM NaCl, 10 % PEG (D) in 3 M urea, 10 mM phosphate, 10 mM HEPES. Scale bar 10 µM. Representative images of n = 3 independent experiments are shown.*

To next determine whether the IM30 barrel structure disfavors condensate formation under the applied experimental conditions, we destabilized the IM30 barrels via the addition of 3 M urea, which results in smaller IM30 oligomers/monomers (section 3.1). We have recently demonstrated that at this urea concentration the IM30 barrel structure, yet not the central α1-3 coiled-coil structure, is largely disassembled (section 3.1). When the barrels were disassembled by urea, formation of liquid condensates by IM30 was observed *in vitro* (**Figure 3.2-3**C, D), and thus, the barrel assembly indeed appears to counteract condensate formation.

Since formation of condensates can be often observed for proteins at crowding conditions, regardless of a real physiological relevance[179], we next investigated IM30 condensate formation without crowding agent in response to physiologically relevant pH changes in greater detail.

3.2.2.3. Formation of IM30* condensates at acidic pH

As the above presented results strongly suggest that barrel disassembly promotes condensate formation, we next used the mutant IM30* that does not form barrel or rod structures anymore[104] to confirm condensate formation in absence of urea. Turbidity measurements followed by DIC microscopy enabled us to monitor condensate formation at varying pH at different protein concentrations, yet in complete absence of urea, salt, and any crowding agent.

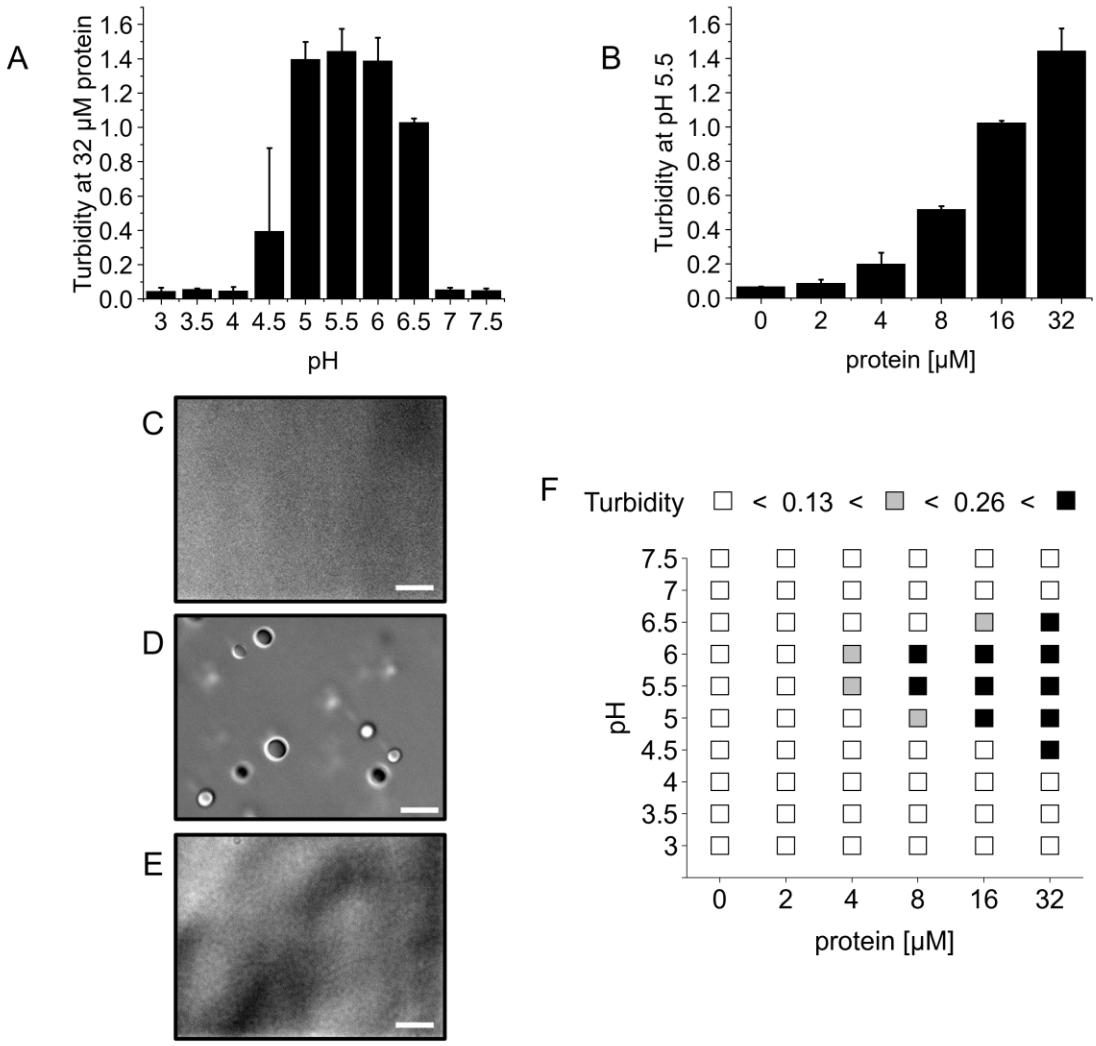

***Figure 3.2-4**: pH-induced IM30* condensate formation. (A) Turbidity measurements of 32 µM IM30* at varying pH. (B) Turbidity measurements of IM30* at pH 5.5 and varying protein concentrations. (C-E) Selected DIC images of 32 µM IM30* at pH 7.5 (C), pH 5.5 (D) and pH 3.5 (E). (F) Phase diagram for IM30* at varying pH and protein concentrations. Error bars represent SD (n = 3 biological replicates).*

At a constant protein concentration of 32 µM we were able to observe the formation of IM30* condensates via DIC microscopy, coupled to an increase in turbidity, already by only slightly lowering the pH to about 5.5 (**Figure 3.2-4**A, C, D). Further acidification below pH 4 resulted in a return to the one phase regime and base levels of turbidity (**Figure 3.2-4**A, E). Turbidity at a constant pH of 5.5 increased with protein concentration and indicated a saturation concentration in the lower µ-molar range (**Figure 3.2-4**B). Increasing the protein concentration above a critical protein concentration likely resulted in increased volume fractions of the condensed phase while keeping a constant protein concentration in the dilute phases as described for simple one-component systems[60]. Summarizing multiple turbidity measurements into a phase diagram (**Figure 3.2-4**F) revealed a reentrant phase transition, which is characterized by at least two phase transitions, in response to pH with a clear preference for the formation of condensates at a pH around 5.5-6.0, which is close to the calculated isoelectric point (pI) of IM30* (5.75). Condensate formation in response to pH has been predicted in simulations to occur typically around the proteins pI[180]. A proton gradient is maintained across the TM[181] and because IM30 senses and protects membranes against proton leakage[104,135] pH 5.5 represents a physiologically relevant range.

3.2.2.4. Formation of IM30* condensates in crowded environments with NaCl

Apart from pH, other cellular parameters are known to trigger and modulate condensate formation *in vivo* as well as *in vitro*, including temperature[182], molecular crowding[178], and ionic strength[183,184]. To investigate whether IM30* phase separates to form condensates under physiologically relevant conditions and could be discussed in relation to formation of punctae *in vivo*, we next analyzed phase separation triggered by increased ionic strength as well as molecular crowding. Thus, we next monitored condensate formation at a constant pH of 7.6, which is similar to cytosolic pH values of cyanobacteria measured under growth at neutral pH[185]. In the presence of 10% PEG as crowding agent and at increasing NaCl concentrations, IM30* formed condensates already at low ionic strength (**Figure 3.2-5**A, C, D).

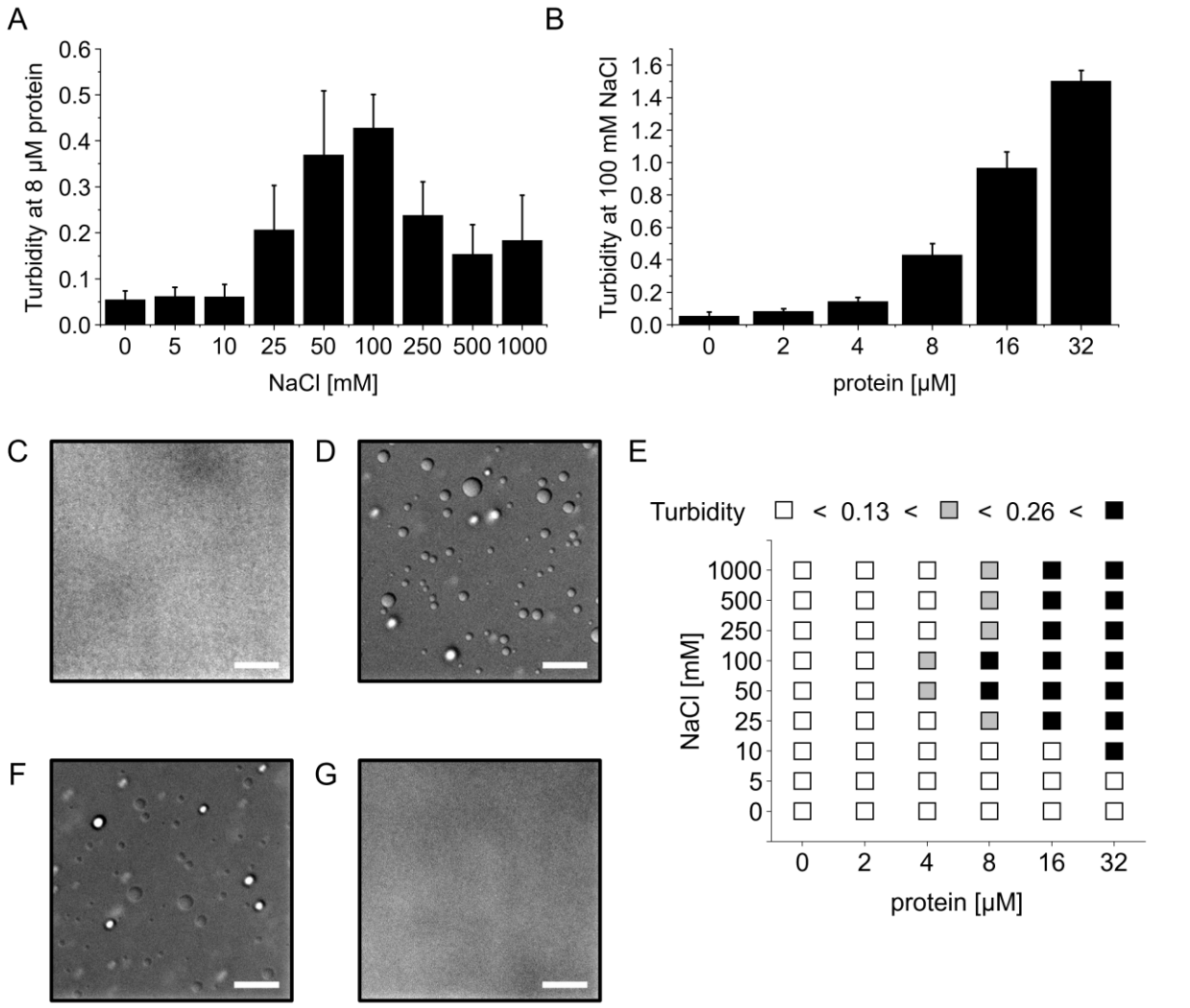

Figure 3.2-5*: IM30* condensate formation at varying NaCl concentrations. (A) Turbidity measured at 8 µM IM30* in presence of 10% PEG at increasing NaCl concentration. (B) Turbidity measured at 100 mM NaCl in presence of 10% PEG at increasing IM30* concentration. DIC microscopy images of 32 µM IM30* at (C) 0 mM NaCl and (D) 100 mM NaCl in presence of 10% PEG. (E) Phase diagram of IM30* at varying NaCl concentrations and protein concentrations in presence of 10% PEG. (F, G) DIC microscopy images of 32 µM IM30* at (F) 1000 mM NaCl in presence of 10 % PEG and (G) 100 mM NaCl in absence of PEG. All measurements were performed in 20 mM HEPES at pH 7.6. Error bars represent SD (n=3 biological replicates).*

Similar to our data on pH induced IM30* condensates (**Figure 3.2-4**B), our turbidity data collected in presence of 10% PEG at 100 mM NaCl with increasing protein concentrations suggested a saturation concentration in the lower µ-molar range for PEG-NaCl induced condensate formation (**Figure *3.2-5***B). The phase diagram assembled from multiple measurements (**Figure *3.2-5***E) is reminiscent of *high salt* phase separation[186]. Here the term "high salt" does not refer to a defined salt concentration, but rather a minimal critical salt concentration that is required for phase

separation and condensate formations, opposed to *low salt* phase separation, where a reduction in the salt concentration below a maximum critical concentration is required for condensate formation[186]. At salt concentrations below 10 mM, we detected no increase in turbidity for all tested concentrations suggesting that a minimal concentration of 10-25 mM NaCl is required to induce condensate formation in presence of 10% PEG (**Figure 3.2-5**E). However, decreasing condensate formation was observed above 100 mM NaCl, which was most pronounced at 4 and 8 µM (**Figure 3.2-5**A, E), and to a lesser extent at 32 µM IM30 where condensates still formed at 1 M salt (**Figure 3.2-5**E, F). Increasing the NaCl concentration above a critical concentration first resulted in condensate formation, while further increasing the salt concentration disassembled these structures again, at least at 4 and 8 µM IM30*. Thus, there seems to exist both a lower and an upper critical NaCl concentration for condensate formation, which is known as *middle salt* phase separation[186]. Further extension of the phase diagram to even higher ionic strength might be necessary to make a clear distinction between *high salt* and *middle salt* phase separation. However, already from our data shown here it is evident that a lower critical salt concentration exists at 10-25 mM NaCl, and that condensate formation of IM30* is most enhanced at 100 mM NaCl, which is in a physiologically relevant range[187]. Noteworthy, in absence of a crowding agent, yet in presence of 100 mM NaCl, IM30* did not phase separate at physiological pH (**Figure *3.2-5***G). Since condensates are still formed at NaCl concentrations of 500 and 1000 mM, the interactions responsible for condensate formation are probably not entirely electrostatic in nature, which would lead to a much stronger inhibitory effect of intermediate NaCl concentrations on condensate formation, as observed for other proteins [184,188].

Electrostatic screening is thought to dominate at lower ionic strength in the physiological range whereas at higher ionic strength the salting-out effect becomes important[189]. Our phase diagram might show an overlap of these two effects as they correspond well to the area around 100 mM NaCl with the lowest saturation concentrations and the area at higher ionic strength with increased saturation concentration.

In summary, we could show that IM30 condensate formation is indeed relevant and should be considered when discussing *in vivo* experiments as IM30 condensates preferably form in a physiologically relevant range and deviations from optimal physiological concentrations negatively affect condensate formation propensity.

3.2.2.5. Dynamics of IM30 and IM30* condensates

Upon an initial formation of liquid spherical condensates, in some cases such structures can transition to more gel-like assemblies [178,190,191]. Whereas some condensates undergo such a transition as part of their physiological function[192], in other cases, changes in fluidity can indicate impaired function, finally leading to the formation of toxic aggregates[174,193–195].

Recently, IM30 *punctae* have been described to dynamically localize to damaged membranes *in vivo* in a manner that resembled Ostwald ripening[108]. Ostwald ripening stems from differences in Laplace pressure for condensates of different sizes resulting in net growth of larger condensates at the expense of smaller condensates. Thus, Ostwald ripening constitutes one of the potential mechanisms for condensate growth in the context of phase separation[196].

Although we thus far only observed condensate growth via coalescence as fusion events (**Figure 3.2-6**C), it does not exclude the relevance of Ostwald ripening *in vitro* and *in vivo*. Either way, the rapid exchange kinetics observed in the targeting of IM30 *in vivo*[108] would suggest that the *in vivo* observed *punctae* (compare **Figure *3.2-1*** and **Figure 3.2-2**) less likely resemble aggregates or a gel-like state, but rather resemble more liquid-like condensates. To describe the IM30 condensate´s state (fluid vs. gel-like) in some detail, we next monitored FRAP to follow the fluorescence recovery of photobleached condensates due to an exchange of bleached monomers in the condensate and unbleached monomers in the bulk solution.

We observed a fast recovery of the fluorescence signal to ~75% of the initial fluorescence after 1 minute and an almost full recovery (>90%) after 10 minutes (**Figure 3.2-6**A, B). This indicates a fluid-like nature of the condensates and a high fraction of mobile content in pH-induced condensates. Furthermore, the condensates were able to fuse resulting in spherical condensates after fusion within a second (**Figure 3.2-6**C) and were frequently wetting the glass surface of the chamber during observation in DIC microscopy experiments after prolonged incubation times (**Supplementary figure 8.2-1**). These are common indications for a liquid-like condensate state[197].

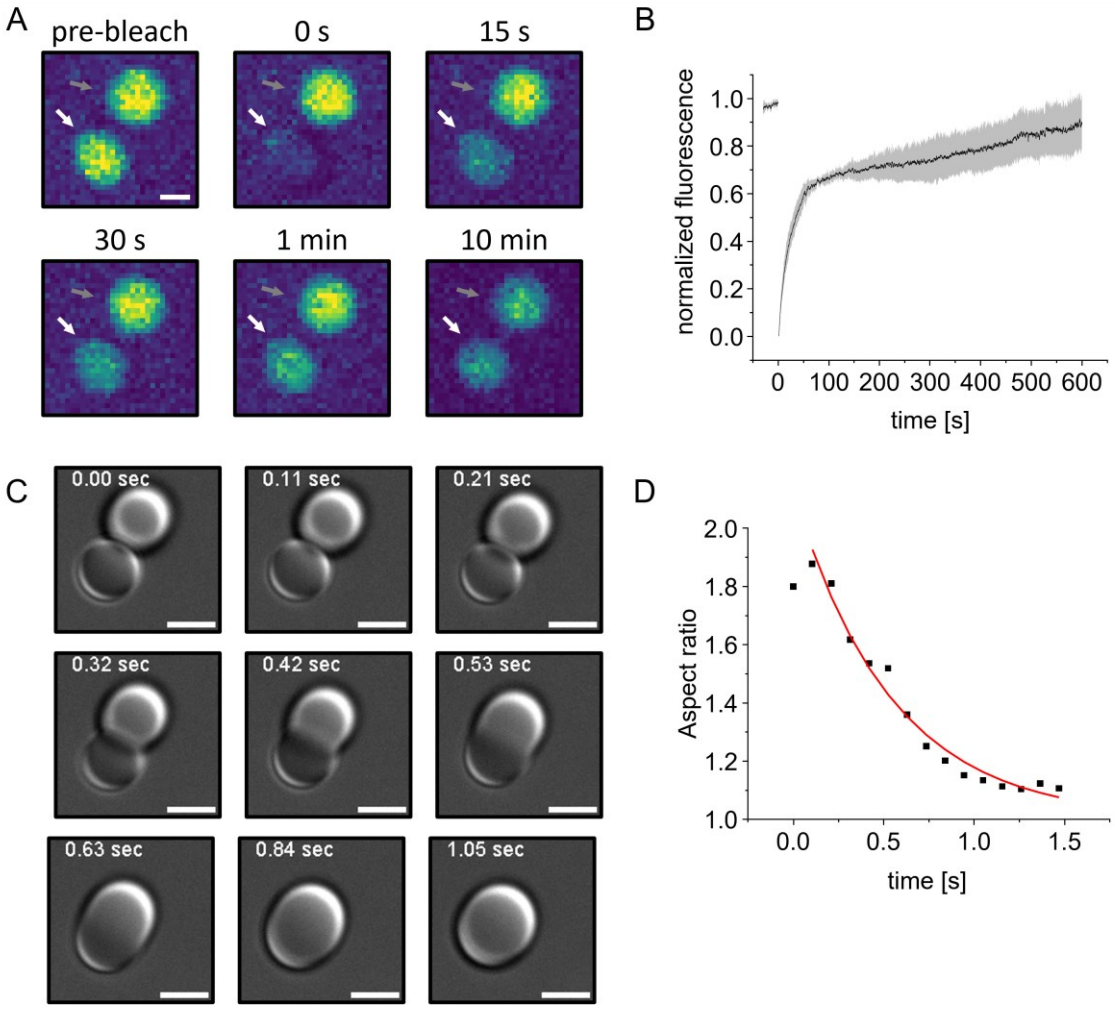

***Figure 3.2-6**: FRAP experiments and analysis of a fusion event of pH-induced IM30* condensates. (A) Fluorescence microscopy images of a fully bleached (white arrow) and a non-bleached (grey arrow) IM30* condensate before and after the bleach pulse. Non-bleached condensates were used as control to correct for acquisition bleaching. The scale bar is 2 µm. Error bars represent SD (n=3 biological replicates (N = 6 condensates)). (B) Normalized fluorescence intensity measured in FRAP experiments of IM30* condensates formed at pH 5.5, 10 mM HEPES, 10 mM Pi-buffer. (C) DIC microscopy snapshots of a fusion event. Time after condensates coming into contact is indicated in each image. The scale bar is 3 µM. (D) Aspect ratio (A.R.) of ellipse fitted to the condensate during the fusion event shown in (C) (black line) and the corresponding exponential fit (red line) with $\tau_{1/2}$ = 0.54 ± 0.03 s, $A.R._0$ = 2.12 ± 0.05 and R^2 = 0.976, n=1.*

To validate the liquid nature of the condensates and to compare their relaxation kinetics to other known biomolecular condensates, we analyzed the kinetics of the fusion event of the two condensates shown in **Figure 3.2-6**C and fitted an exponential function describing the changes in aspect ratio of the fusing condensates over time. Since relaxation time depends on condensate size, we opted to compare the relaxation time at the same length scale defined as geometrical mean,

$\ell = \sqrt{((\ell_{major} - \ell_{minor}) * \ell_{minor})}$, at t = 0 s [188]. For our condensate example we obtain that ℓ is about 5 µm and we obtained a characteristic relaxation time of $\tau_{1/2}$ = 0.54 ± 0.03 s, which is very close to measured values for LAF-1 with $\tau_{1/2}$ ~ 0.6 s at ℓ ~ 5 µm and shows that IM30 condensate dynamics are in the same order of magnitude as other biomolecular condensates.

When condensate formation was induced via lowering the pH, the resulting condensates were fluid in nature, as shown above. Yet, different condensate-inducing conditions can result in condensates that differ in fluidity and temporal stability against liquid- to gel-like transitions for a single condensate forming protein[198–200]. The cellular environment is reported to be 20-30% volume occupied and thereby represents a very crowed environment compared to standard aqueous buffer systems[177]. In the study presented here, we mimicked the crowded environment by addition of 10% PEG, a commonly used crowding agent in the study of biomolecular condensates[178]. Furthermore, we used the previously determined optimal concentrations for condensate formation of 100 mM NaCl (Figure 3.2-5) which represents an ionic strength in the physiological relevant range of *Synechocystis*[187]. Therefore, we analyzed FRAP using IM30* condensates formed at pH 7.6 in presence of 100 mM NaCl and 10% PEG as crowding agent, physiologically relevant conditions for our system[177,187,201].

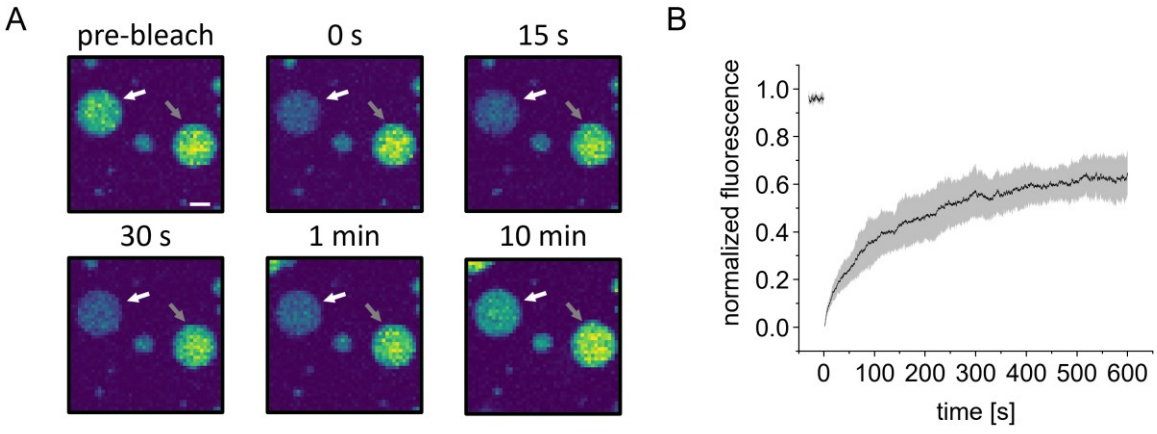

***Figure 3.2-7**: FRAP experiments with PEG/NaCl-induced IM30* condensates. (A) fluorescence microscopy images of a bleached (white arrow) and a non-bleached (grey arrow) IM30* condensate before and after the bleach pulse. (B) Normalized fluorescence intensity measured in FRAP experiments of PEG-NaCl induced condensates at 32 µM IM30*, 20 mM HEPES, pH 7.6, 10% PEG, and 100 mM NaCl. Non-bleached condensates were used as a control to correct for unwanted photobleaching. The scale bar is 2 µm; Error bars represent standard deviations of n=3 biological replicates (N = 6 condensates).*

In the FRAP experiments, the NaCl/PEG-induced IM30* condensates showed a lower recovery after 10 minutes compared to the condensates formed upon decreasing the pH (**Figure 3.2-6**B, ***Figure 3.2-7***B). A lower mobile fraction inside condensates indicated that NaCl/PEG-induced IM30* condensates have rapidly transitioned towards a more gel-like state. Nevertheless, condensates were still able to recover about 60% of their fluorescence signal and partially wetted the bottom glass surface (**Supplementary figure 8.2-2**). To test whether the addition of the crowding agent PEG had an effect on the exchange of monomers between condensate and the solution, we also induced condensates at pH 5.5 in the presence of PEG (Figure 8). While we observed fluorescence recovery within 10 minutes, the fluorescence signal was substantially slowed down (**Figure 3.2-8**) when compared to the pH induced condensates yet in absence of PEG (**Figure 3.2-6**), plus the signal was drastically decreased and did not reach a clear plateau. Therefore, the crowding agent PEG appears to affect the nature of IM30* condensates.

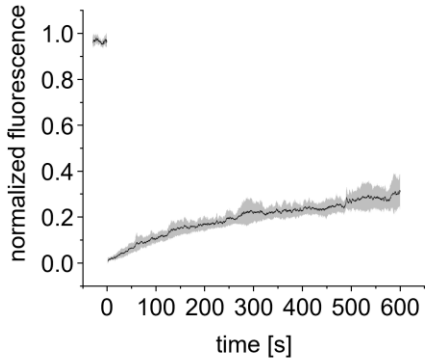

Figure 3.2-8: *FRAP experiment of pH-induced IM30* condensates in presence of PEG. Normalized fluorescence intensity measured in FRAP experiments of pH-induced condensates at 32 µM IM30*, 10 mM HEPES, 10 mM Pi-buffer, 10% PEG at pH 5.5; Error bars represent standard deviations for n=3 biological replicates (N = 6 condensates).*

PEG is a crowding agent commonly used for *in vitro* condensate formation, and the crowding condition itself was shown to induce phase separation of many proteins[178,202,203]. However, in some cases crowding agents were reported to interact specifically with proteins instead of solely providing a neutral environment triggering condensate formation[202]. Preferential incorporation, exclusion, or neutral partitioning of crowding agents to condensates can be tested via fluorescence microscopy using fluorescently labeled crowding agents[202,204]. Therefore, we used Cy5-labeled PEG to check for preferential partitioning of PEG into our condensates. When PEG interacts with the protein, a colocalization of the crowder with the protein in formed condensates is expected,

whereas an exclusive localization of the crowder in the solution is expected when the crowder does not (significantly) interact with the protein. We found that neither PEG/NaCl-induced nor pH-induced condensates with additional 10% PEG showed pronounced incorporation through attractive interactions or exclusion through repulsive interactions between IM30 and PEG supporting the suitability of PEG as a neutral crowding agent for our experiments [178] (**Supplementary figure 8.2-3**). Condensate formation induced by the addition of PEG appears to be triggered by the crowded environment rather than be induced directly by interaction of IM30 with PEG.

3.2.2.6. Disassembly of the IM30 barrel enables IM30 condensate formation

The barrel structure of IM30wt appears to inhibit the formation of condensates and leads to the formation of aggregates under conditions where IM30* readily forms condensates (compare **Figure 3.2-3**B and **Supplementary figure 8.2-8**, **Supplementary figure 8.2-9**, **Supplementary figure 8.2-10**, and **Supplementary figure 8.2-11**). We used urea to destabilize the barrel structures and compared condensate formation of IM30wt and IM30* (**Figure 3.2-9**) under otherwise identical conditions. Indeed, IM30wt forms condensates at conditions where it does not form large homo-oligomers anymore, and thus, the interactions driving condensate formation are likely identical for IM30wt and IM30*. When comparing the turbidity of IM30 and IM30* solutions in absence and presence of urea and in varying condensate-inducing conditions, we found that conditions promoting assembly are similar for both condensates and aggregates (**Figure 3.2-9**E). Our data do not indicate a significant difference between the turbidity stemming from condensate formation or by aggregation, that could only be distinguished by additional DIC microscopy experiments.

The large size of barrel structures of IM30 (> 2 MDa) inherently causes increased scattering when compared to the mutant IM30*. Therefore, there is a significant difference between IM30 and IM30* in the control at pH 7.5 (**Figure 3.2-9**E).

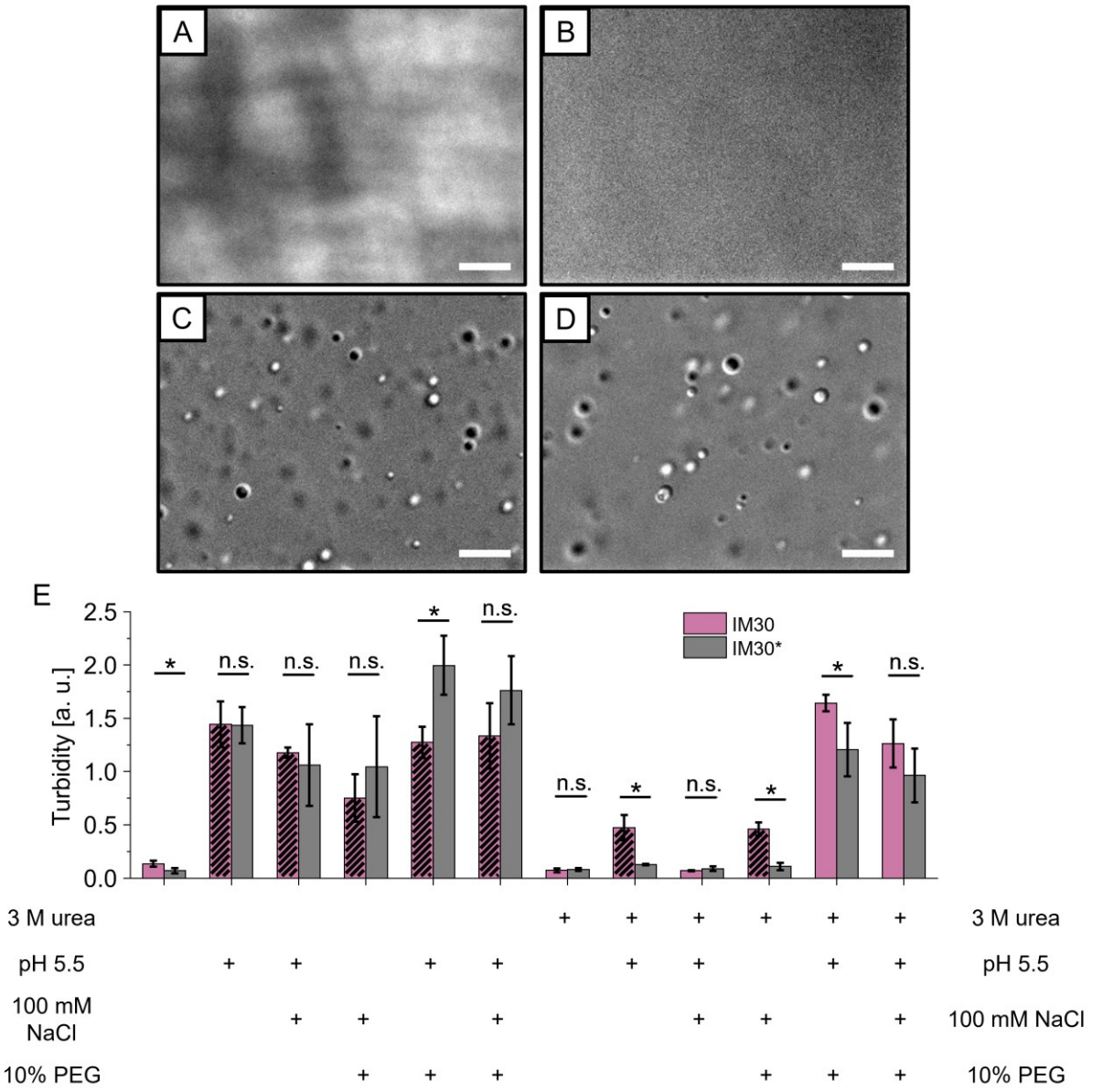

Figure 3.2-9: *Comparison of DIC images and turbidity measurements for IM30 and IM30* at varying conditions. DIC image of 32 µM IM30wt (A, C) or IM30* (B, D) in phase separation buffer at 3 M urea without (A, B) or with (C, D) additional 10% PEG, 100 mM NaCl and pH change to pH 5.5. (E) Column diagram showing 32 µM IM30 (purple) or IM30* (grey) comparing both proteins at each condition. Experiments were performed in phase separation buffer and additional changes to the buffer such as 3M instead of 0 M urea, pH 5.5 instead of pH 7.5, 100 mM instead of 0 mM NaCl and 10% instead of 0% PEG are marked in the table below the images with a "+". The samples were analyzed via DIC microscopy at each specified condition to distinguish between formation of aggregates and condensates and can be seen in* ***Supplementary figure 8.2-8****,* ***Supplementary figure 8.2-9****,* ***Supplementary figure 8.2-10****, and* ***Supplementary figure 8.2-11****. Columns with diagonal stripes indicate the formation of large aggregates or small undefined particles, in contrast to the formation of condensates. Differences in mean values between samples are indicated as lines that end above the respective columns with an asterisk indicating significant differences and n.s. for no*

significant difference according to Welch's t-test ($p<0.05$). Representative images and error bars representing standard deviations were taken from n=3 biological replicates.

Furthermore, we observed a significant difference in the stability against urea between condensates formed by IM30* and aggregates formed by IM30. These differences occurred for both pH-induced condensates and aggregates in absence of salt, as well as for PEG/NaCl-induced condensates and aggregates (**Figure 3.2-9**E). While pH- and PEG-NaCl-induced IM30* condensates were dissolved by 3 M urea, IM30 aggregates that formed at the same conditions were still present at 3 M urea (**Figure 3.2-9**E).

Both PEG and NaCl changed IM30 assemblies that formed at pH 5.5 in presence of urea. Notably, the addition of PEG resulted in the formation of condensates for both IM30 and IM30*. Interestingly, the addition of NaCl on the other hand simply prevented aggregation of IM30. It seems that pH-induced aggregates of IM30 form due to attractive intermolecular electrostatic interactions that are maximized near the proteins pI, where the proteins net charge is zero (**Figure 3.2-9**E). Formation of pH-induced aggregates might be prevented by the reduction of electrostatic interactions due to screening of charges and simultaneous destabilizing effect of urea on hydrogen bonds. In summary, by systematically screening the parameters that were found to be promoting condensate formation in IM30*, we were able to show the effect of salt, crowding environment and differences in pH for the formation of molecular assemblies by IM30.

It is possible that there still were small amounts of transiently formed higher oligomers present in 3 M urea, which could have aggregated as opposed to IM30*, which has no tendency to form aggregation-prone higher oligomers. Additionally, the change in pH, as well as the presence of 100 mM NaCl and 10% PEG, might affect the oligomer stability against urea denaturation and shift the equilibrium ratio of intact to disassembled IM30 oligomers.

Combined, these results indicate that the formation of IM30 condensates depends on the combination of multiple factors, including molecular crowding, pH, the salt concentration and IM30's oligomeric state.

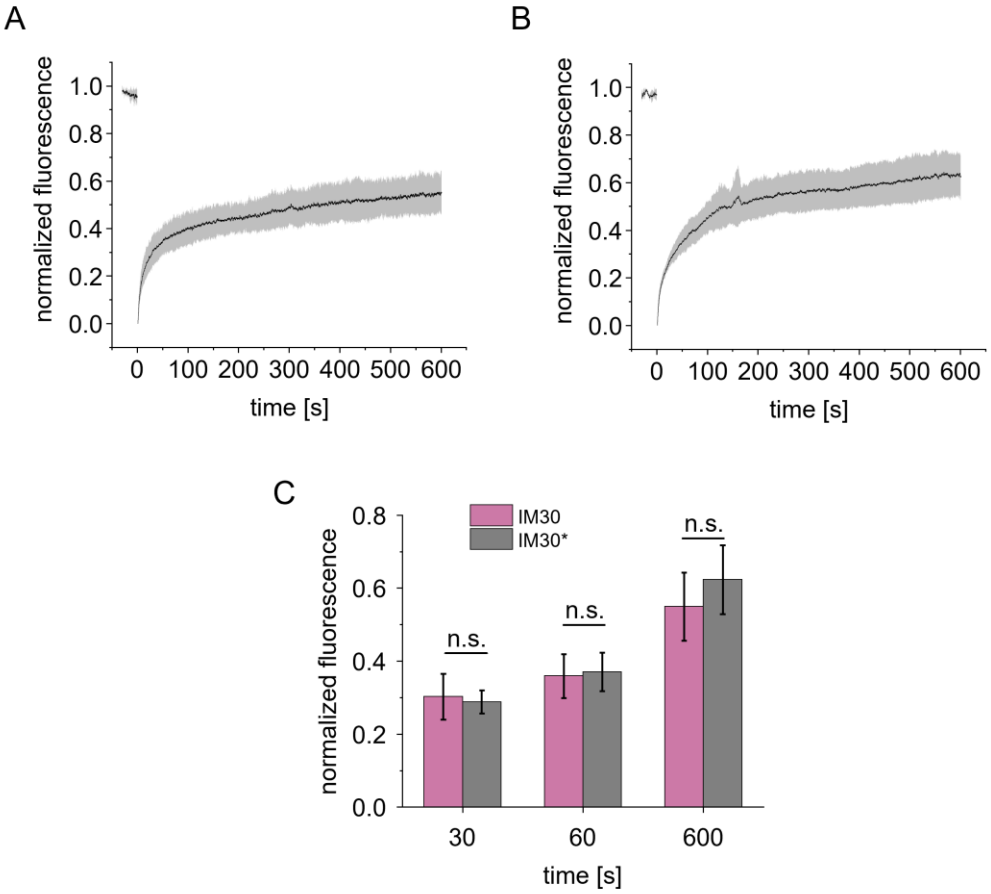

Figure 3.2-10: *Comparison between FRAP experiments on IM30 and IM30* condensates. FRAP of IM30 wt (A) and IM30* (B) condensates formed at pH 5.5, 10% PEG, 100 mM NaCl, 3 M urea. (C) Comparison of FRAP levels at different time points during recovery for IM30wt (purple) and IM30* (black). According to Welch's t-test ($p<0.05$) all differences are not significant (n.s.). Grey area (A+B) and error bars (C) represent standard deviations taken from n=3 biological replicates (N=4 condensates).*

We used IM30* as a model to study IM30 condensate formation in absence of urea (**Figure 3.2-4**, **Figure 3.2-5**) and showed that both proteins have the same requirements for condensate formation in presence of urea (**Figure 3.2-9**E). Hence, to find out if both proteins share similar liquid-like states we next analyzed condensates of each individual protein via monitoring FRAP at otherwise identical conditions. The measured recovery is similar for both proteins with approximately 60% recovery after 10 minutes (**Figure 3.2-10**A, B) and no significant differences in recovery after 30 s, 1 min, and 10 min (**Figure 3.2-10**C) were observed, in line with our assumption that IM30wt and IM30* form condensates with similar fluidity. Their recovery is about equal to the recovery

determined in absence of urea for PEG/NaCl-induced IM30* condensates (**Figure 3.2-7**), but lower when compared to FRAP for pH-induced condensates of IM30* in absence of urea (**Figure 3.2-6**). Thus, there appears to be a considerable immobile fraction inside these condensates.

Taken together our data clearly show that oligomer disassembly enables condensate formation of IM30 and that IM30* is a valid model to study IM30 condensate formation in greater detail.

3.2.3. Discussion

3.2.3.1. IM30 forms condensates in vitro at physiologically relevant conditions

The pH within the cytoplasm and inside the thylakoid lumen of the marine cyanobacterium *Agmenellum quadruplicatum* were estimated to be around 7.3 and 5.6, respectively, when the cells were grown at neutral pH[181]. IM30 is localized in the cyanobacterial cytoplasm or the chloroplast stroma, where it is either soluble or attached to internal membranes[90,107,112,139]. As the cytoplasmic pH is > 7 in living cells, under physiological conditions IM30 is exposed to a pH that is higher than the pH range determined in this study required for condensate formation (< 6.5, **Figure 3.2-4**). However, due to proton accumulation at the surface of negatively charged membranes, the pH can be significantly lowered near the TM, up to 3 pH units[205]. IM30 is known to bind to negatively charged membranes[55] and structural rearrangements are triggered by lowering the pH value[135]. Based on this, IM30 has been suggested to be involved in membrane sealing and/or repair, by a yet undefined mechanism[104,135,206]. Due to the photosynthetic light reaction, a ΔpH is established across the thylakoid membrane[181,207], and TM damage involves proton leakage out of the TM lumen into the cytosol. Thus, at damaged membrane sites the local proton concentration is increased, *i.e.* the local pH is lowered which could well trigger the IM30 activity.

At a pH value close to a proteins isoelectric point (pI), the solubility of a protein is typically decreased, and condensate formation can be promoted[180]. Stressed membranes are susceptible to proton leakage and IM30 has been observed to form *punctae* at higher frequency under conditions where cells are stressed[107,112]. At places where the regular TM structure is damaged, the pH value of the cytoplasm is locally decreased due to protons leaking out of the TM lumen into the cytoplasm. Thus, the pH of 5.5-6, determined to trigger phase separation, is in a physiologically

relevant range and perfectly in line with the earlier proposed membrane protective function of IM30 *in vivo*.

Yet, the IM30wt protein appears to cluster and forms large aggregates at pH 5.5 instead of forming liquid-like condensates, which at first view could contradict the hypothesis of an effect of pH on condensate formation. However, as the IM30* variant that is impaired in barrel formation readily forms condensates, we assume that the differences in the observed pH response are related to the oligomeric state of IM30. Thus, disassembly of IM30wt oligomers in a cellular environment, *e.g.* mediated by chaperones, could well enable the formation of IM30wt condensates (as further discussed below).

Apart from barrel disassembly and environmental factors a protein concentration above the critical saturation concentration, c_{sat}, is required for condensate formation. Our phase diagrams indicate a c_{sat} of ~4 µM at pH 5.5 (**Figure 3.2-4**F). Of course, the value of c_{sat} is modulated *in vitro* as well as *in vivo* by a multitude of additional factors such as temperature, ionic strength, post-translational modifications, and many others, but as we also determined a similar c_{sat} for PEG/NaCl-induced condensates (**Figure 3.2-5**E) we will use this value as a reference point. A study investigating the *in vivo* abundance of several proteins in *Synechocystis* PCC 6803 identified IM30 to be present at 40500-45000 copies per cell (cpc)[208]. When assuming an average diameter of a cyanobacterial cell between 1-2 µm and approximating its shape to a sphere, the IM30 concentration inside a single *Synechocystis* cell is 128-143 µM for d=1 µm and 16-18 µM for d=2 µm. In fact the concentration estimated here is a lower limit since part of the cell volume is occupied by the thylakoid membrane system.

The estimated *in vivo* concentration is even higher than the saturation concentration for IM30* of about 4 µM determined here in the *in vitro* analyses (**Figure 3.2-4**F, **Figure 3.2-5**E), and fits perfectly to the physiologically relevant range for the proposed formation of IM30 condensates *in vivo*.

3.2.3.2. Morphology of IM30 in vivo punctae resembles in vitro condensates

Various studies have reported the formation of IM30 *punctae* in living cyanobacterial cells under stress conditions [94,107,108,209]. It has been speculated that these *punctae* represent clustered or

aggregated IM30 oligomers[107,108,112]. Yet, as the oligomerization-deficient variant IM30* still forms *punctae* structures *in vivo* (Figure 1.2-1B), barrel formation clearly is not required for formation of these structures, and thus the *punctae* do not merely represent clustered IM30 homo-oligomers. Alternatively, as these *punctae* are typically localized in close proximity to internal membranes, especially TMs, these structures could be similar to membrane-covering carpet structures IM30 formed on solid supported bilayers[104]. Furthermore, while located near internal membranes, the globular, round shape of these *punctae* (Figure 3.2-2) contradicts the concept that these structures represent membrane carpets, rather suggests that IM30 *punctae* might be liquid condensates that form upon barrel disassembly.

In *Arabidopsis thaliana*, IM30 appears to form more diverse structures, such as forked and web-like assemblies[209], besides the *punctae* structures described previously as well as in this study. Condensates formed by IM30 in vitro did not show such irregular shapes and were mostly spherical (**Figure *3.2-1***). In line with this, we observed mostly spherical *punctae* structures in *Synechocystis* cells when we analyzed the IM30 wt protein, with occasional small patches near membrane surfaces (**Supplementary figure 8.2-5**). Yet, an additional distinct fluorescence signal that preferentially localized at the cytoplasmic membrane and had covered large flat areas was observed with IM30* (**Figure *3.2-1***), and these signals could well represent membrane surface-covering carpets. Likely, similar structures also form with the IM30wt protein, yet to a lesser extent and thus, IM30 displays a remarkable structural plasticity *in vivo*, involving (at least) the formation of barrels (and rods), partly unfolded monomers, membrane carpets as well as condensates.

3.2.3.3. IM30 condensate formation in the context of the ESCRT-III superfamily

The IM30 protein belongs to the ESCRT-III protein family, all members of which form large oligomeric assemblies that are involved in membrane remodeling[99]. For eukaryotic ESCRT-III complexes, a crucial part of their ability to reshape membranes has been suggested to involve sequential exchange of monomers incorporated into large oligomeric rods via unfolding of individual protomers by the AAA+ ATPase VPS4[144–147,210]. Orchestrated disassembly has been suggested to be enabled by interactions of the N-terminal microtubule interacting and transport (MIT) domain of VPS4 with different MIT interacting motifs (MIM) of ESCRT-III proteins[144,211–213]. MIT domains are represented by a three-helix bundle that was shown to bind to an

amphipathic-helix type MIM with its helices 2 and 3[214]. The interactions between these MIT and MIM domains results in recruitment of VPS4 for ESCRT-III polymer remodeling in eukaryotes[213]. The reported consensus sequence of the C-terminal amphipathic-helix type MIM (D/E)xxLxxRLxxL(K/R)[214] and the reported consensus sequence of the C-terminal helix 6 of IM30 (SVVDAELEELRRKLDKL)[127] show a similar pattern of charged and hydrophobic amino acid residues as seen in their helical wheel projections (https://www.bioinformatics.nl/cgi-bin/emboss/pepwheel) (suppl. fig. 3) . Furthermore, MIM binding to the MIT domain does not only recruit but also activate VPS4 mediated disassembly of ECRT-III polymers by releasing the auto-inhibitory interaction of VPS4 with its MIT domain[212]. Interestingly, the recruitment and activity of ClpB, another AAA+ ATPase involved in disaggregation, is regulated by binding of its coiled-coil M domain to DnaK[215–217]. As opposed to ATP-dependent disassembly by VPS4, eukaryotic ESCRT-III proteins seem to assemble spontaneously by themselves. Similarly, IM30 assembles spontaneously and nucleotide binding to IM30[96] and/or nucleotide hydrolysis appear not to be required for IM30 homo-oligomerization [138,218,219], which strongly indicates a prevalence of IM30 oligomers *in vivo*. In fact, IM30 oligomers have been visualized *in vivo*, in living cells[96]. While eukaryotic ESCRT-III as well as several bacterial PspA appear to be disassembled by the activity of a AAA+ ATPase, a VPS4 homolog appears not to be encoded in *Synechocystis* and another AAA+ ATPase is not encoded in the proximity of the *im30* gene[16,220]. Furthermore, there are no MIT containing proteins in *Synechocystis* according to an HMMer search against the MIT domain of VPS4 from *Arabidopsis thaliana* (https://www.ebi.ac.uk/Tools/hmmer/search/phmmer). Despite the lack of putative IM30 MIM interaction partners containing MIT domains, the C-terminal helix 6 in IM30 could be involved in stimulating protomer extraction during potential polymer remodeling and guide regulated IM30 oligomer disassembly by other disaggregating AAA+ ATPases, like ClpB. The ClpB/HSP100 protein works together with DnaK/HSP70 in the disassembly of aggregates, of *e. g.* heat-damaged proteins[215,221–223] and members of the HSP70/DnaK family have been identified to interact with the C-terminal region of IM30 and disassembles IM30 assemblies *in vivo* as well as *in vitro*[130,143,224].

Taking a step back from ESCRT-III related AAA+ disaggregases, there have been reports on a Type-VI secretion system in bacteria that uses the AAA+ ATPase ClpV to disassemble helical rod-like structures[225]. It was shown that ClpV interacts with an exposed amphipathic helix of VipB, which bound to the N-domain of ClpV via a hydrophobic groove [226]. Many MIM motives are

amphipathic helices that interact with the MIT domain of VPS4 via hydrophobic interactions inside a groove[213]. The ClpV ATPase with its N-domain also contains an M-domain and has the same domain structure as ClpB[227]. Therefore, the C-terminal amphipathic helix α6 of IM30 might enable targeting of ClpB of *Synechocystis* to IM30. Thus, further studies on ESCRT-III-disassembly in bacteria could reveal ClpB as the missing ATPase in homology to eucaryotic VPS4.

Taken together, there are multiple parallels that could be drawn to eukaryotic interaction partners of ESCRT-III proteins which could play a similar role for IM30. There is much to be learned from its interaction with DnaK, potential involvement of AAA+ disaggregases like ClpB, and IM30s putative C-terminal amphipathic helix, which could be mediating specialized protein interactions with the N-domain of ClpB compared to its predecessor PspA, which is lacking this extension. Therefore, it is well possible that IM30 monomers, oligomers and condensates coexist and are of relevance *in vivo*, and their respective concentrations are regulated by proteins such as DnaK.

Another bacterial member of the ESCRT-III protein family, PspA, was already shown to interact with the ATPase PspF[124,163,171]. However, these interactions were not reported in the context of oligomer disassembly, but in the inhibition of the ATPase-mediated activation of gene expression[124,163].

3.2.3.4. Implications of condensate formation for IM30 in vivo function

Biomolecular condensates often form in response to various stress conditions[228–230] and can aid in the protection of the cell[182,231]. Studies have shown that biomolecular condensates can exert forces on the lipids membranes, that can result in membrane remodeling and reshaping[65,232–234]. Another study even reported on biomolecular condensates that formed at sites of membrane damage to aid stabilize the membrane and facilitate the repair process[235]. IM30 is known to form *punctae in vivo* with higher frequency in response to environmental stress[101,107,112,131,168] and a recent study suggested that IM30 rapidly localize to sites of photoinduced membrane damage with localization dynamics that are similar to Ostwald ripening[108]. Eucaryotic ESCRT-III participates in the repair of small ruptures in endolysosomal membranes[236,237] and the ESCRT-III members CHMP2A and CHMP4B, as well as the ESCRT-III binding protein ALIX were recently shown to being rapidly recruited to damaged lysosomes together with stress granules[235]. The membrane repair by stress granules was reported to involve rapid plugging, wetting, and stabilization of the pore to prevent further leakage[235].

Apart from passive response to cellular changes, such as temperature, salt concentration, and pH, biomolecular condensates can be actively modulated by cells through the introduction of post-translational modifications affecting inter- and intramolecular protein-protein interactions, as well as control over expression levels of condensate forming components[58,238,239]. For example, phosphorylation was shown to modulate condensate formation of ALIX and thereby regulate the activation of CHMP4[240]. Interestingly, IM30 is reversibly phosphorylated during the phases of nitrogen chlorosis in relation to the biogenesis of new thylakoid membranes[241,242]. Therefore, IM30 phosphorylation could directly influence its self-assembly into condensates, recruitment of other proteins into IM30 condensates and other protein-protein interactions with potential interaction partners, leading to depletion or increase of IM30 available for condensate formation.

This could indicate a possible mechanism involving both initial plugging of damaged membranes by IM30 condensates followed by subsequent formation of other assemblies like IM30 carpet like structures and barrels for membrane repair.

3.3 Coiled-coil interactions drive IM30 condensate formation

3.3.1. Introduction

The *inner membrane associated protein of 30 kDa* (IM30), also known as Vipp1 (the *vesicle-inducing protein in plastids 1*), is crucially involved in the biogenesis and maintenance of thylakoid membranes (TM) in cyanobacteria and chloroplasts[90,91,95]. Our group and others have shown that IM30 and PspA belong to the same membrane remodeling superfamily of endosome complex for recruitment and transport III (ESCRT-III) proteins that previously solely referred to proteins from eukaryotes and archaea[96–99].

Across cyanobacteria as well as chloroplasts from plants and green algae the IM30 protein is reported to accumulate into distinct areas of high fluorescence intensity called punctae *in vivo*[93,94,112] and sophisticated studies have given insight into the dynamics, triggers, and localization of punctae *in vivo*[93,107,108,112,168]. Nevertheless, the exact function of IM30 *punctae* is still enigmatic and the underlying structure of these assemblies is still not known. Recently, we were able to point out that IM30 can form condensates upon barrel disassembly and showed that the IM30* variant which is deficient in barrel formation and contains an extended intrinsically disordered region (IDR) was still able to form punctae *in vivo*. Furthermore, we showed that IM30 forms these condensates at physiological relevant conditions. Another study independently reported dynamical growth and shrinking of *punctae* in temporal relation to each other that resembled Ostwald ripening, which is one of the possible types of condensate growth[108].

Both IM30 and IM30* were able to form puncta *in vivo* and condensates *in vitro* (section 3.2) as well as carpet-like structures *in vitro*[104], but the regions that are enabling IM30 to form these different assemblies and their relation to punctae are not known so far. To provide further insight into the nature of puncta formation we investigate the ability of truncated IM30 variants (**Figure 3.3-1**) to form supramolecular assemblies *in vitro* and *in vivo*.

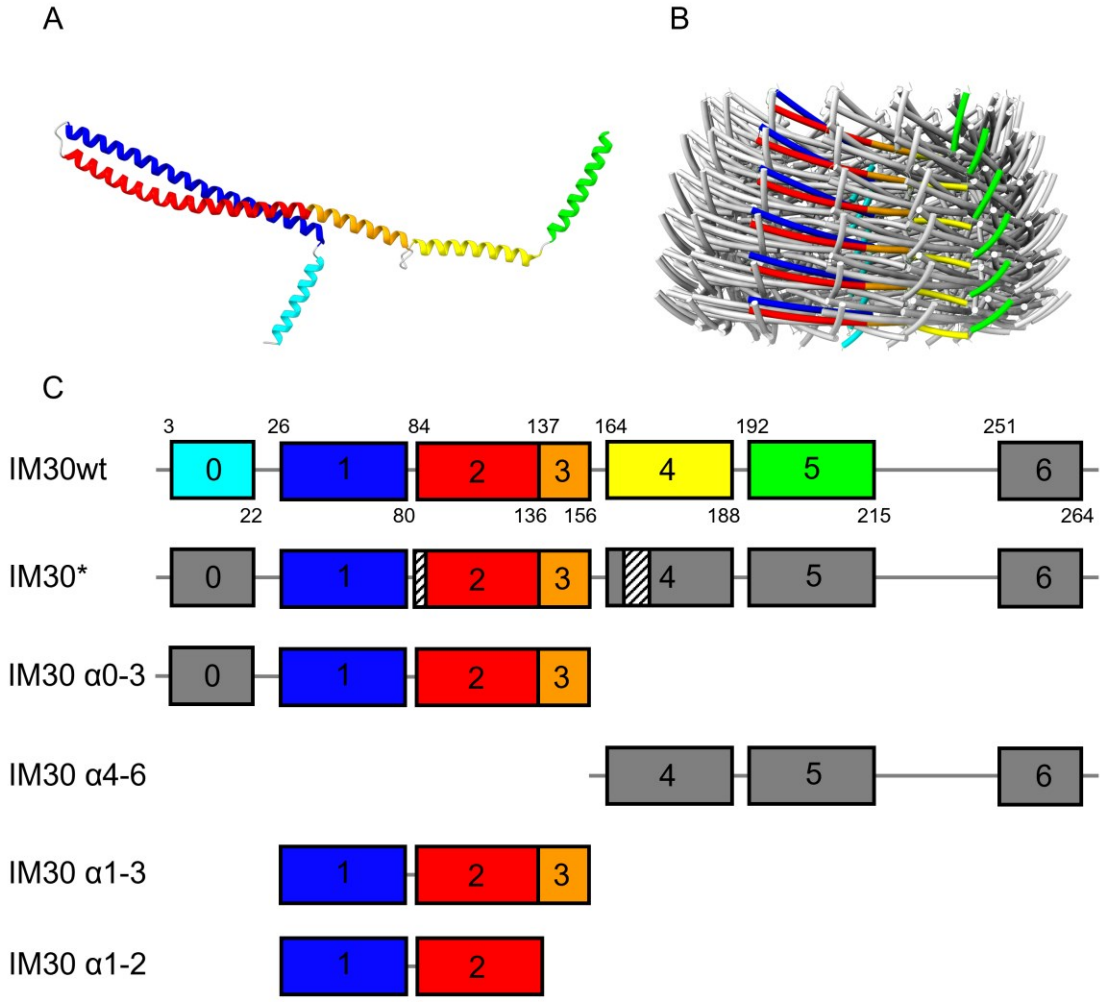

***Figure 3.3-1**: IM30 structure and schematic representations of truncated IM30 variants (adapted from **Figure 1.2-1** and **Figure 3.1-1**). (A) Structure of an IM30 monomer without the C-terminal flexible region containing helix 6 (PDB: 7O3Y). (B) Model of IM30 barrel in cylinder cartoon representation in grey with helices from a single monomer in each layer colored as in (A) for IM30wt (PDB:7O3Y). (C) Schematic representation of full-length and truncated IM30 variants analyzed in this study. Numbers inside the boxes represent numbers of helices, and colors in boxes correspond to colors of helices in the model. Grey color indicates flexible and disordered regions. Small numbers above and below boxes represent beginning and end of regions defined in this study as helix. The position of mutated amino acids in IM30* are indicated by white boxes with black stripes.*

3.3.2. Results

3.3.2.1. IM30 puncta formation does not depend on the extended C-terminal IDR in vivo

IM30 is known to frequently form punctae *in vivo*[94,107,108,112] that were discussed in the context of the formation of higher oligomeric structures, like rod-like structures, scaffolds, or clusters of multiple barrels, but the exact type of supramolecular assembly is still under debate[136,243]. Furthermore, the exact function of punctae is still not known, but studies have shown that *punctae* formation is increased under high-light compared to low-light growth conditions[112]. Additionally, the dynamic re-localization seemed to be important for the acquisition of photosynthetic competency[107] and IM30 accumulated into *punctae* in response to high light induced chlorophyl a damage in the thylakoid membrane[108]. In our studies we showed that the IM30* mutant which does not form barrel structures anymore was still able to accumulate into *punctae in vivo* and hypothesized that IM30 *punctae* could be related to condensate formation (section 3.1).

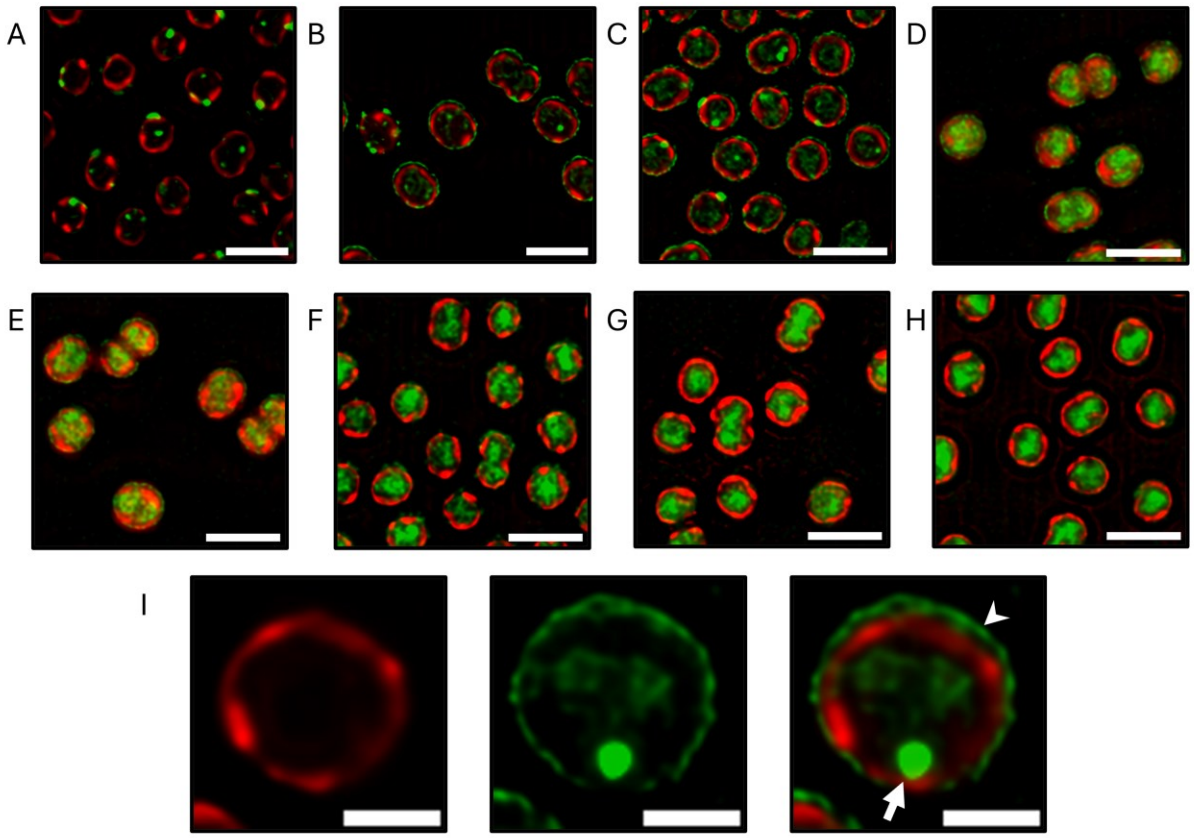

***Figure 3.3-2**: SIM² fluorescence images showing the localization of different IM30 variants in Synechocystis. (A) IM30-7GS-mVenus, (B) IM30*-7GS-mVenus, (C) IM30$_{1-156}$-7GS-mVenus, (D) IM30$_{26-156}$-7GS-mVenus, (E) IM30$_{26-136}$-7GS-mVenus, (F) IM30$_{157-267}$-7GS-mVenus, (G) mVenus, (H) 7GS-mVenus. (I) fluorescence images of TM channel (left), mVenus channel (middle) and combined channels (right) for a single Synechocystis cell expressing IM30$_{1-156}$-7GS-mVenus. A single punctum is indicated by*

a white arrow and a sheet-like structure near the plasma membrane is indicated by a white arrowhead. Scale bars represent 3 µm in (A-G) and 1 µm in (I). All original images were acquired and processed to obtain SIM² images by [redacted] *in the lab of* [redacted] *(University of Liverpool).*

To test if the ability to form condensates *in vitro* shows further parallels to IM30 puncta formation, we generated *Synechocystis* cells expressing truncated IM30 variants fused to a yellow fluorescent protein (mVenus) to compare the localization of full-length IM30 and truncated IM30 variants *in vivo*. The genes were inserted in addition to the native *im30* gene in the cells to prevent loss of viability due the lack of the essential native *im30* gene. The fluorescence signal of IM30-mVenus frequently accumulated into prototypical punctae both near the thylakoid membrane and in the cytosol (**Figure 3.3-2**A, as previously described in section 3.2.2.1). The mutant deficient in barrel formation IM30*-mVenus is equally capable of forming *punctae* and shows an additional fluorescence signal at the plasma membrane (**Figure 3.3-2**B, as previously described in section 3.2.2.1). Interestingly, even for the truncated variant $IM30_{1\text{-}156}$-mVenus we observed puncta formation as well as localization at the plasma membrane (**Figure 3.3-2**C, I) like IM30*-mVenus. The fluorescence signal of mVenus fused to $IM30_{157\text{-}267}$, $IM30_{26\text{-}156}$ and $IM30_{26\text{-}136}$ was distributed in the cytosol (**Figure 3.3-2**D, E, F), but an additional localization at the plasma membrane was observed for mVenus fused to $IM30_{26\text{-}156}$ and $IM30_{26\text{-}136}$ (**Figure 3.3-2**D, E) as seen for IM30*-mVenus and $IM30_{1\text{-}156}$-mVenus (**Figure 3.3-2**B, C, I).

3.3.2.2. IM30's N-terminal coiled-coil domain drives condensate formation

Both IM30wt and IM30* can form liquid condensates but it remained unknown which part of the protein is driving condensate formation (section 3.2). IM30wt is only able to form condensates after barrel disassembly (section 3.2). Chaperones such as HSP70/DnaK were shown to interact with IM30 and promote oligomer disassembly in *Chlamydomonas reinhardtii*[130,224]. We previously showed that upon barrel disassembly large regions of the protein apart from the central coiled-coil become disordered (section 3.1). In this process, the C-terminal part containing the regions of helices α4-6 turned into an extended IDR and IM30 obtained a conformation similar to IM30* (Junglas et al. 2020 and section 3.1). IDRs are frequently involved in driving phase separation and possess an inherent flexibility facilitating them to partake in multiple transient interactions[58,60,89]. To see if the extended IDR or other parts of IM30* enable it to form condensates, we performed turbidity measurements followed by DIC microscopy with IM30* and truncated

IM30 variants at conditions that favored condensate formation of IM30*, i.e. at 100 mM NaCl and 10% PEG (**Figure 3.3-3**).

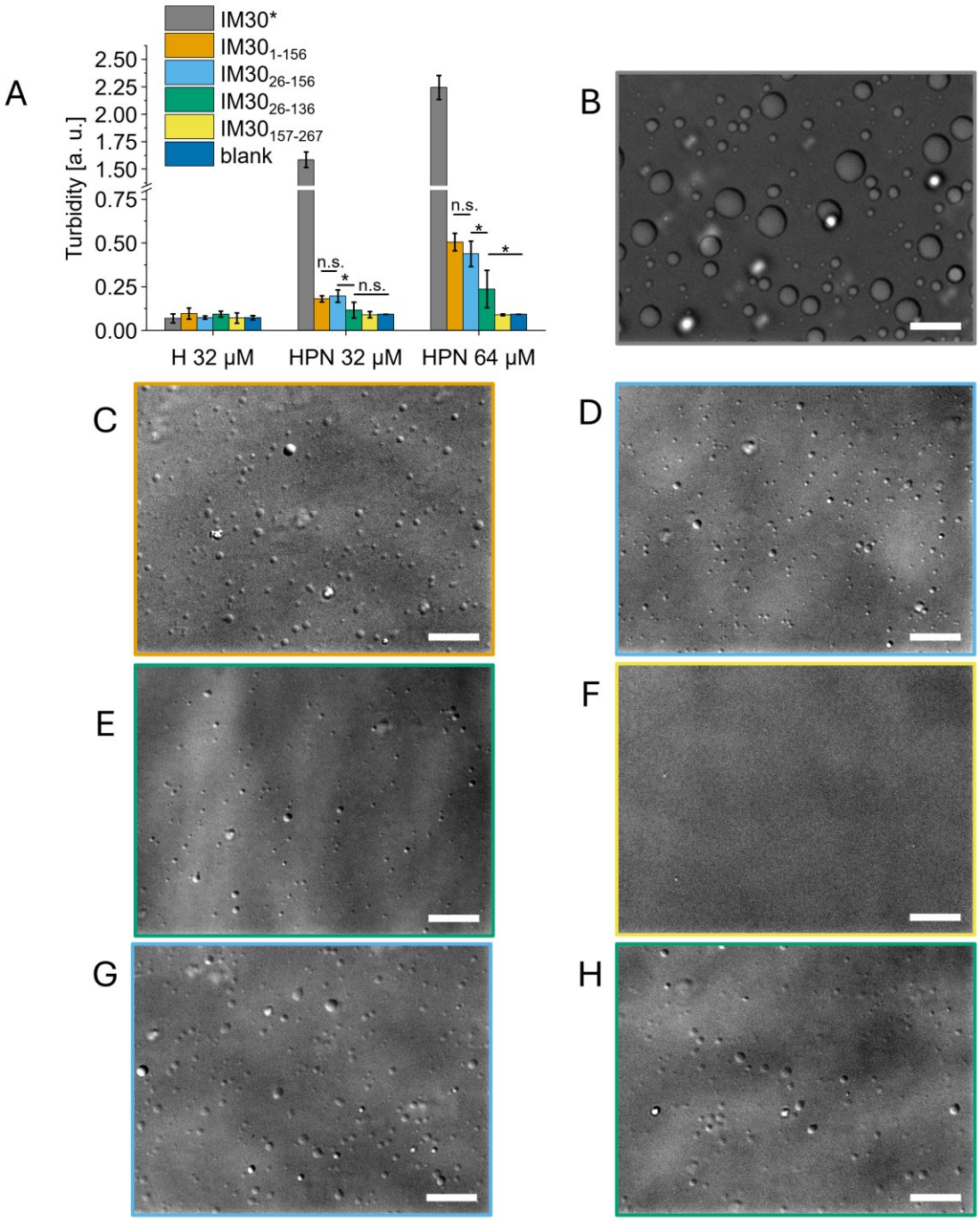

***Figure 3.3-3**: Turbidity measurements and DIC microscopy images of IM30 variants at condensate promoting conditions. (A) Turbidity for IM30* (grey), IM30$_{1-156}$ (orange), IM30$_{26-156}$ (light blue), IM30$_{26-136}$ (green), IM30$_{157-267}$ (yellow), or blank (dark blue) samples at different conditions indicated below the grouped columns as 20 mM HEPES - H, 10% PEG - P and 100 mM NaCl –*

N; (B-F) DIC microscopy images corresponding to 32 µM protein at 20 mM HEPES, 10% PEG, 100 mM NaCl for (B) IM30, (C) $IM30_{1-156}$, (D) $IM30_{26-156}$, (E) $IM30_{26-136}$ or (F) $IM30_{157-267}$ with frames sharing the same color as in (A); (G, H) DIC microscopy images corresponding to 64 µM protein at 20 mM HEPES, 10% PEG, 100 mM NaCl for $IM30_{26-156}$ (G) or $IM30_{26-136}$ (H) with frames sharing the same color as in (A). Scale bars are 10 µm. Representative DIC images are shown, and error bars indicate standard deviations from n = 3 experiments.*

Our data show that all variants containing the minimal coiled-coil region ($IM30_{26-136}$) α1-2 can form condensates (**Figure 3.3-3**A-E, G, H). Surprisingly, the extended IDR $IM30_{157-267}$ (α4-6) did not form condensates under any of the tested conditions (**Figure 3.3-3**A, F). Droplet sizes in DIC images and turbidity values of the truncated variants were drastically decreased compared to IM30* at equal concentrations (**Figure 3.3-3**A-E). The turbidity of $IM30_{26-136}$ (α1-2) was not significantly different from the blank in the PEG-NaCl sample at 32 µM (**Figure 3.3-3**A). Nevertheless, we already detected some condensates at 32 µM for this condition by DIC microscopy, which were further increased in size at 64 µM and showed significantly higher turbidity compared to the blank but still lower turbidity and fewer condensates compared to $IM30_{26-156}$ (α1-3) (**Figure 3.3-3**E, G, H). While we measured significantly higher turbidity for $IM30_{26-136}$ condensates compared to $IM30_{26-156}$ condensates at both 32 µM and 64 µM in the PEG-NaCl samples, we detected no significant differences between $IM30_{26-156}$ and $IM30_{1-156}$ (α0-3) at these conditions (**Figure 3.3-3**A).

Taken together, our data suggests that the presence of additional helices a0 and a3 increases condensate formation propensity, whereas the extended IDR alone does not form condensates but further enhances condensate formation of IM30* compared to the truncated variants.

3.3.2.3. The extended IDR in IM30* auto-inhibits condensate formation

Based on the recently reported data including a phase diagram, IM30* requires both PEG and NaCl for condensate formation at pH 7.6 (see section 3.2). Additional experiments showed that the same conditions that were promoting IM30* condensate formation also led to condensate or aggregate formation of IM30 depending on the oligomeric state of the protein (see section 3.2). To test if truncated IM30 variants share similar condensate forming conditions with IM30* we tested the requirements for the simultaneous presence of PEG and NaCl for condensate formation (**Figure 3.3-4**). All IM30 variants did not form condensates when only 100 mM NaCl was present (**Figure 3.3-4**A). Surprisingly, all tested IM30 variants that did form PEG-NaCl induced condensates, *i.e.*

all but IM30$_{157-267}$, also formed PEG-induced condensates in absence of additional NaCl, except for IM30* (**Figure 3.3-4**A-F).

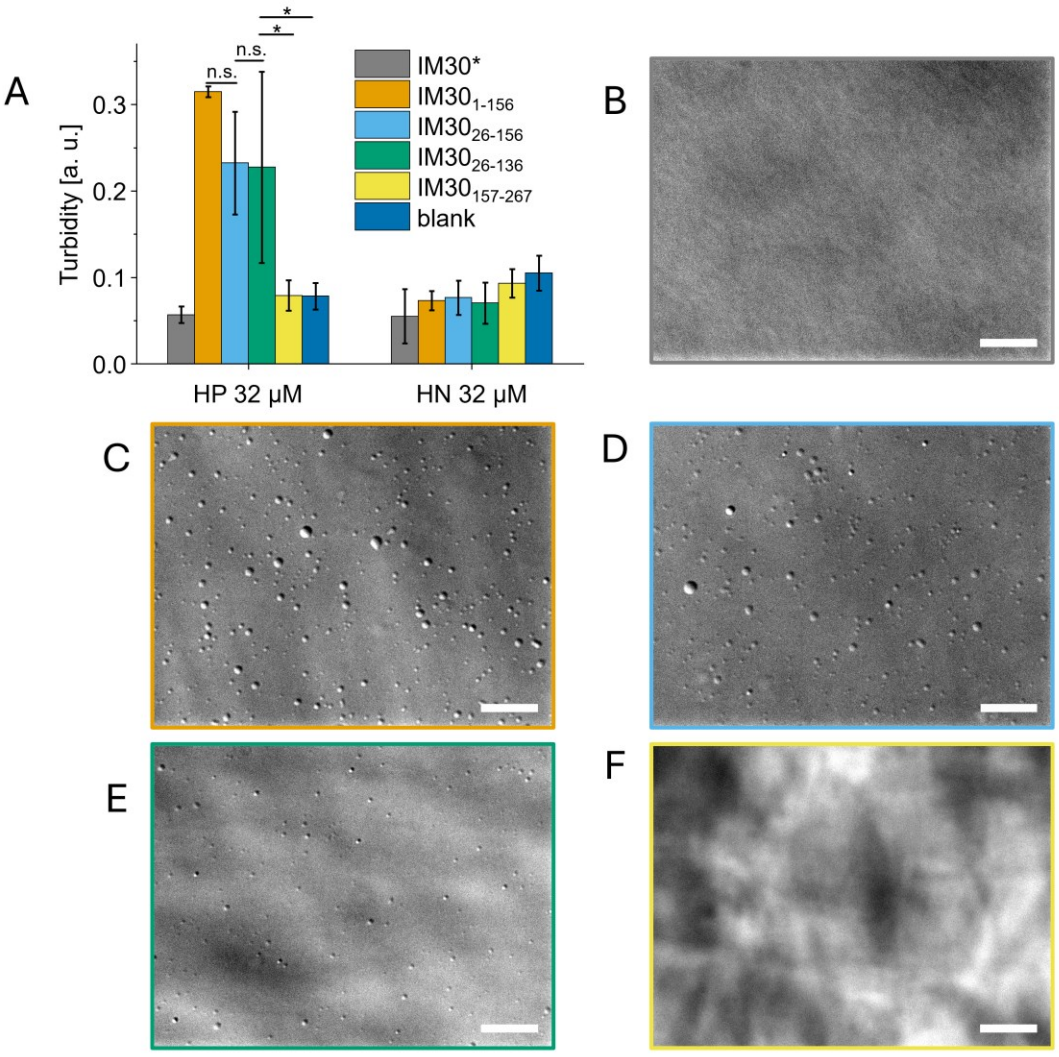

***Figure 3.3-4**: Turbidity measurements and DIC microscopy images of IM30 variants showing the effect of PEG and NaCl. (A) Measured turbidity of IM30* (grey), IM30$_{1-156}$ (orange), IM30$_{26-156}$ (light blue), IM30$_{26-136}$ (green), IM30$_{157-267}$ (yellow), or blank (dark blue) samples at 20 mM HEPES – H and 10% PEG - P (left group) or 100 mM NaCl – N (right group); (B-F) DIC microscopy images corresponding to 32 µM protein at 20 mM HEPES, 10% PEG for (B) IM30*, (C) IM30$_{1-156}$, (D) IM30$_{26-156}$, (E) IM30$_{26-136}$ or (F) IM30$_{157-267}$ with frames sharing the same color as in (A). Scale bars are 10 µm. Representative DIC images are shown, and error bars indicate standard deviations from n = 3 experiments.*

3.3.2.4. Destabilization of the coiled-coil by urea disrupts condensate formation

Due to the inability of the extended IDR IM30$_{157\text{-}267}$ (α4-6) to form condensates in contrast to all variants containing the coiled-coil region, we hypothesized that transient intermolecular interactions between the isolated coiled-coils might be the driving force for condensate formation of IM30. It has been reported that coiled-coil interactions, meaning associative interactions between helices that are connected by short linkers, are capable of driving condensate formation[244]. To test if coiled-coil interactions are needed for condensate formation, we utilized urea to destabilize the remaining secondary structure of the coiled-coil in IM30* and followed PEG/NaCl- and pH-induced IM30* condensate formation at different urea concentrations.

We observed a steady decrease in turbidity for PEG/NaCl-induced condensates with increasing urea concentrations up to 3 M urea (**Figure 3.3-5**A). Above 3 M urea the turbidity stayed at a constant low level. Similarly, the turbidity of IM30* at pH 5.5 in absence of PEG and NaCl decreased drastically in presence of 3 M urea (**Figure 3.3-5**C). To verify that the reduction in turbidity was due to fewer condensates, we performed DIC microscopy at increasing urea concentrations. Here, we did observe a similar effect of urea on condensate formation as condensates seemed to decrease in size and number with increasing urea concentration for PEG-NaCl induced condensates (**Figure 3.3-5**F) and no condensate could be observed at urea concentration of ≥ 3 M for both PEG-NaCl and pH 5.5 conditions (**Figure 3.3-5**D, E, F) in total agreement with the turbidity measurements (**Figure 3.3-5**A, C).

Hexane-diol is another destabilizing agent used to disrupt hydrophobic interactions and interactions involving aromatic residues[179,184,245]. To analyze the importance of these interactions at high ionic strength, where electrostatic contributions should be negligible, we followed condensate formation of IM30* at 1000 mM NaCl and increasing hexane-diol concentration using turbidity measurements and DIC microscopy. In contrast to the dissolving effect of urea (**Figure 3.3-5**A, C-F), we observed no decline in turbidity for increasing concentrations of hexane-diol (**Figure 3.3-5**B), which was validated by condensate formation still being observed at 10% hexane-diol via DIC microcopy (**Figure 3.3-5**G). The only observable change in DIC images was an apparent decrease in condensate size which seemed to be accompanied by a simultaneous increase in number of condensates (**Figure 3.3-5**G) resulting in an overall constant turbidity signal (**Figure 3.3-5**B).

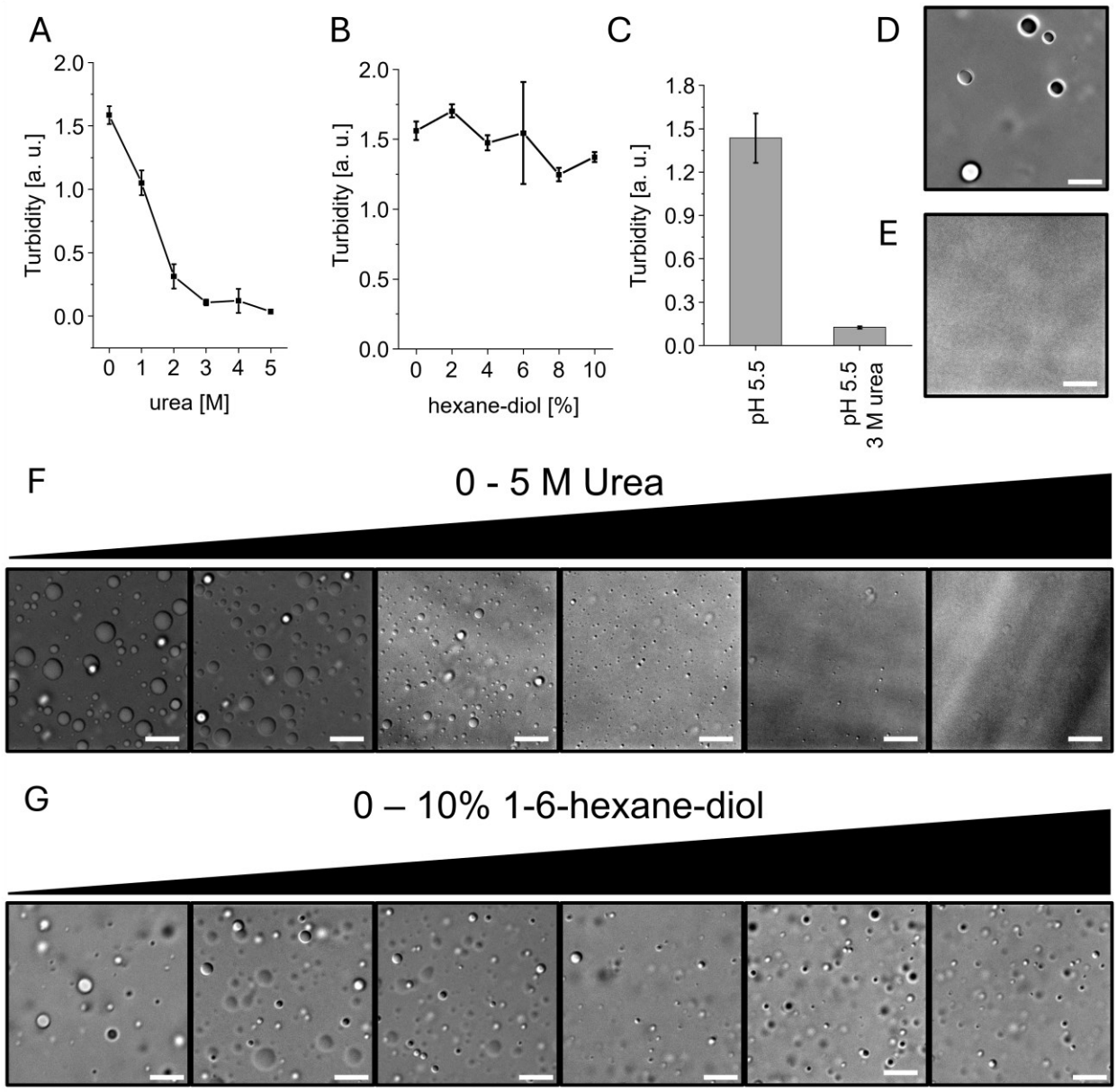

Figure 3.3-5*: Turbidity measurements and DIC microscopy images of IM30* condensates in presence and absence of destabilizing agents. (A) Measured turbidity of PEG-NaCl induced IM30* condensates at 32 µM protein concentration, 20 mM HEPES, 10% PEG, 100 mM NaCl at increasing urea concentrations; (C) Measured turbidity and corresponding DIC images (D,E) for pH induced IM30* condensates at 32 µM protein concentration, 10 mM HEPES, 10 mM phosphate buffer at pH 5.5 in absence (D) and in presence (E) of 3 M urea; (F) DIC microscopy images of PEG-NaCl induced IM30* condensates at 32 µM protein concentration, 20 mM HEPES, 10% PEG, 100 mM NaCl at increasing urea concentrations from 0 M urea (left) to 5 M urea (right) in 1 M steps; (G) DIC microscopy images of PEG-NaCl induced IM30* condensates at 64 µM protein concentration, 20 mM HEPES, 10% PEG, 1000 mM NaCl at increasing 1-6-hexane-diol concentrations from 0 % (left) to 10% (right) in 2% steps. Scale bars are 10 µm. Representative DIC images and error bars showing standard deviations from n = 3 experiments.*

3.3.2.5. The extended C-terminal IDR of IM30 is not required for the formation carpet-like structures

IM30 as well as other ESCRT-III proteins have shown remarkable structural flexibility and to form different supramolecular assemblies[97–99,104,206,246]. When IM30 binds to lipid membranes *in vitro*, the IM30 barrel was shown to disassemble and result in the formation of carpet-like structures[104]. Fluorescently labeled IM30 occasionally showed an additional signal at the plasma membrane in fluorescence microscopy images apart from its prototypical punctae (**Figure 3.3-2**A, and section 3.2 **Supplementary figure 8.2-5**). This signal was enhanced for IM30* and truncated IM30 variants that contained the coiled-coil (**Figure 3.3-2**B-E). To see if the plasma membrane localization could be related to the formation of carpet-like structures we next compared the ability of truncated variants to assemble on a supported lipid bilayer (SLB).

The ability to form supramolecular assemblies on lipid membranes seems to be a prerequisite for ESCRT-III-mediated membrane remodeling. We previously described condensate formation of IM30 (section 3.2) which in theory could precede, be coupled to, modulate, and/or follow the formation of such membrane-associated IM30 assemblies. To identify regions of the protein that are required for carpet formation we applied atomic force microscopy (AFM) to IM30 variants in presence of a supported lipid bilayer (SLB).

IM30 shows typical carpet-like structures that appear as large areas of circular shape with an apparent height of ~2 nm above the background level of the SLB surface (**Figure 3.3-6**A). Similarly, the IM30* mutant shows similar circularly shaped areas at the SLB (**Figure 3.3-6**B) with an apparent height of ~1 nm. The truncated variant $IM30_{1\text{-}156}$ formed flat carpet-like structures with an apparent height of 1.5 nm (**Figure 3.3-6**C) and slightly more irregularly shaped edges, whereas no carpet formation or in fact any indication for membrane-bound protein was detected for $IM30_{157\text{-}267}$ (**Figure 3.3-6**D). $IM30_{157\text{-}267}$ was observed to lack membrane-binding capabilities in other studies from our group (data not shown). These results suggest that IM30 carpet formation requires the N-terminal domain containing the coiled-coil region and does not depend on its C-terminal extended IDR.

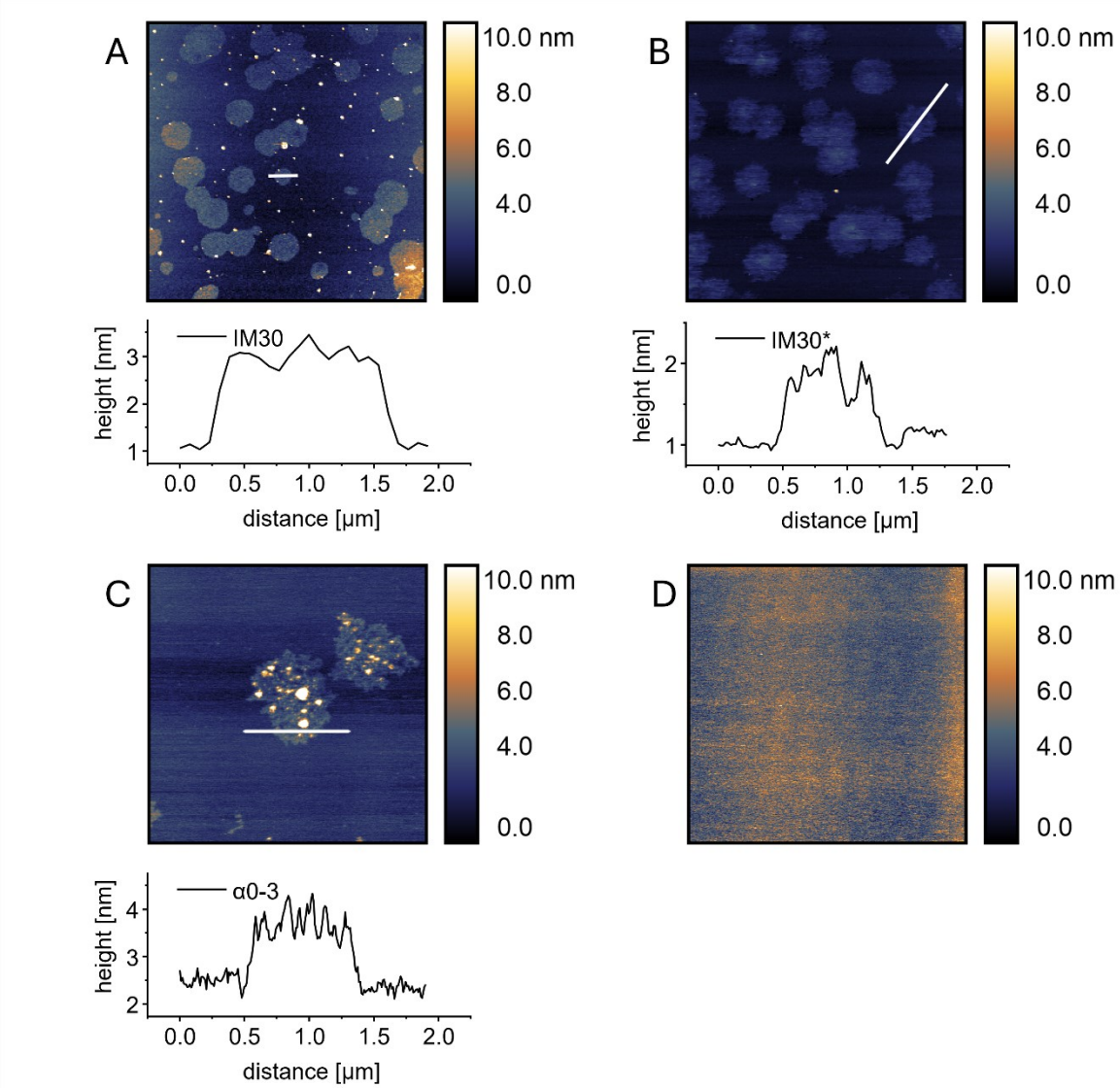

***Figure 3.3-6**: AFM topographic images and line profiles of differentIM30 variants after incubation on supported lipid bilayers. AFM image (top) and line profile (bottom) of 4 µM (A) IM30 wt, (B) 0.5 µM IM30*, (C) 0.75 µM $IM30_{26\text{-}156}$ and (D) 1.5 µM $IM30_{157\text{-}267}$ after incubation on a SLB made of 40% (mol) DOPG and 60 % (mol) DOPC (A-C) or DOPG (D); line profile was taken at positions indicated by a white line in the corresponding topographic image. imaged areas have the size of 20 µm (A, D) and 5 µm (B, C).*

3.3.3. Discussion

3.3.3.1. IM30 localization into punctae *in vivo* correlates with *in vitro* condensates propensity

By comparing the localization of different IM30 variants *in vivo* to their propensity to form condensates *in vitro* we provided further indication for the underlying type of assembly of IM30 *punctae* to be biomolecular condensates. IM30 variants that lack the C-terminal helices included in $IM30_{157-267}$ were previously shown to only form monomers in solution *in vitro*[137]. We showed that $IM30_{1-156}$ is, however, capable of localizing into *punctae* (**Figure 3.3-2**, **Figure *3.2-1***C, I) as well as form condensates (**Figure 3.3-3**A, C), which agrees well with our hypothesis that *punctae* are in fact not related to barrel formation but rather represent biomolecular condensates instead. This hypothesis was further supported by the fluorescence signal for $IM30_{157-267}$-mVenus being exclusively distributed throughout the cytosol (**Figure *3.2-1***F), similar to freely diffusing mVenus (**Figure *3.2-1***G, H), as this IM30 variant also did not form condensates *in vitro* (**Figure 3.3-3**A, F).

The truncated IM30 variants $IM30_{26-156}$ and $IM30_{26-136}$ were able to form condensates (**Figure 3.3-3**A, D, E) and thus the absence of *puncta* formation in these samples (**Figure *3.2-1***D, E) does not support the idea of *punctae* being related to IM30 condensates, but could be explained by comparing their condensate formation propensity *in vitro* (**Figure 3.3-3**, **Figure 3.3-4**) and considering the possibility of additional unknown factors for condensate formation *in vivo*. For example did the further truncation of the helical regions show decreased turbidity and less condensates for $IM30_{26-136}$ (α1-2) compared to $IM30_{26-156}$ (α1-3) and $IM30_{1-156}$ (α0-3) at equal concentrations (**Figure 3.3-3**A, C, D, E), which could explain the lack of punctae *in vivo* (**Figure 3.3-2**, **Figure *3.2-1***D, E). Even though there was no significant difference between $IM30_{26-156}$ and $IM30_{1-156}$ in terms of turbidity for PEG/NaCl-induced condensates (**Figure 3.3-3**A), we observed slightly lowered turbidity for PEG-induced condensates of $IM30_{26-156}$ compared to $IM30_{1-156}$ (**Figure 3.3-4**A). Even though these differences were not statistically significant in our turbidity data, our DIC images further supported the negative effect on condensate formation after removal of individual helices from $IM30_{1-156}$ (**Figure 3.3-4**C, D, E). To verify these observations, further statistical evaluation of droplet size and the collection of phase diagrams could be performed.

3.3.3.2. Coiled-coil interactions drive IM30 condensate formation

Transient interactions that can be important for condensate formation of proteins include electrostatic, hydrophobic, and cation-π interactions as well as π-π-stacking and hydrogen bonds[247]. We were able to show that IM30* forms condensates at pH 5.5 in absence of both crowding agent and NaCl (section 3.2). The pH as driving force and modulator for condensate formation was previously described in theoretical work[180,248], used in membrane model systems[249] and reported for proteins[250–252]. The condensate formation in response to pH was shown to involve electrostatic interactions that could be reduced by increasing the ionic strength leading to the dissolution of condensates[179,250]. Our data, however, showed no significant differences between condensates formed at pH 5.5 in absence and in presence of 100 mM NaCl (section 3.2.2.6), indicating that additional contributions from other interactions are important for IM30 condensate formation.

In presence of crowding agent IM30* condensate formation occurred at intermediate and even at high ionic strength (section 3.2.2.4) where electrostatic interactions should be negligible due to the electrostatic screening of charges and hydrophobic interactions start to dominate[189]. 1-6-Hexandiol is a common additive used to disrupt hydrophobic interactions and interactions involving aromatic residues *in vitro*[179,184,245,253–256] and is also frequently used, even though recently debated[257], for *in vivo* studies[65,245]. However, PEG/NaCl-induced IM30* condensates at high ionic strength did not dissolve in presence of hexane-diol and we only observed an apparent decrease in condensate size which was compensated by an increase in number of condensates (**Figure 3.3-5**). Therefore, hydrophobic interactions contribute at most partially to IM30 condensate formation.

IM30 has an obvious propensity to form interactions between helices in higher oligomeric barrel structures, where a single monomer can have interactions with up to 16 different monomers in the same barrel with C16 point symmetry[96] and helices form an interwoven network with conserved intermolecular interfaces[97,99]. We showed that all C-terminally truncated variants containing $IM30_{26\text{-}136}$ were able to form condensates (**Figure 3.3-3**). It was recently shown in simulations that coiled-coil interactions can be the driving force for condensate formation[244] and other proteins have previously been reported to rely on their coiled-coil regions for condensate formation, like the carboxysome positioning protein McdB[85], the endocytic trafficking protein Ede1[258] and many others[244]. Therefore, we hypothesize that attractive coiled-coil interactions mediated by a

combination of hydrogen bonds, hydrophobic interactions and electrostatic interactions involving $IM30_{26-136}$ drive IM30 condensate formation.

The observation of the dissolution of condensates with increasing urea concentrations (**Figure 3.3-5**) agreed with the idea that interactions between helices are important for condensate formation of IM30*. But since urea itself can have a strong effect on a multitude of interactions[259] we could not rule out that the dissolution was not, or only partially, attributed to the loss of secondary structure in the coiled-coil region. However, urea was commonly used to destabilize H-bonds in proteins and used to analyze the importance of H-bonds for condensate formation[179,192,260] for example by increasing concentrations from 0.5 M up to 2 M urea[179] and at these concentrations the central coiled-coil of IM30 was previously shown to still be largely intact (section 3.1). Therefore, a strong effect of secondary structure destabilization on condensate formation would be expected to become relevant only at urea concentrations above 2 M.

In this context, our data did not support a negligible effect of H-bonds on condensate formation of IM30* (**Figure 3.3-5**). Nevertheless, there were two observations that suggested that the helical interactions might be the actual driving force for IM30* condensate formation: (i) both the size of condensates observed in DIC microscopy, as well as turbidity in presence of 2 M urea were equal to sizes and turbidity values of $IM30_{1-156}$ at PEG-NaCl induced condensates in absence of urea (**Figure 3.3-3**, **Figure 3.3-5**). This suggested that urea dissolved interactions between the extended IDR comprising α4-6 and helices α0-3 of the N-terminal region that seemed to enhance condensate formation of IM30* compared to the truncated variants (**Figure 3.3-3**). Upon addition of urea these interactions were destabilized and led to smaller condensate sizes and decreased turbidity. To validate this assumption, a similar experiment applying the truncated variants would need to be performed to see if condensates formed by these variants are significantly less affected by urea concentrations up to 2 M and show the same dissolution of condensates at ≥ 3 M urea. (ii) A different reason could be that the observation on the stability of the coiled-coil region up to 2 M urea were made in absence of salt (section 3.1). It was previously shown that salt can have a strong influence on the oligomeric state of smaller IM30* oligomers[104]. Therefore, the addition of 100 mM NaCl could have an additional destabilizing effect on the coiled-coil in presence of urea and further experiments on the stability of IM30s central coiled-coil region in presence of NaCl

are required to provide a better overview on the applicable range of urea for the destabilization of IM30 barrel structures without affecting the structural integrity of the central coiled-coil.

Not only PEG/NaCl-, but also pH-induced condensates are dissolved by urea (**Figure 3.3-5**) , as well as pH induced condensates in presence of 100 mM NaCl (see section 3.2 and **Supplementary figure 8.2-10**), and condensates still form in presence of urea when both PEG and pH 5.5 are present (see section 3.2.2.6). This suggests an additive effect of pH and PEG for IM30 condensate formation. We hypothesized that the isolated IM30 coiled-coil forms condensates in presence of PEG, when IM30* does not, due to the differences in pI values (see main text to **Figure 3.3-4**) and/or because the extended C-terminal IDR is auto-inhibiting IM30* condensate formation in the absence of salt. Therefore, the observed rescue of IM30 condensate formation in presence of pH 5.5 and PEG from disruption by urea is likely caused by a lower critical saturation concentration compared to either pH 5.5 or PEG alone.

Additional experiments using truncated variants, employing controls for the effect of salt, and IM30 variants with locally destabilized helices are required to provide further evidence for the importance of helicity for IM30 condensate formation.

Taken together, our results suggest that a combination of hydrophobic interactions, electrostatic interactions, and hydrogen bonds, that are mediated by the coiled-coil, contribute to condensate formation in IM30.

3.3.3.3. The extended C-terminal IDR of IM30* modulates condensate formation propensity

Under crowding conditions we observed highly increased condensate formation propensity in presence of salt (**Figure 3.3-3**) in contrast to no condensate formation in absence of salt (**Figure 3.3-4**) for IM30* compared to the truncated IM30 variants that contain the coiled-coil, which showed little dependence on salt (**Figure 3.3-3**, **Figure 3.3-4**). This suggests an auto-inhibitory effect of the extended C-terminal domain, that is resolved in presence of salt, and could be attributed to the differences in pI values of the two sets of proteins.

IM30 has a basic N-terminal region (pI = 9.39 for native IM30 a0-3) and an acidic C-terminal region (pI = 3.99 for native IM30 a4-6) which is a common feature shared among members of the ESCRT-III protein family[261,262]. This charge separation could aid in the sequential assembly of

higher oligomers or carpet-like structures and further enhance condensate formation through electrostatic interactions between monomers but does not seem crucial for condensate formation since IM30 variants lacking the acidic C-terminal region are still able to form condensates (**Figure 3.3-4**). IM30* has a pI value of 5.75, where it forms condensates even in absence of the crowding agent PEG (see section 3.2.2.3), while the truncated variants containing the coiled-coil have much higher pI values of 8.06, 8.08 and 6.87 for $IM30_{1-156}$, $IM30_{26-156}$, and $IM30_{26-136}$, respectively. Thus, their pI values are all much closer to pH 7.6 of the buffer solution used in the experiment compared to IM30*. Since condensate formation is further promoted at pH values close to the proteins pI[180], the difference in pI values between IM30* and the truncated variants containing the coiled-coil could cause the difference in condensate formation in presence of solely PEG at pH 7.6 (**Figure 3.3-4**). Further experiments at more acidic pH could be used to test if the crowding agent PEG is merely promoting condensate formation by lowering the critical saturation concentration and verify if the pH is the actual determining factor for condensate formation in this context. In summary, our data indicates that the C-terminal extended IDR modulates IM30* condensate formation by inhibiting intermolecular interactions involving the coiled-coil through steric and/or electrostatic intramolecular interactions between the coiled-coil and the extended IDR at low ionic strength.

3.3.3.4. IM30 plasma membrane localization in vivo can be related to carpet-like structures in vitro

In our experiments fluorescently labeled IM30 showed some additional signal at the plasma membrane which became pronounced and covered larger areas of the plasma membrane for IM30*, $IM30_{1-156}$, $IM30_{26-156}$, and $IM30_{26-136}$. IM30 has been reported to have a plasma membrane localization[263,264], at the inner envelope for tobacco protoplasts in addition to its localization in *punctae* at the thylakoid membrane[94], .at the TM and inner envelope of chloroplasts[90,91], and at the TM and cytoplasmic membrane of Synechocystis[139]. Stress-induced formation of *punctae* as well as localization at the plasma membrane was also observed for bacterial ESCRT-III family members, *i. e.* PspA[171,172] and LiaH[173]. We now showed that the isolated extended C-terminal IDR of IM30 by itself does not localize into *punctae* and does not seem to bind membranes in general (**Figure 3.3-2**, **Figure *3.2-1***F). This is in good agreement with earlier studies in protoplasts from eukaryotes where a C-terminal truncation had no effect on IM30 localization whereas removal of the coiled-coil resulted in a dispersed signal throughout the stroma [94].

Barrel structures of IM30 reassemble into flat carpet-like structures upon binding to supported lipid bilayers (SLB)[104]. It was previously shown that formation of smaller oligomeric IM30 enhances membrane binding[111] and speeds up carpet formation[104]. This agrees well with our observation of enhanced plasma membrane signal for barrel impaired IM30 variants compared to the wildtype (**Figure *3.2-1***). By using AFM to visualize IM30 bound to lipid membranes we could confirm the formation of carpet-like membrane structures being retained for the structured N-terminal domain $IM30_{1-156}$ and lost for the extended C-terminal IDR $IM30_{157-267}$ (**Figure 3.3-6**). Thus, the observed plasma membrane localization (**Figure *3.2-1***) might indeed resemble some kind of carpet-like structure *in vivo* although the molecular structure of membrane-bound IM30 at these regions is still not known.

A recent study of another group succeeded in reporting the structural basis for the formation of flat spirals on membrane surfaces by IM30 of *Nostoc punctiforme*[206]. The reported spirals seem to be equivalent or at least related to the previously described carpet formation of IM30 in *Synechocystis* [104] and closely resemble the spiral formation that has been studied for other ESCRT-III proteins, like Snf7[132,265,266]. Spiral formation in eukaryotes is a sequential and highly regulated process that was suggested to involve monomer exchange by the AAA+ ATPase VPS4 resulting in buckling, tubulation, and fission due to changing preferential polymer curvatures [147,149,265]. The reported models for spirals formed by IM30 of *Nostoc punctiforme*[206] and other models reported for eukaryotic ESCRT-III spirals[132,246,267] indicate the existence of conserved intermolecular interfaces between monomers in spirals on lipid membranes that resemble the interfaces found in higher oligomeric structures in solution[96–99]. Most interestingly, removal of the C-terminal region from other ESCRT-III proteins was shown to result in localization of ESCRT-III proteins at the membrane[262], which fits to our observations made for truncated IM30 variants *in vitro* and *in vivo*. Here, we provided evidence for the coiled-coil region of $IM30_{1-156}$ being sufficient for carpet formation which fits our *in vivo* data and is in good agreement with previously reported data on ESCRT-III proteins that form carpet-like structures on membranes[132,206,246,266].

Additional AFM studies with $IM30_{26-156}$ and $IM30_{26-136}$ are required to find the minimal construct for carpet formation and will lead to a better understanding of *in vivo* membrane localization and determine the exact overlap between the ability to form condensates and carpet structures.

Interestingly, a recent study reported on the existence of a novel ESCRT-II-like protein, VIPP1-associated-protein 1 (VIA1), in plant chloroplasts (*arabidopsis thaliana*) and in green algae (*chlamydomonas reinhardtii*) containing a winged-helix (WH) domain, typical for ESCRT-II proteins. VIA1 was capable of binding IM30, also known as VIPP1, and was shown to co-localize with IM30 *in vivo*[268]. A homolog of this protein can also be found in *Synechocystis* by a BLAST search[269,270] using an ESCRT-II protein SNF8 from *Saccharomyces cerevisiae* (Uniprot-ID: Q55563) as a template. The protein, here referred to as SynVIA1, is encoded in the *slr1603* gene. A model generated by Alphafold-multimer[100,271] (version 3) implemented in the local version of ColabFold[272] with SynIM30 and SynVIA1 shows the same interaction interface between the SynIM30s coiled-coil region and the WH domain of SynVIA1 (**Supplementary figure 8.3-3**) as reported for the other VIA homologs in the recent publication[268]. This membrane-bound receptor could play a role in condensate formation at the membrane surface and/or be related to the formation of other IM30 assemblies on the membrane. This is further supported by the superimposed barrel structure aligning the neighboring IM30 monomer in the barrel structure surprisingly close to the second WH-like domain of the SynVIA1 monomer. This could hint towards a mechanism on how higher IM30 oligomeric assemblies like-barrels or carpet-like structures are initialized and how the transition of the extended IDR of non-oligomeric IM30 in solution towards a helical structure in the oligomer is regulated by positioning the coiled-coil regions in a defined for orientation to each other to facilitate potential oligomerization at the membrane. This receptor could thus be used by the cell to recruit IM30 to specific locations for oligomerization.

On the other hand, *in vitro* experiments on 2D-Phase separation[273–276] and theoretical studies on prewetting in the presence of membranes[79] show that membrane binding can lead to condensate formation on the membrane prior to condensate formation in the cytosol due to a decreased saturation concentration on the membrane. The authors of the theoretical study give a great overview on the different implications of membrane binding in presence and absence of additional membrane-bound receptors on the prewetting transitions and its relation to condensate formation in solution[79]. However, any evidence for 2D-phase separation of IM30 is still missing and possible changes in accessibility of amino acids that would participate in important transient interactions, or the formation of other stable structures such as carpet-like structures[104] upon membrane binding add more complexity and impede any reasonable assumptions.

Taken together, we have provided important evidence for similarities between the plasma membrane localization *in vivo* and the ability of IM30 variants to form carpet-like structures *in vitro*. Future studies will advance our understanding of the important factors and differences for the formation of *punctae*, carpet-like structures, higher oligomers, and condensates as well as the role of these multiple different supramolecular assemblies for the *in vivo* function of IM30.

4. References

1. Schopf JW, Packer BM (1987) Early Archean (3.3-Billion to 3.5-Billion-Year-Old) Microfossils from Warrawoona Group, Australia. Science (1979) 237:70–73.

2. Baumgartner RJ, Van Kranendonk MJ, Wacey D, Fiorentini ML, Saunders M, Caruso S, Pages A, Homann M, Guagliardo P (2019) Nano−porous pyrite and organic matter in 3.5-billion-year-old stromatolites record primordial life. Geology 47:1039–1043.

3. Sánchez-Baracaldo P, Cardona T (2020) On the origin of oxygenic photosynthesis and Cyanobacteria. New Phytologist 225:1440–1446.

4. Sleep NH, Bird DK (2008) Evolutionary ecology during the rise of dioxygen in the Earth's atmosphere. Philosophical Transactions of the Royal Society B: Biological Sciences 363:2651–2664.

5. Sánchez-Baracaldo P, Bianchini G, Wilson JD, Knoll AH (2022) Cyanobacteria and biogeochemical cycles through Earth history. Trends Microbiol 30:143–157.

6. Sánchez-Baracaldo P, Raven JA, Pisani D, Knoll AH (2017) Early photosynthetic eukaryotes inhabited low-salinity habitats. Proc Natl Acad Sci U S A 114:E7737–E7745.

7. Lyons TW, Reinhard CT, Planavsky NJ (2014) The rise of oxygen in Earth's early ocean and atmosphere. Nature 506:307–315.

8. Sánchez-Baracaldo P (2015) Origin of marine planktonic cyanobacteria. Sci Rep 5:17418.

9. Antonaru LA, Selinger VM, Jung P, Di Stefano G, Sanderson ND, Barker L, Wilson DJ, Büdel B, Canniffe DP, Billi D, et al. (2023) Common loss of far-red light photoacclimation in cyanobacteria from hot and cold deserts: a case study in the Chroococcidiopsidales. ISME Communications 3.

10. Pointing SB, Belnap J (2012) Microbial colonization and controls in dryland systems. Nat Rev Microbiol 10:551–562.

11. Field CB, Behrenfeld MJ, Randerson JT, Falkowski P (1998) Primary Production of the Biosphere: Integrating Terrestrial and Oceanic Components. Science (1979) 281:237–240.

12. Mangan NM, Flamholz A, Hood RD, Milo R, Savage DF (2016) PH determines the energetic efficiency of the cyanobacterial CO2 concentrating mechanism. Proc Natl Acad Sci U S A 113:E5354–E5362.

13. Zahra Z, Choo DH, Lee H, Parveen A (2020) Cyanobacteria: Review of Current Potentials and Applications. Environments 7:13.

14. Archibald JM (2015) Endosymbiosis and eukaryotic cell evolution. Current Biology 25:R911–R921.

15. Reyes-Prieto A, Weber APM, Bhattacharya D (2007) The Origin and Establishment of the Plastid in Algae and Plants. Annu Rev Genet 41:147–168.

16. Kaneko T, Sato S, Kotani H, Tanaka A, Asamizu E, Nakamura Y, Miyajima N, Hirosawa M, Sugiura M, Sasamoto S, et al. Sequence Analysis of the Genome of the Unicellular Cyanobacterium Synechocystis sp. Strain PCC6803. II. Sequence Determination of the Entire Genome and Assignment of Potential Protein-coding Regions. 1996.

17. Rippka R, Deruelles J, Waterbury JB (1979) Generic assignments, strain histories and properties of pure cultures of cyanobacteria. J Gen Microbiol 111:1–61.

18. Williams JGK (1988) Construction of Specific Mutations in Photosystem II Photosynthetic Reaction Center by Genetic Engineering Methods in Synechocystis 6803. Methods Enzymol 167:766–778.

19. BARTEN R, LILL H (1995) DNA-uptake in the naturally competent cyanobacterium, PCC 6803. FEMS Microbiol Lett 129:83–88.

20. Porter RD DNA transformation. In: Methods in Enzymology. Vol. 167. ; 1988. pp. 703–712.

21. Griese M, Lange C, Soppa J (2011) Ploidy in cyanobacteria. FEMS Microbiol Lett 323:124–131.

22. Šmarda J, Šmajs D, Komrska J, Krzyžánek V (2002) S-layers on cell walls of cyanobacteria. Micron 33:257–277.

23. Dou Z, Heinhorst S, Williams EB, Murin CD, Shively JM, Cannon GC (2008) CO2 Fixation Kinetics of Halothiobacillus neapolitanus Mutant Carboxysomes Lacking Carbonic Anhydrase

Suggest the Shell Acts as a Diffusional Barrier for CO2. Journal of Biological Chemistry 283:10377–10384.

24. Frost SC, McKenna R eds Carbonic Anhydrase: Mechanism, Regulation, Links to Disease, and Industrial Applications. Dordrecht: Springer Netherlands; 2014.

25. Cleland WW, Andrews TJ, Gutteridge S, Hartman FC, Lorimer GH (1998) Mechanism of Rubisco: The Carbamate as General Base. Chem Rev 98:549–562.

26. Hayer-Hartl M, Hartl FU (2020) Chaperone Machineries of Rubisco – The Most Abundant Enzyme. Trends Biochem Sci 45:748–763.

27. Wang H, Yan X, Aigner H, Bracher A, Nguyen ND, Hee WY, Long BM, Price GD, Hartl FU, Hayer-Hartl M (2019) Rubisco condensate formation by CcmM in β-carboxysome biogenesis. Nature 566:131–135.

28. Zang K, Wang H, Hartl FU, Hayer-Hartl M Scaffolding protein CcmM directs multiprotein phase separation in β-carboxysome biogenesis. Springer US; 2021.

29. Freeman Rosenzweig ES, Xu B, Kuhn Cuellar L, Martinez-Sanchez A, Schaffer M, Strauss M, Cartwright HN, Ronceray P, Plitzko JM, Förster F, et al. (2017) The Eukaryotic CO2-Concentrating Organelle Is Liquid-like and Exhibits Dynamic Reorganization. Cell 171:148-162.e19.

30. Rippka R, Waterbury J, Cohen-Bazire G (1974) A cyanobacterium which lacks thylakoids. Arch Microbiol 100:419–436.

31. Vothknecht UC, Westhoff P (2001) Biogenesis and origin of thylakoid membranes. Biochim Biophys Acta Mol Cell Res 1541:91–101.

32. Schneider D, Fuhrmann E, Scholz I, Hess WR, Graumann PL (2007) Fluorescence staining of live cyanobacterial cells suggest non-stringent chromosome segregation and absence of a connection between cytoplasmic and thylakoid membranes. BMC Cell Biol 8:1–10.

33. Liberton M, Howard Berg R, Heuser J, Roth R, Pakrasi HB (2006) Ultrastructure of the membrane systems in the unicellular cyanobacterium Synechocystis sp. strain PCC 6803. Protoplasma 227:129.

34. Mareš J, Strunecký O, Bučinská L, Wiedermannová J (2019) Evolutionary patterns of thylakoid architecture in Cyanobacteria. Front Microbiol 10:1–22.

35. Mullineaux CW (2014) Co-existence of photosynthetic and respiratory activities in cyanobacterial thylakoid membranes. Biochim Biophys Acta Bioenerg 1837:503–511.

36. Vermaas WF Photosynthesis and Respiration in Cyanobacteria. In: Encyclopedia of Life Sciences. Wiley; 2001.

37. Shimakawa G (2023) Electron transport in cyanobacterial thylakoid membranes: are cyanobacteria simple models for photosynthetic organisms? J Exp Bot 74:3476–3487.

38. Kugler A, Stensjö K (2023) Optimal energy and redox metabolism in the cyanobacterium Synechocystis sp. PCC 6803. NPJ Syst Biol Appl 9.

39. Kramer DM, Evans JR (2011) The Importance of Energy Balance in Improving Photosynthetic Productivity. Plant Physiol 155:70–78.

40. Johnson GN (2011) Physiology of PSI cyclic electron transport in higher plants. Biochimica et Biophysica Acta (BBA) - Bioenergetics 1807:384–389.

41. Liu LN (2016) Distribution and dynamics of electron transport complexes in cyanobacterial thylakoid membranes. Biochim Biophys Acta Bioenerg 1857:256–265.

42. Mullineaux CW, Allen JF (1990) State 1-State 2 transitions in the cyanobacterium Synechococcus 6301 are controlled by the redox state of electron carriers between Photosystems I and II. Photosynth Res 23:297–311.

43. Nixon PJ, Michoux F, Yu J, Boehm M, Komenda J (2010) Recent advances in understanding the assembly and repair of photosystem II. Ann Bot 106:1–16.

44. Zak E, Norling B, Maitra R, Huang F, Andersson B, Pakrasi HB (2001) The initial steps of biogenesis of cyanobacterial photosystems occur in plasma membranes. Proceedings of the National Academy of Sciences 98:13443–13448.

45. Stengel A, Gügel IL, Hilger D, Rengstl B, Jung H, Nickelsen J (2012) Initial steps of photosystem II de novo assembly and preloading with manganese take place in biogenesis centers in Synechocystis. Plant Cell 24:660–675.

46. Barthel S, Bernát G, Seidel T, Rupprecht E, Kahmann U, Schneider D (2013) Thylakoid membrane maturation and PSII activation are linked in greening Synechocystis sp. PCC 6803 cells1. Plant Physiol 163:1037–1046.

47. Rast A, Schaffer M, Albert S, Wan W, Pfeffer S, Beck F, Plitzko JM, Nickelsen J, Engel BD (2019) Biogenic regions of cyanobacterial thylakoids form contact sites with the plasma membrane. Nat Plants 5:436–446.

48. Rengstl B, Oster U, Stengel A, Nickelsen J (2011) An Intermediate Membrane Subfraction in Cyanobacteria Is Involved in an Assembly Network for Photosystem II Biogenesis. Journal of Biological Chemistry 286:21944–21951.

49. Selão TT, Zhang L, Knoppová J, Komenda J, Norling B (2016) Photosystem II Assembly Steps Take Place in the Thylakoid Membrane of the Cyanobacterium Synechocystis sp. PCC6803. Plant Cell Physiol 57:95–104.

50. Ostermeier M, Garibay-Hernández A, Holzer VJC, Schroda M, Nickelsen J (2024) Structure, biogenesis, and evolution of thylakoid membranes. Plant Cell 00:1–22.

51. Siebenaller C, Schneider D (2023) Cyanobacterial membrane dynamics in the light of eukaryotic principles. Biosci Rep 43.

52. Mullineaux CW, Liu LN (2020) Membrane Dynamics in Phototrophic Bacteria. Annu Rev Microbiol 74:633–654.

53. Rast A, Heinz S, Nickelsen J (2015) Biogenesis of thylakoid membranes. Biochim Biophys Acta Bioenerg 1847:821–830.

54. Klotz A, Georg J, Bučinská L, Watanabe S, Reimann V, Januszewski W, Sobotka R, Jendrossek D, Hess WR, Forchhammer K (2016) Awakening of a Dormant Cyanobacterium from Nitrogen Chlorosis Reveals a Genetically Determined Program. Current Biology 26:2862–2872.

55. Hennig R, Heidrich J, Saur M, Schmüser L, Roeters SJ, Hellmann N, Woutersen S, Bonn M, Weidner T, Markl J, et al. (2015) IM30 triggers membrane fusion in cyanobacteria and chloroplasts. Nat Commun 6.

56. Heinz S, Rast A, Shao L, Gutu A, Gügel IL, Heyno E, Labs M, Rengstl B, Viola S, Nowaczyk MM, et al. (2016) Thylakoid membrane architecture in Synechocystis depends on CurT, a homolog of the granal CURVATURE THYLAKOID1 proteins. Plant Cell 28:2238–2260.

57. Gewehr L, Junglas B, Jilly R, Franz J, Zhu WE, Weidner T, Bonn M, Sachse C, Schneider D (2023) SynDLP is a dynamin-like protein of Synechocystis sp. PCC 6803 with eukaryotic features. Nat Commun 14.

58. Banani SF, Lee HO, Hyman AA, Rosen MK (2017) Biomolecular condensates: organizers of cellular biochemistry. Nat Rev Mol Cell Biol 18:285–298.

59. Lyon AS, Peeples WB, Rosen MK (2021) A framework for understanding the functions of biomolecular condensates across scales. Nat Rev Mol Cell Biol 22:215–235.

60. Alberti S, Gladfelter A, Mittag T (2019) Considerations and Challenges in Studying Liquid-Liquid Phase Separation and Biomolecular Condensates. Cell 176:419–434.

61. Pak CW, Kosno M, Holehouse AS, Padrick SB, Mittal A, Ali R, Yunus AA, Liu DR, Pappu R V., Rosen MK (2016) Sequence Determinants of Intracellular Phase Separation by Complex Coacervation of a Disordered Protein. Mol Cell 63:72–85.

62. Mittag T, Pappu R V. (2022) A conceptual framework for understanding phase separation and addressing open questions and challenges. Mol Cell 82:2201–2214.

63. Harmon TS, Holehouse AS, Rosen MK, Pappu R V. (2017) Intrinsically disordered linkers determine the interplay between phase separation and gelation in multivalent proteins. Elife 6:1–31.

64. Gouveia B, Kim Y, Shaevitz JW, Petry S, Stone HA, Brangwynne CP (2022) Capillary forces generated by biomolecular condensates. Nature 609:255–264.

65. Bergeron-Sandoval LP, Kumar S, Heris HK, Chang CLA, Cornell CE, Keller SL, François P, Hendricks AG, Ehrlicher AJ, Pappu R V., et al. (2021) Endocytic proteins with prion-like domains form viscoelastic condensates that enable membrane remodeling. Proc Natl Acad Sci U S A 118.

66. Farag M, Borcherds WM, Bremer A, Mittag T, Pappu R V. (2023) Phase separation of protein mixtures is driven by the interplay of homotypic and heterotypic interactions. Nat Commun 14:5527.

67. Lemke EA, Babu MM, Kriwacki RW, Mittag T, Pappu R V., Wright PE, Forman-Kay JD (2024) Intrinsic disorder: A term to define the specific physicochemical characteristic of protein conformational heterogeneity. Mol Cell 84:1188–1190.

68. Oldfield CJ, Dunker AK (2014) Intrinsically Disordered Proteins and Intrinsically Disordered Protein Regions. Annu Rev Biochem 83:553–584.

69. Dunker AK, Cortese MS, Romero P, Iakoucheva LM, Uversky VN (2005) Flexible nets. FEBS J 272:5129–5148.

70. Kriwacki RW, Hengst L, Tennant L, Reed SI, Wright PE (1996) Structural studies of p21Waf1/Cip1/Sdi1 in the free and Cdk2-bound state: conformational disorder mediates binding diversity. Proceedings of the National Academy of Sciences 93:11504–11509.

71. Gardner KAJA, Moore DA, Erickson HP (2013) The C-terminal linker of Escherichia coli FtsZ functions as an intrinsically disordered peptide. Mol Microbiol 89:264–275.

72. Brangwynne CP, Eckmann CR, Courson DS, Rybarska A, Hoege C, Gharakhani J, Jülicher F, Hyman AA (2009) Germline P Granules Are Liquid Droplets That Localize by Controlled Dissolution/Condensation. Science (1979) 324:1729–1732.

73. Patel A, Lee HO, Jawerth L, Maharana S, Jahnel M, Hein MY, Stoynov S, Mahamid J, Saha S, Franzmann TM, et al. (2015) A Liquid-to-Solid Phase Transition of the ALS Protein FUS Accelerated by Disease Mutation. Cell 162:1066–1077.

74. Zeng M, Shang Y, Araki Y, Guo T, Huganir RL, Zhang M (2016) Phase Transition in Postsynaptic Densities Underlies Formation of Synaptic Complexes and Synaptic Plasticity. Cell 166:1163-1175.e12.

75. Milovanovic D, Wu Y, Bian X, De Camilli P (2018) A liquid phase of synapsin and lipid vesicles. Science (1979) 361:604–607.

76. Celetti G, Paci G, Caria J, VanDelinder V, Bachand G, Lemke EA (2020) The liquid state of FG-nucleoporins mimics permeability barrier properties of nuclear pore complexes. Journal of Cell Biology 219.

77. Feric M, Vaidya N, Harmon TS, Mitrea DM, Zhu L, Richardson TM, Kriwacki RW, Pappu R V., Brangwynne CP (2016) Coexisting Liquid Phases Underlie Nucleolar Subcompartments. Cell 165:1686–1697.

78. Ditlev JA (2021) Membrane-associated phase separation: organization and function emerge from a two-dimensional milieu. J Mol Cell Biol 13:319–324.

79. Zhao X, Bartolucci G, Honigmann A, Jülicher F, Weber CA (2021) Thermodynamics of wetting, prewetting and surface phase transitions with surface binding. New J Phys 23.

80. Saurabh S, Chong TN, Bayas C, Dahlberg PD, Cartwright HN, Moerner WE, Shapiro L ATP-responsive biomolecular condensates tune bacterial kinase signaling. 2022.

81. Azaldegui CA, Vecchiarelli AG, Biteen JS (2021) The emergence of phase separation as an organizing principle in bacteria. Biophys J 120:1123–1138.

82. Guilhas B, Walter JC, Rech J, David G, Walliser NO, Palmeri J, Mathieu-Demaziere C, Parmeggiani A, Bouet JY, Le Gall A, et al. (2020) ATP-Driven Separation of Liquid Phase Condensates in Bacteria. Mol Cell 79:293-303.e4.

83. Monterroso B, Zorrilla S, Sobrinos-Sanguino M, Robles-Ramos MA, López-Álvarez M, Margolin W, Keating CD, Rivas G (2019) Bacterial FtsZ protein forms phase-separated condensates with its nucleoid-associated inhibitor SlmA. EMBO Rep 20.

84. Al-Husini N, Tomares DT, Bitar O, Childers WS, Schrader JM (2018) α-Proteobacterial RNA Degradosomes Assemble Liquid-Liquid Phase-Separated RNP Bodies. Mol Cell 71:1027-1039.e14.

85. Basalla JL, Mak CA, Byrne J, Ghalmi M, Hoang Y, Vecchiarelli AG (2023) Dissecting the phase separation and oligomerization activities of the carboxysome positioning protein McdB. Elife 12:1–27.

86. Whitman BT, Wang Y, Murray CRA, Glover MJN, Owttrim GW (2023) Liquid-Liquid Phase Separation of the DEAD-Box Cyanobacterial RNA Helicase Redox (CrhR) into Dynamic Membraneless Organelles in *Synechocystis* sp. Strain PCC 6803 Buan NR, editor. Appl Environ Microbiol.

87. Pattanayak GK, Liao Y, Wallace EWJ, Budnik B, Drummond DA, Rust MJ (2020) Daily Cycles of Reversible Protein Condensation in Cyanobacteria. Cell Rep 32:108032.

88. Cohan MC, Pappu R V. (2020) Making the Case for Disordered Proteins and Biomolecular Condensates in Bacteria. Trends Biochem Sci 45:668–680.

89. Gao Z, Zhang W, Chang R, Zhang S, Yang G, Zhao G (2021) Liquid-Liquid Phase Separation: Unraveling the Enigma of Biomolecular Condensates in Microbial Cells. Front Microbiol 12.

90. Li HS-M, Kaneko Y, Keegstra K Molecular Cloning of a Chloroplastic ProteinAssociated with both the Envelope and Thylakoid Membranes. 1994.

91. Kroll D, Meierhoff K, Bechtold N, Kinoshita M, Westphal S, Vothknecht UC, Soll J, Westhoff P (2001) VIPP1 , a nuclear gene of Arabidopsis thaliana essential for thylakoid membrane formation. Proceedings of the National Academy of Sciences 98:4238–4242.

92. Zhang L, Kato Y, Otters S, Vothknecht UC, Sakamoto W (2012) Essential role of VIPP1 in chloroplast envelope maintenance in Arabidopsis. Plant Cell 24:3695–3707.

93. Nordhues A, Schöttler MA, Unger AK, Geimer S, Schönfelder S, Schmollinger S, Rütgers M, Finazzi G, Soppa B, Sommer F, et al. (2012) Evidence for a role of VIPP1 in the structural organization of the photosynthetic apparatus in Chlamydomonas. Plant Cell 24:637–659.

94. Aseeva E, Ossenbühl F, Eichacker LA, Wanner G, Soll J, Vothknecht UC (2004) Complex formation of Vipp1 depends on its alpha-helical PspA-like domain. J Biol Chem 279:35535–41.

95. Westphal S, Heins L, Soll J, Vothknecht UC (2001) Vipp1 deletion mutant of Synechocystis: A connection between bacterial phage shock and thylakoid biogenesis? Proceedings of the National Academy of Sciences 98:4243–4248.

96. Gupta TK, Klumpe S, Gries K, Heinz S, Wietrzynski W, Ohnishi N, Niemeyer J, Spaniol B, Schaffer M, Rast A, et al. (2021) Structural basis for VIPP1 oligomerization and maintenance of thylakoid membrane integrity. Cell 184:3643-3659.e23.

97. Liu J, Tassinari M, Souza DP, Naskar S, Noel JK, Bohuszewicz O, Buck M, Williams TA, Baum B, Low HH (2021) Bacterial Vipp1 and PspA are members of the ancient ESCRT-III membrane-remodeling superfamily. Cell:1–14.

98. Junglas B, Huber ST, Heidler T, Schlösser L, Mann D, Hennig R, Clarke M, Hellmann N, Schneider D, Sachse C (2021) PspA adopts an ESCRT-III-like fold and remodels bacterial membranes. Cell:1–15.

99. Schlösser L, Sachse C, Low HH, Schneider D (2023) Conserved structures of ESCRT-III superfamily members across domains of life. Trends Biochem Sci 48:993–1004.

100. Evans R, O'Neill M, Pritzel A, Antropova N, Senior A, Green T, Žídek A, Bates R, Blackwell S, Yim J, et al. (2022) Protein complex prediction with AlphaFold-Multimer. bioRxiv:2021.10.04.463034.

101. Kreis E, König K, Misir M, Niemeyer J, Sommer F, Schroda M (2023) TurboID reveals the proxiomes of Chlamydomonas proteins involved in thylakoid biogenesis and stress response. Plant Physiol.

102. Wang J, Chitsaz F, Derbyshire MK, Gonzales NR, Gwadz M, Lu S, Marchler GH, Song JS, Thanki N, Yamashita RA, et al. (2023) The conserved domain database in 2023. Nucleic Acids Res 51:D384–D388.

103. Jumper J, Evans R, Pritzel A, Green T, Figurnov M, Ronneberger O, Tunyasuvunakool K, Bates R, Žídek A, Potapenko A, et al. (2021) Highly accurate protein structure prediction with AlphaFold. Nature 596:583–589.

104. Junglas B, Orru R, Axt A, Siebenaller C, Steinchen W, Heidrich J, Hellmich UA, Hellmann N, Wolf E, Weber SAL, et al. (2020) IM30 IDPs form a membrane-protective carpet upon super-complex disassembly. Commun Biol 3:595.

105. Heidrich J, Junglas B, Grytsyk N, Hellmann N, Rusitzka K, Gebauer W, Markl J, Hellwig P, Schneider D (2018) Mg2+ binding triggers rearrangement of the IM30 ring structure, resulting in

augmented exposure of hydrophobic surfaces competent for membrane binding. J Biol Chem 293:8230–8241.

106. Hennig R, West A, Debus M, Saur M, Markl J, Sachs JN, Schneider D (2017) The IM30/Vipp1 C-terminus associates with the lipid bilayer and modulates membrane fusion. Biochim Biophys Acta Bioenerg 1858:126–136.

107. Gutu A, Chang F, O'Shea EK (2018) Dynamical localization of a thylakoid membrane binding protein is required for acquisition of photosynthetic competency. Mol Microbiol 108:16–31.

108. Gates C, Hill NC, Dahlgren K, Cameron JC (2023) Kinetics and targeting of Vipp1 aggregation in cyanobacteria.

109. Kelly CL, Taylor GM, Hitchcock A, Torres-Méndez A, Heap JT (2018) A Rhamnose-Inducible System for Precise and Temporal Control of Gene Expression in Cyanobacteria. ACS Synth Biol 7:1056–1066.

110. Fuhrmann E, Gathmann S, Rupprecht E, Golecki J, Schneider D (2009) Thylakoid membrane reduction affects the photosystem stoichiometry in the cyanobacterium Synechocystis sp. PCC 6803. Plant Physiol 149:735–744.

111. Heidrich J, Wulf V, Hennig R, Saur M, Markl J, Sönnichsen C, Schneider D (2016) Organization into higher ordered ring structures counteracts membrane binding of IM30, a protein associated with inner membranes in chloroplasts and cyanobacteria. Journal of Biological Chemistry 291:14954–14962.

112. Bryan SJ, Burroughs NJ, Shevela D, Yu J, Rupprecht E, Liu L-N, Mastroianni G, Xue Q, Llorente-Garcia I, Leake MC, et al. (2014) Localisation and interactions of the Vipp1 protein in cyanobacteria. Mol Microbiol 94:1179.

113. Bradford MM (1976) A rapid and sensitive method for the quantitation of microgram quantities of protein utilizing the principle of protein-dye binding. Anal Biochem 72:248–254.

114. Greene RF, Pace CN (1974) Urea and Guanidine Hydrochloride Denaturation of Ribonuclease, Lysozyme, α-Chymotrypsin, and b-Lactoglobulin. Journal of Biological Chemistry 249:5388–5393.

115. Bereau T, Deserno M (2009) Generic coarse-grained model for protein folding and aggregation. Journal of Chemical Physics 130.

116. Best RB, Hummer G (2009) Optimized molecular dynamics force fields applied to the helix-coil transition of polypeptides. Journal of Physical Chemistry B 113:9004–9015.

117. Girard M, Ehlen A, Shakya A, Bereau T, de la Cruz MO (2019) Hoobas: A highly object-oriented builder for molecular dynamics. Comput Mater Sci 167:25–33.

118. Anderson JA, Glaser J, Glotzer SC (2020) HOOMD-blue: A Python package for high-performance molecular dynamics and hard particle Monte Carlo simulations. Comput Mater Sci 173.

119. Zillmer H (2021) Interactions and phase behaviour of Ubiquilin-2.

120. Schindelin J, Arganda-Carreras I, Frise E, Kaynig V, Longair M, Pietzsch T, Preibisch S, Rueden C, Saalfeld S, Schmid B, et al. (2012) Fiji: an open-source platform for biological-image analysis. Nature Methods 2012 9:7 9:676–682.

121. Brangwynne CP, Mitchison TJ, Hyman AA (2011) Active liquid-like behavior of nucleoli determines their size and shape in Xenopus laevis oocytes. Proc Natl Acad Sci U S A 108:4334–4339.

122. Muzzopappa F, Hummert J, Anfossi M, Tashev SA, Herten DP, Erdel F (2022) Detecting and quantifying liquid–liquid phase separation in living cells by model-free calibrated half-bleaching. Nat Commun 13:1–15.

123. Nečas D, Klapetek P (2012) Gwyddion: an open-source software for SPM data analysis. Open Physics 10:181–188.

124. Darwin AJ (2005) The phage-shock-protein response. Mol Microbiol 57:621–628.

125. Manganelli R, Gennaro ML (2017) Protecting from Envelope Stress: Variations on the Phage-Shock-Protein Theme. Trends Microbiol 25:205–216.

126. Popp PF, Gumerov VM, Andrianova EP, Bewersdorf L, Mascher T, Zhulin IB, Wolf D (2022) Phyletic Distribution and Diversification of the Phage Shock Protein Stress Response System in Bacteria and Archaea. mSystems 7.

127. Vothknecht UC, Otters S, Hennig R, Schneider D (2012) Vipp1: a very important protein in plastids?! J Exp Bot 63:1699–1712.

128. Bultema JB, Fuhrmann E, Boekema EJ, Schneider D (2010) Vipp1 and PspA: Related but not twins. Commun Integr Biol 3:162–5.

129. Theis J, Gupta TK, Klingler J, Wan W, Albert S, Keller S, Engel BD, Schroda M (2019) VIPP1 rods engulf membranes containing phosphatidylinositol phosphates. Sci Rep 9:8725.

130. Liu C, Willmund F, Golecki JR, Cacace S, Heß B, Markert C, Schroda M (2007) The chloroplast HSP70B-CDJ2-CGE1 chaperones catalyse assembly and disassembly of VIPP1 oligomers in Chlamydomonas. Plant Journal 50:265–277.

131. Zhang L, Kondo H, Kamikubo H, Kataoka M, Sakamoto W (2016) VIPP1 Has a Disordered C-Terminal Tail Necessary for Protecting Photosynthetic Membranes against Stress. Plant Physiol 171:1983–1995.

132. Tang S, Henne WM, Borbat PP, Buchkovich NJ, Freed JH, Mao Y, Fromme JC, Emr SD (2015) Structural basis for activation, assembly and membrane binding of ESCRT-III Snf7 filaments. Elife 4:1–22.

133. Heidrich J, Thurotte A, Schneider D (2017) Specific interaction of IM30/Vipp1 with cyanobacterial and chloroplast membranes results in membrane remodeling and eventually in membrane fusion. Biochim Biophys Acta Biomembr 1859:537–549.

134. Zhen Y, Radulovic M, Vietri M, Stenmark H (2021) Sealing holes in cellular membranes. EMBO J 40.

135. Siebenaller C, Junglas B, Lehmann A, Hellmann N, Schneider D (2020) Proton Leakage Is Sensed by IM30 and Activates IM30-Triggered Membrane Fusion. Int J Mol Sci 21:4530.

136. Siebenaller C, Junglas B, Schneider D (2019) Functional Implications of Multiple IM30 Oligomeric States. Front Plant Sci 10.

137. Thurotte A, Schneider D (2019) The Fusion Activity of IM30 Rings Involves Controlled Unmasking of the Fusogenic Core. Front Plant Sci 10:1–12.

138. Siebenaller C, Schlösser L, Junglas B, Schmidt-Dengler M, Jacob D, Hellmann N, Sachse C, Helm M, Schneider D (2021) Binding and/or hydrolysis of purine-based nucleotides is not required for IM30 ring formation. FEBS Lett 595:1876–1885.

139. Fuhrmann E, Bultema JB, Kahmann U, Rupprecht E, Boekema EJ, Schneider D (2009) The vesicle-inducing protein 1 from Synechocystis sp. PCC 6803 organizes into diverse higher-ordered ring structures. Mol Biol Cell 20:4620–8.

140. Lopez AJ, Martínez L (2018) Parametric models to compute tryptophan fluorescence wavelengths from classical protein simulations. J Comput Chem 39:1249–1258.

141. Holtzer ME, Holtzer A (1995) The use of spectral decomposition via the convex constraint algorithm in interpreting the CD-observed unfolding transitions of C coils. Biopolymers 36:365–379.

142. Monera OD, Zhou NE, Kay CM, Hodges RS (1993) Comparison of antiparallel and parallel two-stranded α-helical coiled-coils: Design, synthesis, and characterization. Journal of Biological Chemistry 268:19218–19227.

143. Liu C, Willmund F, Whitelegge JP, Hawat S, Knapp B, Lodha M, Schroda M (2005) J-Domain Protein CDJ2 and HSP70B Are a Plastidic Chaperone Pair That Interacts with Vesicle-Inducing Protein in Plastids 1. Mol Biol Cell 16:1165–1177.

144. Shestakova A, Hanono A, Drosner S, Curtiss M, Davies BA, Katzmann DJ, Babst M (2010) Assembly of the AAA ATPase Vps4 on ESCRT-III Lemmon S, editor. Mol Biol Cell 21:1059–1071.

145. Vietri M, Radulovic M, Stenmark H (2020) The many functions of ESCRTs. Nat Rev Mol Cell Biol 21:25–42.

146. Alonso Y Adell M, Migliano SM, Teis D (2016) ESCRT-III and Vps4: a dynamic multipurpose tool for membrane budding and scission. FEBS Journal 283:3288–3302.

147. Mierzwa BE, Chiaruttini N, Redondo-Morata L, Moser Von Filseck J, König J, Larios J, Poser I, Müller-Reichert T, Scheuring S, Roux A, et al. (2017) Dynamic subunit turnover in ESCRT-III assemblies is regulated by Vps4 to mediate membrane remodelling during cytokinesis. Nat Cell Biol 19:787–798.

148. Jiang X, Harker-Kirschneck L, Vanhille-Campos C, Pfitzner AK, Lominadze E, Roux A, Baum B, Šarić A (2022) Modelling membrane reshaping by staged polymerization of ESCRT-III filaments. PLoS Comput Biol 18:1–15.

149. Pfitzner AK, Moser von Filseck J, Roux A (2021) Principles of membrane remodeling by dynamic ESCRT-III polymers. Trends Cell Biol 31:856–868.

150. Pfitzner AK, Mercier V, Jiang X, Moser von Filseck J, Baum B, Šarić A, Roux A (2020) An ESCRT-III Polymerization Sequence Drives Membrane Deformation and Fission. Cell 182:1140-1155.e18.

151. McCullough J, Frost A, Sundquist WI (2018) Structures, Functions, and Dynamics of ESCRT-III/Vps4 Membrane Remodeling and Fission Complexes. Annu Rev Cell Dev Biol 34:85–109.

152. Allison R, Lumb JH, Fassier C, Connell JW, Ten Martin D, Seaman MNJ, Hazan J, Reid E (2013) An ESCRT–spastin interaction promotes fission of recycling tubules from the endosome. Journal of Cell Biology 202:527–543.

153. McCullough J, Clippinger AK, Talledge N, Skowyra ML, Saunders MG, Naismith T V., Colf LA, Afonine P, Arthur C, Sundquist WI, et al. (2015) Structure and membrane remodeling activity of ESCRT-III helical polymers. Science (1979) 350:1548–1551.

154. Schöneberg J, Lee I-H, Iwasa JH, Hurley JH (2017) Reverse-topology membrane scission by the ESCRT proteins. Nat Rev Mol Cell Biol 18:5–17.

155. Remec Pavlin M, Hurley JH (2020) The ESCRTs - converging on mechanism. J Cell Sci 133.

156. Hurley JH (2015) ESCRTs are everywhere. EMBO J 34:2398–2407.

157. Wideman JG, Leung KF, Field MC, Dacks JB (2014) The cell biology of the endocytic system from an evolutionary perspective. Cold Spring Harb Perspect Biol 6:1–12.

158. Christ L, Raiborg C, Wenzel EM, Campsteijn C, Stenmark H (2017) Cellular Functions and Molecular Mechanisms of the ESCRT Membrane-Scission Machinery. Trends Biochem Sci 42:42–56.

159. Carlton JG, Baum B (2023) Roles of ESCRT-III polymers in cell division across the tree of life. Curr Opin Cell Biol 85:102274.

160. Adams H, Teertstra W, Demmers J, Boesten R, Tommassen J (2003) Interactions between phage-shock proteins in Escherichia coli. J Bacteriol 185:1174–1180.

161. Osadnik H, Schöpfel M, Heidrich E, Mehner D, Lilie H, Parthier C, Risselada HJ, Grubmüller H, Stubbs MT, Brüser T (2015) PspF-binding domain PspA1-144 and the PspA·F complex: New insights into the coiled-coil-dependent regulation of AAA+ proteins. Mol Microbiol 98:743–759.

162. Elderkin S, Jones S, Schumacher J, Studholme D, Buck M (2002) Mechanism of Action of the Escherichia coli Phage Shock Protein PspA in Repression of the AAA Family Transcription Factor PspF. J Mol Biol 320:23–37.

163. Ye F, Gao F, Liu X, Buck M, Zhang X (2022) Mechanisms of DNA opening revealed in AAA+ transcription complex structures. Sci Adv 8.

164. Jovanovic G, Mehta P, McDonald C, Davidson AC, Uzdavinys P, Ying L, Buck M (2014) The N-terminal amphipathic helices determine regulatory and effector functions of phage shock protein A (PspA) in escherichia coli. J Mol Biol 426:1498–1511.

165. Joly N, Engl C, Jovanovic G, Huvet M, Toni T, Sheng X, Stumpf MPH, Buck M (2010) Managing membrane stress: The phage shock protein (Psp) response, from molecular mechanisms to physiology. FEMS Microbiol Rev 34:797–827.

166. Wang M, Chan EWC, Wan Y, Wong MH yin, Chen S (2021) Active maintenance of proton motive force mediates starvation-induced bacterial antibiotic tolerance in Escherichia coli. Commun Biol 4:1–11.

167. Kobayashi R, Suzuki T, Yoshida M (2007) Escherichia coli phage-shock protein A (PspA) binds to membrane phospholipids and repairs proton leakage of the damaged membranes. Mol Microbiol 66:100–109.

168. Zhang L, Kusaba M, Tanaka A, Sakamoto W (2016) Protection of Chloroplast Membranes by VIPP1 Rescues Aberrant Seedling Development in Arabidopsis nyc1 Mutant. Front Plant Sci 7:533.

169. McDonald C, Jovanovic G, Ces O, Buck M (2015) Membrane Stored Curvature Elastic Stress Modulates Recruitment of Maintenance Proteins PspA and Vipp1. mBio 6:e01188-15.

170. McDonald C, Jovanovic G, Wallace BA, Ces O, Buck M (2017) Structure and function of PspA and Vipp1 N-terminal peptides: Insights into the membrane stress sensing and mitigation. Biochimica et Biophysica Acta (BBA) - Biomembranes 1859:28–39.

171. Yamaguchi S, Reid DA, Rothenberg E, Darwin AJ (2013) Changes in Psp protein binding partners, localization and behaviour upon activation of the Yersinia enterocolitica phage shock protein response. Mol Microbiol 87:656–671.

172. Engl C, Jovanovic G, Lloyd LJ, Murray H, Spitaler M, Ying L, Errington J, Buck M (2009) In vivo localizations of membrane stress controllers PspA and PspG in Escherichia coli. Mol Microbiol 73:382–396.

173. Domínguez-Escobar J, Wolf D, Fritz G, Höfler C, Wedlich-Söldner R, Mascher T (2014) Subcellular localization, interactions and dynamics of the phage-shock protein-like Lia response in Bacillus subtilis. Mol Microbiol 92:716–732.

174. Alberti S, Dormann D (2019) Liquid-Liquid Phase Separation in Disease. Annu Rev Genet 53:171–194.

175. Shin Y, Brangwynne CP (2017) Liquid phase condensation in cell physiology and disease. Science (1979) 357.

176. Hyman AA, Weber CA, Jülicher F (2014) Liquid-liquid phase separation in biology. Annu Rev Cell Dev Biol 30:39–58.

177. Ellis RJ (2001) Macromolecular crowding: an important but neglected aspect of the intracellular environment. Curr Opin Struct Biol 11:114–119.

178. André AAM, Spruijt E (2020) Liquid–liquid phase separation in crowded environments. Int J Mol Sci 21:1–20.

179. Poudyal M, Patel K, Gadhe L, Sawner AS, Kadu P, Datta D, Mukherjee S, Ray S, Navalkar A, Maiti S, et al. (2023) Intermolecular interactions underlie protein/peptide phase separation irrespective of sequence and structure at crowded milieu. Nat Commun 14.

180. Adame-Arana O, Weber CA, Zaburdaev V, Prost J, Jülicher F (2020) Liquid Phase Separation Controlled by pH. Biophys J 119:1590–1605.

181. Belkin S, Mehlhorn RJ, Packer L (1987) Proton Gradients in Intact Cyanobacteria. Plant Physiol 84:25–30.

182. Riback JA, Katanski CD, Kear-Scott JL, Pilipenko E V., Rojek AE, Sosnick TR, Drummond DA (2017) Stress-Triggered Phase Separation Is an Adaptive, Evolutionarily Tuned Response. Cell 168:1028-1040.e19.

183. Zhang Y, Xu N, Yan C, Zhou X, Qiao Q, Miao L, Xu Z (2024) Live-Cell Imaging to Resolve Salt-Induced Liquid-Liquid Phase Separation of FUS Protein by Dye Self-Labeling. Chemical and Biomedical Imaging 2:70–80.

184. Krainer G, Welsh TJ, Joseph JA, Espinosa JR, Wittmann S, de Csilléry E, Sridhar A, Toprakcioglu Z, Gudiškytė G, Czekalska MA, et al. (2021) Reentrant liquid condensate phase of proteins is stabilized by hydrophobic and non-ionic interactions. Nat Commun 12.

185. Peschek GA, Czerny T, Schmetterer G, Nitschmann WH (1985) Transmembrane Proton Electrochemical Gradients in Dark Aerobic and Anaerobic Cells of the Cyanobacterium (Blue-Green Alga) Anacystis nidulans: Evidence for Respiratory Energy Transduction in the Plasma Membrane. Plant Physiol 79:278–284.

186. Wohl S, Jakubowski M, Zheng W (2021) Salt-Dependent Conformational Changes of Intrinsically Disordered Proteins.

187. Hagemann M, Fulda S, Schubert H (1994) DNA, RNA, and protein synthesis in the cyanobacterium Synechocystis sp. PCC 6803 adapted to different salt concentrations. Curr Microbiol 28:201–207.

188. Elbaum-Garfinkle S, Kim Y, Szczepaniak K, Chen CCH, Eckmann CR, Myong S, Brangwynne CP (2015) The disordered P granule protein LAF-1 drives phase separation into droplets with tunable viscosity and dynamics. Proc Natl Acad Sci U S A 112:7189–7194.

189. Vancraenenbroeck R, Harel YS, Zheng W, Hofmann H (2019) Polymer effects modulate binding affinities in disordered proteins. Proc Natl Acad Sci U S A 116:19506–19512.

190. Van Lindt J, Bratek-Skicki A, Nguyen PN, Pakravan D, Durán-Armenta LF, Tantos A, Pancsa R, Van Den Bosch L, Maes D, Tompa P (2021) A generic approach to study the kinetics of liquid–liquid phase separation under near-native conditions. Commun Biol 4:2–9.

191. Franzmann TM, Jahnel M, Pozniakovsky A, Mahamid J, Holehouse AS, Nüske E, Richter D, Baumeister W, Grill SW, Pappu R V., et al. (2018) Phase separation of a yeast prion protein promotes cellular fitness. Science (1979) 359.

192. Guo Q, Zou G, Qian X, Chen S, Gao H, Yu J (2022) Hydrogen-bonds mediate liquid-liquid phase separation of mussel derived adhesive peptides. Nat Commun 13:5771.

193. Ray S, Singh N, Kumar R, Patel K, Pandey S, Datta D, Mahato J, Panigrahi R, Navalkar A, Mehra S, et al. (2020) α-Synuclein aggregation nucleates through liquid–liquid phase separation. Nat Chem 12:705–716.

194. Aguzzi A, Altmeyer M (2016) Phase Separation: Linking Cellular Compartmentalization to Disease. Trends Cell Biol 26:547–558.

195. Mathieu C, Pappu R V., Paul Taylor J (2020) Beyond aggregation: Pathological phase transitions in neurodegenerative disease. Science (1979) 370:56–60.

196. Nakashima KK, van Haren MHI, André AAM, Robu I, Spruijt E (2021) Active coacervate droplets are protocells that grow and resist Ostwald ripening. Nat Commun 12.

197. Wang Z, Zhang G, Zhang H (2019) Protocol for analyzing protein liquid–liquid phase separation. Biophys Rep 5:1–9.

198. Sawner AS, Ray S, Yadav P, Mukherjee S, Panigrahi R, Poudyal M, Patel K, Ghosh D, Kummerant E, Kumar A, et al. (2021) Modulating α-Synuclein Liquid-Liquid Phase Separation. Biochemistry 60:3676–3696.

199. Lin Y, Fichou Y, Longhini AP, Llanes LC, Yin P, Bazan GC, Kosik KS, Han S (2021) Liquid-Liquid Phase Separation of Tau Driven by Hydrophobic Interaction Facilitates Fibrillization of Tau. J Mol Biol 433:166731.

200. Mohammadi P, Christopher J, Beaune G, Engelhardt P, Kamada A, Timonen JVI, Knowles TPJ, Penttila M, Linder MB (2020) Controllable coacervation of recombinantly produced spider silk protein using kosmotropic salts. J Colloid Interface Sci 560:149–160.

201. Hagemann M (2011) Molecular biology of cyanobacterial salt acclimation. FEMS Microbiol Rev 35:87–123.

202. André AAM, Yewdall NA, Spruijt E (2023) Crowding-induced phase separation and gelling by co-condensation of PEG in NPM1-rRNA condensates. Biophys J 122:397–407.

203. Rayman JB, Karl KA, Kandel ER (2018) TIA-1 Self-Multimerization, Phase Separation, and Recruitment into Stress Granules Are Dynamically Regulated by Zn 2+. Cell Rep 22:59–71.

204. Marianelli AM, Miller BM, Keating CD (2018) Impact of macromolecular crowding on RNA/spermine complex coacervation and oligonucleotide compartmentalization. Soft Matter 14:368–378.

205. Yamashita T, Voth GA (2010) Properties of hydrated excess protons near phospholipid bilayers. Journal of Physical Chemistry B 114:592–603.

206. Naskar S, Merino A, Espadas J, Singh J, Roux A, Colom A, Low HH (2023) Mechanism for Vipp1 spiral formation , ring biogenesis and membrane repair.

207. Mullineaux CW (2014) Co-existence of photosynthetic and respiratory activities in cyanobacterial thylakoid membranes. Biochim Biophys Acta Bioenerg 1837:503–511.

208. Jackson PJ, Hitchcock A, Brindley AA, Dickman MJ, Hunter CN (2023) Absolute quantification of cellular levels of photosynthesis-related proteins in Synechocystis sp. PCC 6803. Photosynth Res 155:219–245.

209. Zhang L, Kato Y, Otters S, Vothknecht UC, Sakamoto W (2012) Essential Role of VIPP1 in Chloroplast Envelope Maintenance in Arabidopsis. Plant Cell 24:3695–3707.

210. Adell MAY, Migliano SM, Upadhyayula S, Bykov YS, Sprenger S, Pakdel M, Vogel GF, Jih G, Skillern W, Behrouzi R, et al. (2017) Recruitment dynamics of ESCRT-III and Vps4 to endosomes and implications for reverse membrane budding. Elife 6:1–27.

211. Hurley JH, Yang D (2008) MIT Domainia. Dev Cell 14:6–8.

212. Han H, Monroe N, Votteler J, Shakya B, Sundquist WI, Hill CP (2015) Binding of substrates to the central pore of the Vps4 ATPase is autoinhibited by the Microtubule Interacting and Trafficking (MIT) domain and activated by MIT Interacting Motifs (MIMs). Journal of Biological Chemistry 290:13490–13499.

213. Wenzel DM, Mackay DR, Skalicky JJ, Paine EL, Miller MS, Ullman KS, Sundquist WI (2022) Comprehensive analysis of the human ESCRT-III-MIT domain interactome reveals new cofactors for cytokinetic abscission. Elife 11:1–36.

214. Obita T, Saksena S, Ghazi-Tabatabai S, Gill DJ, Perisic O, Emr SD, Williams RL (2007) Structural basis for selective recognition of ESCRT-III by the AAA ATPase Vps4. Nature 449:735–739.

215. Carroni M, Kummer E, Oguchi Y, Wendler P, Clare DK, Sinning I, Kopp J, Mogk A, Bukau B, Saibil HR (2014) Head-to-tail interactions of the coiled-coil domains regulate ClpB activity and cooperation with Hsp70 in protein disaggregation. Elife 2014:1–22.

216. Oguchi Y, Kummer E, Seyffer F, Berynskyy M, Anstett B, Zahn R, Wade RC, Mogk A, Bukau B (2012) A tightly regulated molecular toggle controls AAA+ disaggregase. Nat Struct Mol Biol 19:1338–1346.

217. Schirmer EC, Homann OR, Kowal AS, Lindquist S (2004) Dominant Gain-of-Function Mutations in Hsp104p Reveal Crucial Roles for the Middle Region. Mol Biol Cell 15:2061–2072.

218. Ohnishi N, Zhang L, Sakamoto W (2018) VIPP1 Involved in Chloroplast Membrane Integrity Has GTPase Activity in Vitro. Plant Physiol 177:328–338.

219. Junglas B, Siebenaller C, Schlösser L, Hellmann N, Schneider D (2020) GTP hydrolysis by Synechocystis IM30 does not decisively affect its membrane remodeling activity. Sci Rep 10:9793.

220. Moore LR, Caspi R, Campbell DA, Casey JR, Crevecoeur S, Lea-Smith DJ, Long B, Omar NM, Paley SM, Schmelling NM, et al. (2024) CyanoCyc cyanobacterial web portal. Front Microbiol 15.

221. Glover JR, Lindquist S (1998) Hsp104, Hsp70, and Hsp40: A novel chaperone system that rescues previously aggregated proteins. Cell 94:73–82.

222. Hayashi S, Nakazaki Y, Kagii K, Imamura H, Watanabe YH (2017) Fusion protein analysis reveals the precise regulation between Hsp70 and Hsp100 during protein disaggregation. Sci Rep 7:1–14.

223. Bouchnak I, van Wijk KJ (2021) Structure, function, and substrates of Clp AAA+ protease systems in cyanobacteria, plastids, and apicoplasts: A comparative analysis. Journal of Biological Chemistry 296:100338.

224. Gao F, Wang W, Zhang W, Liu C (2015) α-Helical Domains Affecting the Oligomerization of Vipp1 and Its Interaction with Hsp70/DnaK in Chlamydomonas. Biochemistry 54:4877–4889.

225. Kudryashev M, Wang RYR, Brackmann M, Scherer S, Maier T, Baker D, Dimaio F, Stahlberg H, Egelman EH, Basler M (2015) Structure of the Type VI secretion system contractile sheath. Cell 160:952–962.

226. Pietrosiuk A, Lenherr ED, Falk S, Bönemann G, Kopp J, Zentgraf H, Sinning I, Mogk A (2011) Molecular basis for the unique role of the AAA + chaperone ClpV in type VI protein secretion. Journal of Biological Chemistry 286:30010–30021.

227. Seyffer F, Kummer E, Oguchi Y, Winkler J, Kumar M, Zahn R, Sourjik V, Bukau B, Mogk A (2012) Hsp70 proteins bind Hsp100 regulatory M domains to activate AAA+ disaggregase at aggregate surfaces. Nat Struct Mol Biol 19:1347–1355.

228. Watanabe K, Morishita K, Zhou X, Shiizaki S, Uchiyama Y, Koike M, Naguro I, Ichijo H (2021) Cells recognize osmotic stress through liquid–liquid phase separation lubricated with poly(ADP-ribose). Nat Commun 12.

229. Gu J, Liu Z, Zhang S, Li Y, Xia W, Wang C, Xiang H, Liu Z, Tan L, Fang Y, et al. (2020) Hsp40 proteins phase separate to chaperone the assembly and maintenance of membraneless organelles. Proc Natl Acad Sci U S A 117:31123–31133.

230. Zhang H, Shao S, Zeng Y, Wang X, Qin Y, Ren Q, Xiang S, Wang Y, Xiao J, Sun Y (2022) Reversible phase separation of HSF1 is required for an acute transcriptional response during heat shock. Nat Cell Biol 24:340–352.

231. Söding J, Zwicker D, Sohrabi-Jahromi S, Boehning M, Kirschbaum J (2020) Mechanisms for Active Regulation of Biomolecular Condensates. Trends Cell Biol 30:4–14.

232. Kusumaatmaja H, May AI, Knorr RL (2021) Intracellular wetting mediates contacts between liquid compartments and membrane-bound organelles. Journal of Cell Biology 220:1–10.

233. Kusumaatmaja H, May AI, Feeney M, McKenna JF, Mizushima N, Frigerio L, Knorr RL (2021) Wetting of phase-separated droplets on plant vacuole membranes leads to a competition between tonoplast budding and nanotube formation. Proc Natl Acad Sci U S A 118:3–5.

234. Mangiarotti A, Chen N, Zhao Z, Lipowsky R, Dimova R (2023) Wetting and complex remodeling of membranes by biomolecular condensates. Nat Commun 14:1–15.

235. Bussi C, Mangiarotti A, Vanhille-Campos C, Aylan B, Pellegrino E, Athanasiadi N, Fearns A, Rodgers A, Franzmann TM, Šarić A, et al. (2023) Stress granules plug and stabilize damaged endolysosomal membranes. Nature 623:1062–1069.

236. Skowyra ML, Schlesinger PH, Naismith T V., Hanson PI (2018) Triggered recruitment of ESCRT machinery promotes endolysosomal repair. Science (1979) 360.

237. Radulovic M, Schink KO, Wenzel EM, Nähse V, Bongiovanni A, Lafont F, Stenmark H (2018) ESCRT -mediated lysosome repair precedes lysophagy and promotes cell survival . EMBO J 37.

238. Qamar S, Wang G, Randle SJ, Ruggeri FS, Varela JA, Lin JQ, Phillips EC, Miyashita A, Williams D, Ströhl F, et al. (2018) FUS Phase Separation Is Modulated by a Molecular Chaperone and Methylation of Arginine Cation-π Interactions. Cell 173:720-734.e15.

239. Li J, Zhang M, Ma W, Yang B, Lu H, Zhou F, Zhang L (2022) Post-translational modifications in liquid-liquid phase separation: a comprehensive review. Molecular Biomedicine 3.

240. Elias RD, Zhu Y, Su Q, Ghirlando R, Zhang J, Deshmukh L (2023) Reversible phase separation of ESCRT protein ALIX through tyrosine phosphorylation. Sci Adv 9.

241. Forchhammer K, Schwarz R (2019) Nitrogen chlorosis in unicellular cyanobacteria – a developmental program for surviving nitrogen deprivation. Environ Microbiol 21:1173–1184.

242. Spät P, Klotz A, Rexroth S, Maček B, Forchhammer K (2018) Chlorosis as a Developmental Program in Cyanobacteria: The Proteomic Fundament for Survival and Awakening. Molecular & Cellular Proteomics 17:1650–1669.

243. Junglas B, Schneider D (2018) What is Vipp1 good for? Mol Microbiol 108:1–5.

244. Ramirez DA, Hough LE, Shirts MR (2024) Coiled-coil domains are sufficient to drive liquid-liquid phase separation in protein models. Biophys J 123:703–717.

245. Kroschwald S, Maharana S, Simon A (2017) Hexanediol: a chemical probe to investigate the material properties of membrane-less compartments. Matters (Zur).

246. Cashikar AG, Shim S, Roth R, Maldazys MR, Heuser JE, Hanson PI (2014) Structure of cellular ESCRT-III spirals and their relationship to HIV budding. Elife 3:1–17.

247. Dignon GL, Best RB, Mittal J (2020) Biomolecular Phase Separation: From Molecular Driving Forces to Macroscopic Properties. Annu Rev Phys Chem 71:53–75.

248. Lindsay RJ, Mansbach RA, Gnanakaran S, Shen T (2021) Effects of pH on an IDP conformational ensemble explored by molecular dynamics simulation. Biophys Chem 271:106552.

249. Last MGF, Deshpande S, Dekker C (2020) pH-Controlled Coacervate-Membrane Interactions within Liposomes. ACS Nano 14:4487–4498.

250. Dogra P, Joshi A, Majumdar A, Mukhopadhyay S (2019) Intermolecular Charge-Transfer Modulates Liquid-Liquid Phase Separation and Liquid-to-Solid Maturation of an Intrinsically Disordered pH-Responsive Domain. J Am Chem Soc 141:20380–20389.

251. Munder MC, Midtvedt D, Franzmann T, Nüske E, Otto O, Herbig M, Ulbricht E, Müller P, Taubenberger A, Maharana S, et al. (2016) A pH-driven transition of the cytoplasm from a fluid- to a solid-like state promotes entry into dormancy. Elife 5:1–30.

252. King MR, Ruff KM, Lin AZ, Pant A, Farag M, Lalmansingh JM, Wu T, Fossat MJ, Ouyang W, Lew MD, et al. (2024) Macromolecular condensation organizes nucleolar sub-phases to set up a pH gradient. Cell 187:1889-1906.e24.

253. Kumar Patel C, Singh S, Saini B, Kanti Mukherjee T (2022) Macromolecular Crowding-Induced Unusual Liquid−Liquid Phase Separation of Human Serum Albumin via Soft Protein−Protein Interactions. J. Phys. Chem. Lett 13:3636–3644.

254. Sołtys K, Wycisk K, Ożyhar A (2021) Liquid-liquid phase separation of the intrinsically disordered AB region of hRXRγ is driven by hydrophobic interactions. Int J Biol Macromol 183:936–949.

255. Tsoi PS, Quan MD, Choi K, Dao KM, Ferreon JC, Ferreon ACM (2021) Electrostatic modulation of hnRNPA1 low-complexity domain liquid–liquid phase separation and aggregation. Protein Science 30:1408–1417.

256. Lin Y, Fichou Y, Zeng Z, Hu NY, Han S (2020) Electrostatically Driven Complex Coacervation and Amyloid Aggregation of Tau Are Independent Processes with Overlapping Conditions. ACS Chem Neurosci 11:615–627.

257. Düster R, Kaltheuner IH, Schmitz M, Geyer M (2021) 1,6-Hexanediol, commonly used to dissolve liquid-liquid phase separated condensates, directly impairs kinase and phosphatase activities. Journal of Biological Chemistry 296:100260.

258. Kozak M, Kaksonen M (2022) Condensation of Ede1 promotes the initiation of endocytosis. Elife 11:1–25.

259. Paladino A, Vitagliano L, Graziano G (2023) The Action of Chemical Denaturants: From Globular to Intrinsically Disordered Proteins. Biology (Basel) 12.

260. Liu J, Shim YY, Reaney MJT (2020) Ionic strength and hydrogen bonding effects on whey protein isolate–flaxseed gum coacervate rheology. Food Sci Nutr 8:2102–2111.

261. Babst M, Katzmann DJ, Estepa-Sabal EJ, Meerloo T, Emr SD ESCRT-III: An Endosome-Associated Heterooligomeric Protein Complex Required for MVB Sorting. 2002.

262. Shim S, Kimpler LA, Hanson PI (2007) Structure/Function Analysis of Four Core ESCRT-III Proteins Reveals Common Regulatory Role for Extreme C-Terminal Domain. Traffic 8:1068–1079.

263. Srivastava R, Pisareva T, Norling B (2005) Proteomic studies of the thylakoid membrane of Synechocystis sp. PCC 6803. Proteomics 5:4905–4916.

264. Srivastava R, Battchikova N, Norling B, Aro EM (2006) Plasma membrane of Synechocystis PCC 6803: A heterogeneous distribution of membrane proteins. Arch Microbiol 185:238–243.

265. Chiaruttini N, Redondo-Morata L, Colom A, Humbert F, Lenz M, Scheuring S, Roux A (2015) Relaxation of Loaded ESCRT-III Spiral Springs Drives Membrane Deformation. Cell 163:866–879.

266. Jukic N, Perrino AP, Humbert F, Roux A, Scheuring S (2022) Snf7 spirals sense and alter membrane curvature. Nat Commun 13.

267. Hanson PI, Roth R, Lin Y, Heuser JE (2008) Plasma membrane deformation by circular arrays of ESCRT-III protein filaments. Journal of Cell Biology 180:389–402.

268. Yilmazer I, Vetrano P, Eicke S, Abt MR, Traverso E A conserved ESCRT-II-like protein participates in the biogenesis and maintenance of thylakoid membranes. 2023.

269. Sayers EW, Bolton EE, Brister JR, Canese K, Chan J, Comeau DC, Connor R, Funk K, Kelly C, Kim S, et al. (2022) Database resources of the national center for biotechnology information. Nucleic Acids Res 50:D20–D26.

270. The UniProt Consortium (2023) UniProt: the Universal Protein Knowledgebase in 2023. Nucleic Acids Res. 51:D523–D531 (2023). 51:523–531.

271. Yan Y, Huang SY (2021) Accurate prediction of inter-protein residue-residue contacts for homo-oligomeric protein complexes. Brief Bioinform 22:1–13.

272. Mirdita M, Schütze K, Moriwaki Y, Heo L, Ovchinnikov S, Steinegger M (2022) ColabFold: making protein folding accessible to all. Nat Methods 19:679–682.

273. Banjade S, Rosen MK (2014) Phase transitions of multivalent proteins can promote clustering of membrane receptors. Elife 3:1–24.

274. Babl L, Merino-Salomón A, Kanwa N, Schwille P (2022) Membrane mediated phase separation of the bacterial nucleoid occlusion protein Noc. Sci Rep 12:1–12.

275. Li P, Banjade S, Cheng HC, Kim S, Chen B, Guo L, Llaguno M, Hollingsworth J V., King DS, Banani SF, et al. (2012) Phase transitions in the assembly of multivalent signalling proteins. Nature 483:336–340.

276. Ladbury JE, Lin CC, Suen KM (2023) Phase separation enhances probability of receptor signalling and drug targeting. Trends Biochem Sci 48:428–436.

277. Allen L, Scott J, Brand A, Hlava M, Altman M (2014) Publishing: Credit where credit is due. Nature 508:312–313.

278. Glaser F, Pupko T, Paz I, Bell RE, Bechor-Shental D, Martz E, Ben-Tal N (2003) ConSurf: Identification of Functional Regions in Proteins by Surface-Mapping of Phylogenetic Information. Bioinformatics 19:163–164.

5. Abbreviations

%	percent
°C	degree celsius
µL	microliter
µM	micromolar
R	resistance
E. coli	*Escherichia coli*
Synechocystis	*Synechocystis sp. PCC 6803*
ADP	adenosine diphosphate
ATP	adenosine triphosphate
Amp	ampicillin
BSA	bovine serum albumin
CBB	Calvin–Benson–Bassham
CD	circular dichroism
CEF	cyclic electron flow
Cyt b_6f	cytochrome b_6f
Cyt c_6	cytochrome c_6
DMSO	dimethyl sulfoxide
DNA	deoxyribonucleic acid
DOPC	1,2-dioleoyl-sn-glycero-3-phosphocholine
DOPG	1,2-dioleoyl-sn-glycero-3- phosphoglycerol)
DTT	dithiothreitol
EDTA	ethylenediaminetetraacetic acid, disodium salt
g	gram
HEPES	4-(2-hydroxyethyl)-1-piperazineethanesulfonic acid
His-Tag	histidine tag
Kan	kanamycin

kDa	kilo dalton
L	liter
LB	lysogeny broth
mL	mililiter
mVenus	monomeric venus
NADH	nicotinamide adenine dinucleotide hydrogen
NADPH	nicotinamide adenine dinucleotide phosphate hydrogen
NDH-1	type I NADPH-plastoquinone oxidoreductase
Ni-NTA	nickel nitriloacetic acid
ns	nanoseconds
OD	optical density
PCR	polymerase chain reaction
PMF	proton motive force
PDB	protein data bank
PQ	plastoquinone
PQH2	plastoquinol
PSI	photosystem I
PSII	photosystem II
RNA	Ribonucleic acid
rpm	revolutions per minute
RuBisCO	ribulose-1,5-bisphosphate carboxylase
SD	standard deviation
SDS	sodium dodecyl sulphate
SDS-PAGE	sodium dodecyl sulphate-polyacrylamide gel electrophoresis
TAE	Tris acetate EDTA
TEMED	tetramethylethylenediamine
TM	thylakoid membrane
Tris	Tris(hydroxymethyl)aminoethane
wt	wild type

6. List of figures

7. List of tables

8. Appendix

8.1 Appendix to section 3.1

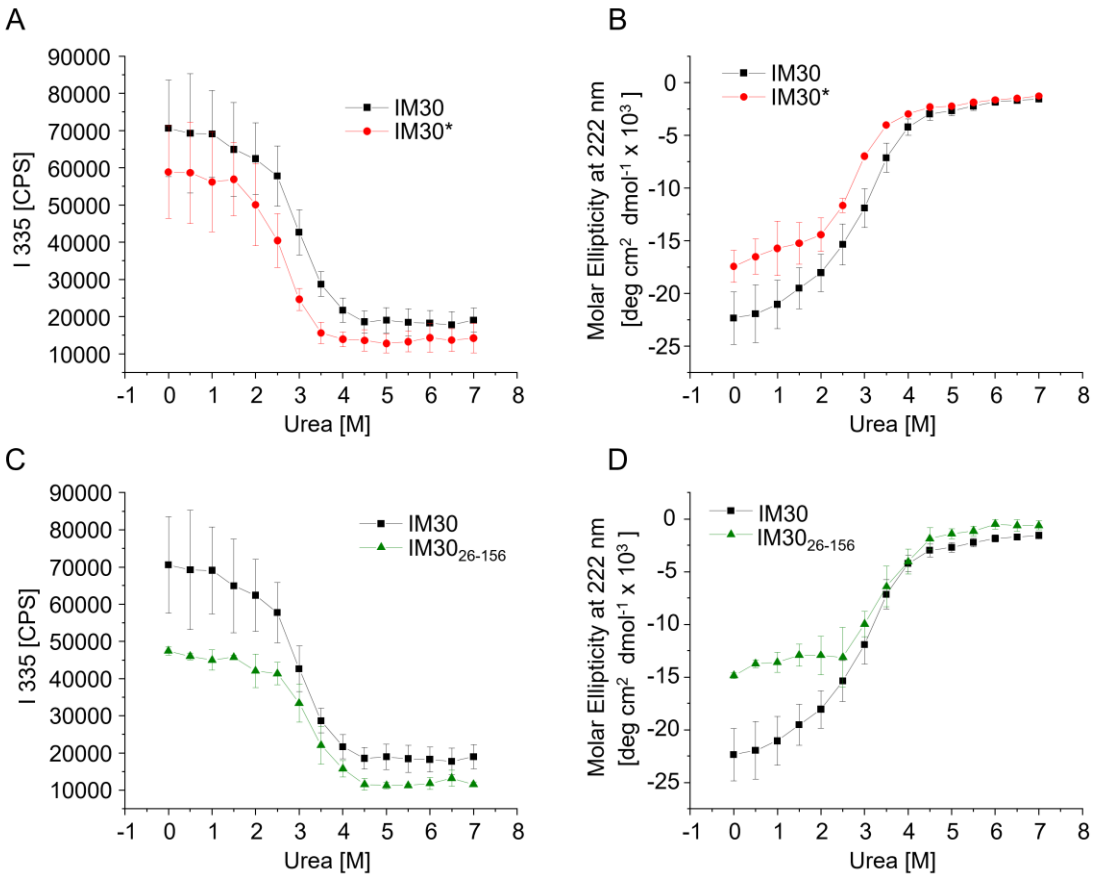

Supplementary figure 8.1-1*: Trp fluorescence intensity and CD signal at 222 nm at increasing urea concentrations. (A) Trp fluorescence intensity and (B) CD signal at 222 nm of IM30 and IM30*. (C) Trp fluorescence intensity and (D) CD signal at 222 nm of IM30 and IM30$_{26\text{-}156}$. The error bars represent SD, n=3.Note: In case of IM30 the disordered regions contribute only little to the total protein structure whereas the much shorter construct of IM30$_{26\text{-}156}$ has much higher portion of flexible regions (~33%) at 0 M urea compared to IM30. Therefore, the molar ellipticity for the latter seems much lower compared to IM30.*

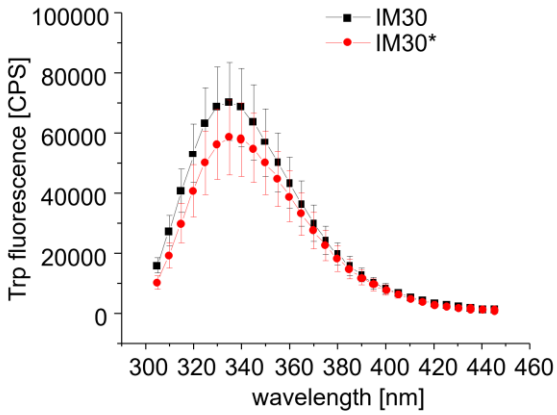

***Supplementary figure 8.1-2**:Trp fluorescence spectrum of IM30. Trp fluorescence spectrum of (A) IM30 and (B) IM30* at 0 M urea; The error bars represent SD, n=3*

***Suppl. table 8.1-1**: R-values and parameters parameter of global fits used in this study. Parameters a and b are not applicable for the fits of IM30* and $IM30_{26-156}$.*

	IM30wt	IM30wt (b=0)	IM30*	$IM30_{26-156}$
R^2	0.998	0.997	0.998	0.995
a	0.75±0.08	0.93±0.8	-	-
b	0.19±0.6	0	-	-
c_{50}	3.0±0.1	2.7±0.7	2.65±0.03	3.1±0.1
d	0.53±0.04	0.62±0.03	0.45±0.02	0.62±0.05

Author contributions according to CRediT - Contributor Roles Taxonomy[277]

Ndjali Quarta: Conceptualization, Data Curation, Formal Analysis, Investigation (protein preparations and analyses), Methodology, Software, Validation, Visualization, Writing – Original Draft, Writing – Review & Editing. [redacted] Investigation (MD simulations), Data Curation, Formal Analysis, Software, Validation, Visualization, Writing – Original Draft. [redacted]**:** Conceptualization (MD simulations), Data Curation, Formal Analysis, Funding Acquisition, Methodology, Project Administration, Resources, Software, Supervision, Validation, Writing – Original Draft. [redacted] Data Curation, Investigation (kinetic analyses and model development), Software, Validation, Visualization, Writing – Original Draft, Writing – Review & Editing. [redacted]**:** Conceptualization, Formal Analysis, Methodology, Funding Acquisition, Project Administration, Resources, Supervision, Writing – Original Draft, Writing – Review & Editing.

8.2 Appendix to section 3.2

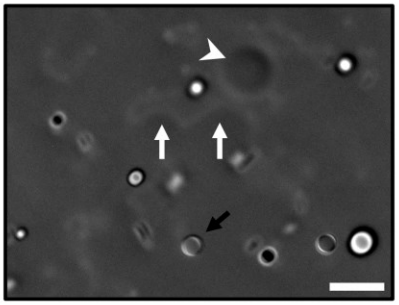

Supplementary figure 8.2-1*: Wetting of pH induced condensates on glass surface. Exemplary DIC image of 32 µM IM30*, 10 mM HEPES, 10 mM Phosphate buffer at pH 5.5 after prolonged incubation time showing wetting of bottom glass surface by IM30* condensates. White arrowhead indicates a condensate that recently attached to the glass slide and wetted the surface; white arrows indicate the edge of the extended area of already fused condensates; black arrow indicates unfused condensate sitting in solution near the glass surface.*

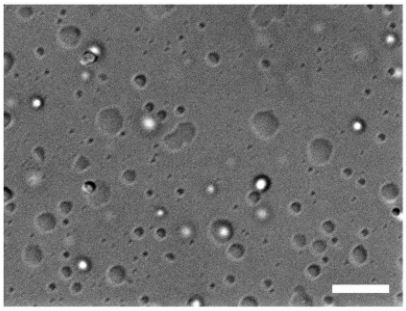

Supplementary figure 8.2-2*: Wetting of PEG/NaCl induced condensates on glass surface. Exemplary DIC image of 32 µM IM30*, 10 mM HEPES, 10 mM Phosphate buffer at pH 5.5 after prolonged incubation time showing wetting of bottom glass surface by IM30* condensates. White arrowhead indicates a condensate that recently attached to the glass slide and wetted the surface; white arrows indicate the edge of the extended area of already fused condensates; black arrow indicates unfused condensate sitting in solution near the glass surface.*

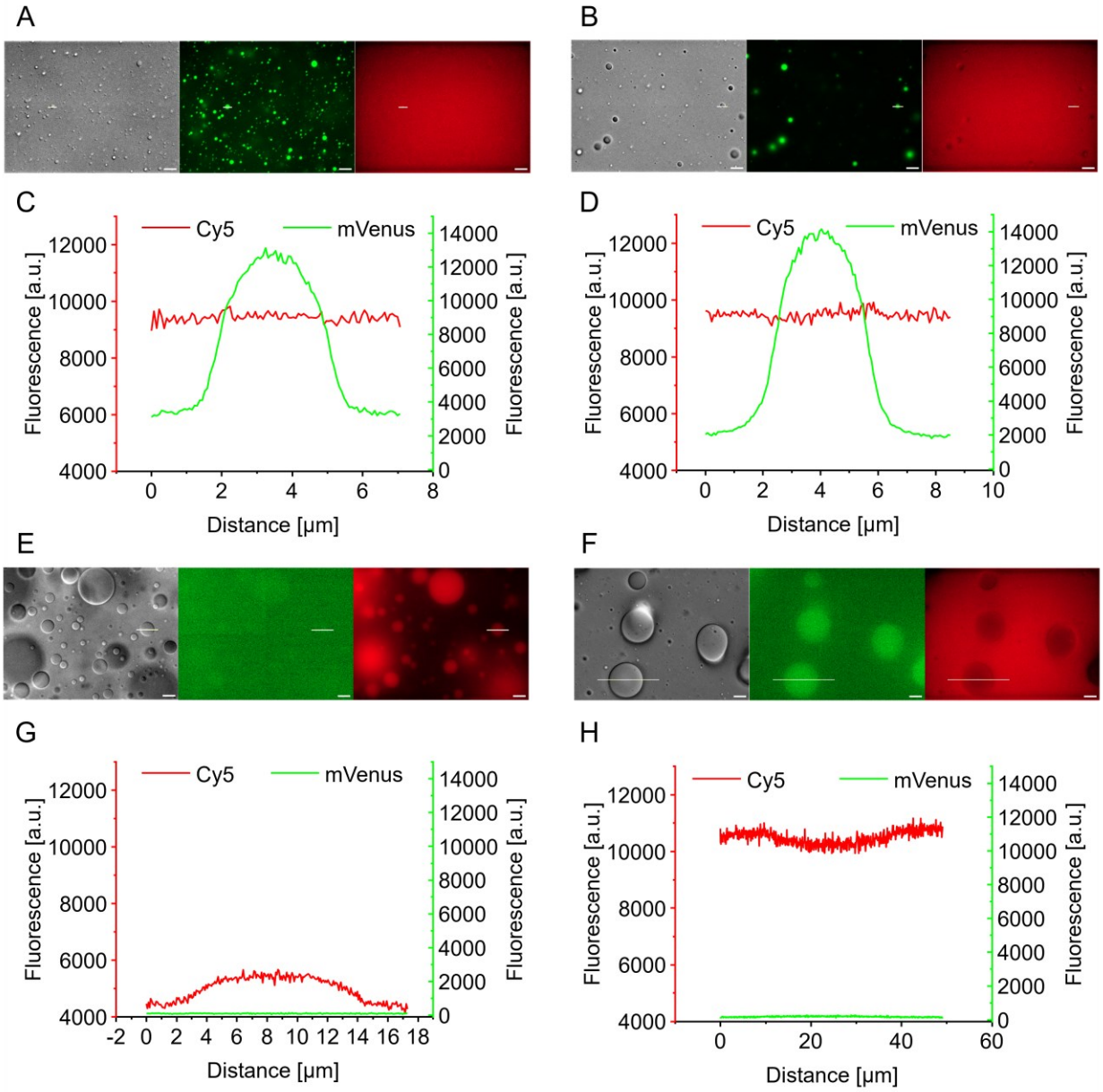

***Supplementary figure 8.2-3**: Fluorescence microscopy of IM30* condensates with fluorescently labeled crowding agent. (A, C) 32 µM IM30*, 10 mol% 7GS-mVenus, 10% PEG, 1 mol% Cy5-PEG, 100 mM NaCl and 20 mM HEPES at pH 7.6; (B, D) pH 5.5 induced condensates in presence of 10% PEG, 1 mol% Cy5-PEG; (E, G) PEG dextran condensates and (F, H) PEG BSA condensates each with same total concentration of Cy5-PEG as in (A) and (B); (A, B, E, F) DIC image (left); mVenus channel (middle) and Cy5 channel (right) and corresponding line profile (C, D, G, H) of fluorescence signal for a line through the area that is indicated by a white thin line in the corresponding images; exemplary images and line profile are shown for a set of n=3 experiments; scale bar 10 µm.*

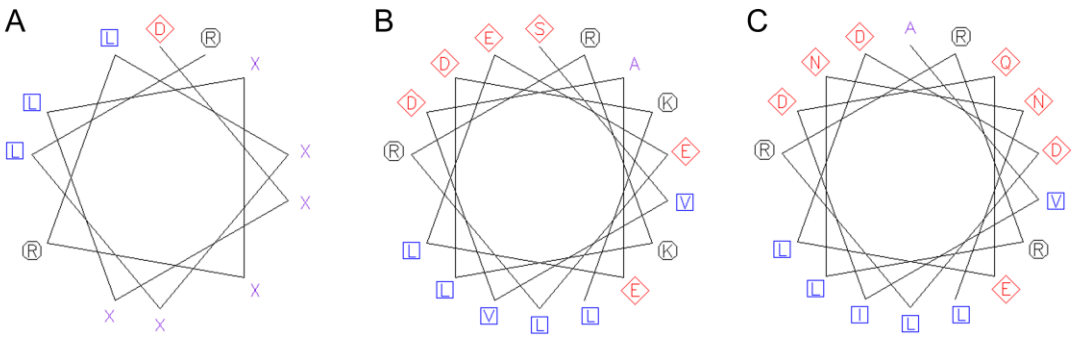

***Supplementary figure 8.2-4**: Comparison of helical wheel projections showing similarities in their amphipathic pattern. Helical wheel projection for C-terminal region of a MIM consensus sequence from ESCRT-III [214] (A) and corresponding consensus sequence in IM30 [127] (B) and the corresponding sequence of SynIM30.*

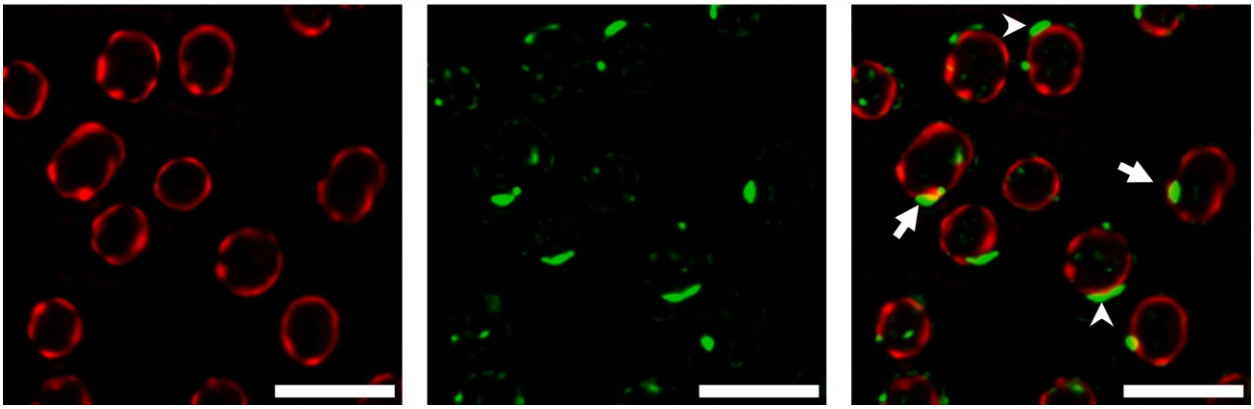

***Supplementary figure 8.2-5**: Fluorescence microscopy images showing patchy sheet like punctae for of Synechocystis cells expressing mVenus-tagged IM30. Shown are the thylakoid channel in red (left), mVenus channel in green (middle) and an overlay of both channels (right) of structured illumination evaluated images (SIM² strong). White arrows mark punctae, white arrowhead indicates patches and sheet-like protein localization near the plasma membrane. The scale bar is 3 µm. All in vivo fluorescence microscopy experiments were conceived and performed in collaboration with [redacted] and [redacted] niversity of Liverpool, UK).*

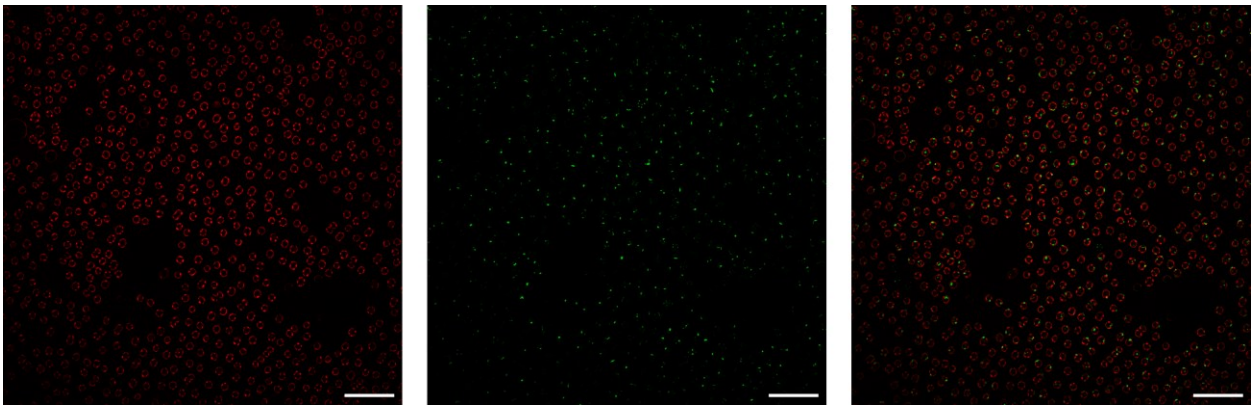

Supplementary figure 8.2-6*: Uncropped fluorescence microscopy images of Synechocystis cells expressing mVenus-tagged IM30. Shown are the thylakoid channel in red (left), mVenus channel in green (middle) and an overlay of both channels (right) of structured illumination evaluated images (SIM² strong). The scale bar is 10 µm. All in vivo fluorescence microscopy experiments were conceived and performed in collaboration with [redacted] and [redacted] (University of Liverpool, UK).*

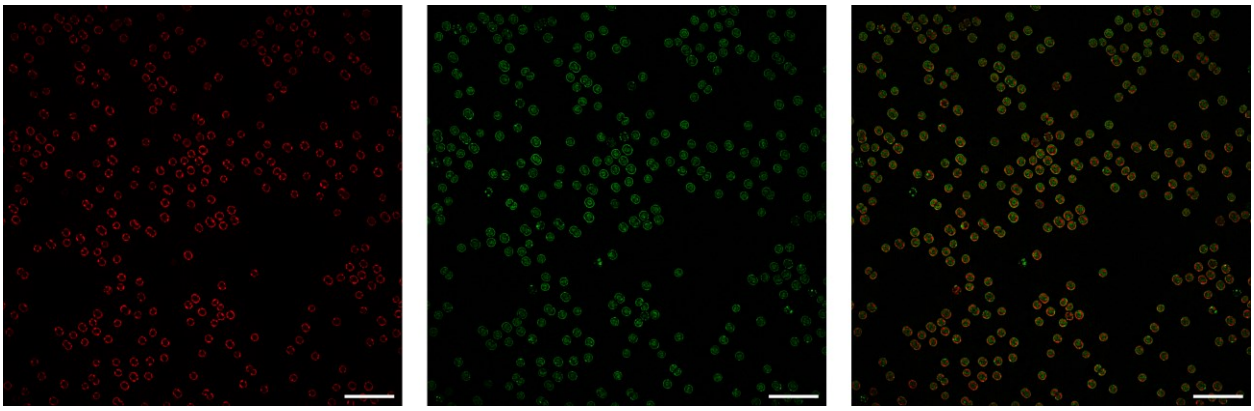

Supplementary figure 8.2-7*: Uncropped fluorescence microscopy images of Synechocystis cells expressing mVenus-tagged IM30*. Shown are the thylakoid channel in red (left), mVenus channel in green (middle) and an overlay of both channels (right) of structured illumination evaluated images (SIM² strong). The scale bar is 10 µm. All in vivo fluorescence microscopy experiments were conceived and performed in collaboration with [redacted] and [redacted] (University of Liverpool, UK).*

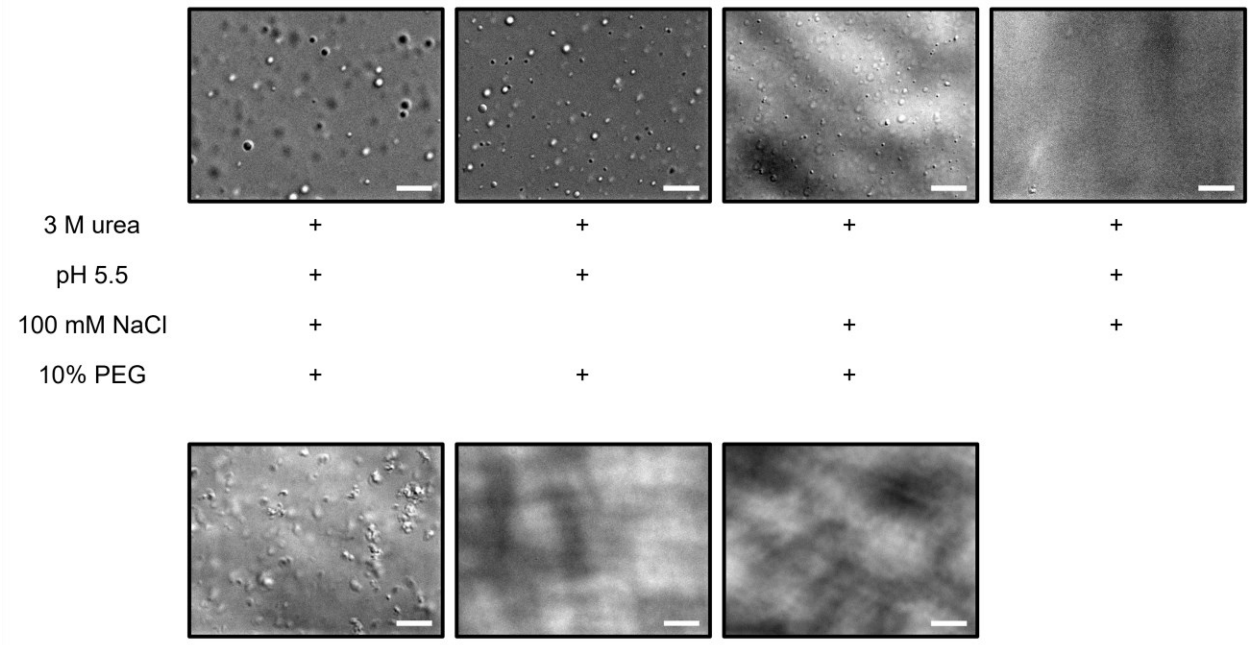

Supplementary figure 8.2-8*: Summary of DIC images of IM30 at varying conditions with urea. Experiments were performed in phase separation buffer and additional changes to the buffer such as 3M instead of 0 M urea, pH 5.5 instead of pH 7.5, 100 mM instead of 0 mM NaCl and 10% instead of 0% PEG are marked in the table below the images with a "+". The scale bar is 10 µm.*

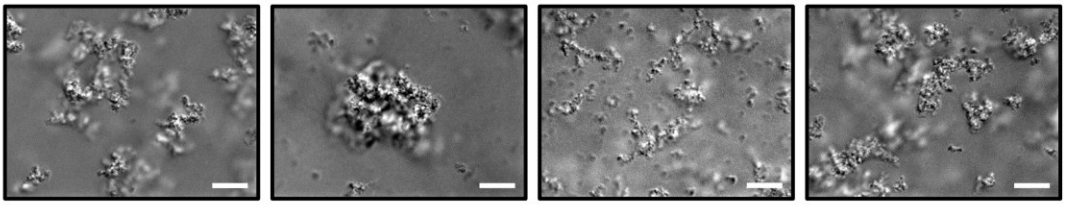

3 M urea				
pH 5.5	+	+		+
100 mM NaCl	+		+	+
10% PEG	+	+	+	

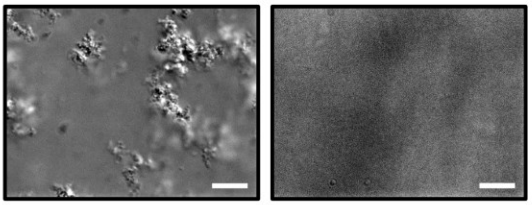

3 M urea	
pH 5.5	+
100 mM NaCl	
10% PEG	

Supplementary figure 8.2-9*: Summary of DIC images of IM30 at varying conditions without urea. Experiments were performed in phase separation buffer and additional changes to the buffer such as 3M instead of 0 M urea, pH 5.5 instead of pH 7.5, 100 mM instead of 0 mM NaCl and 10% instead of 0% PEG are marked in the table below the images with a "+". The scale bar is 10 µm.*

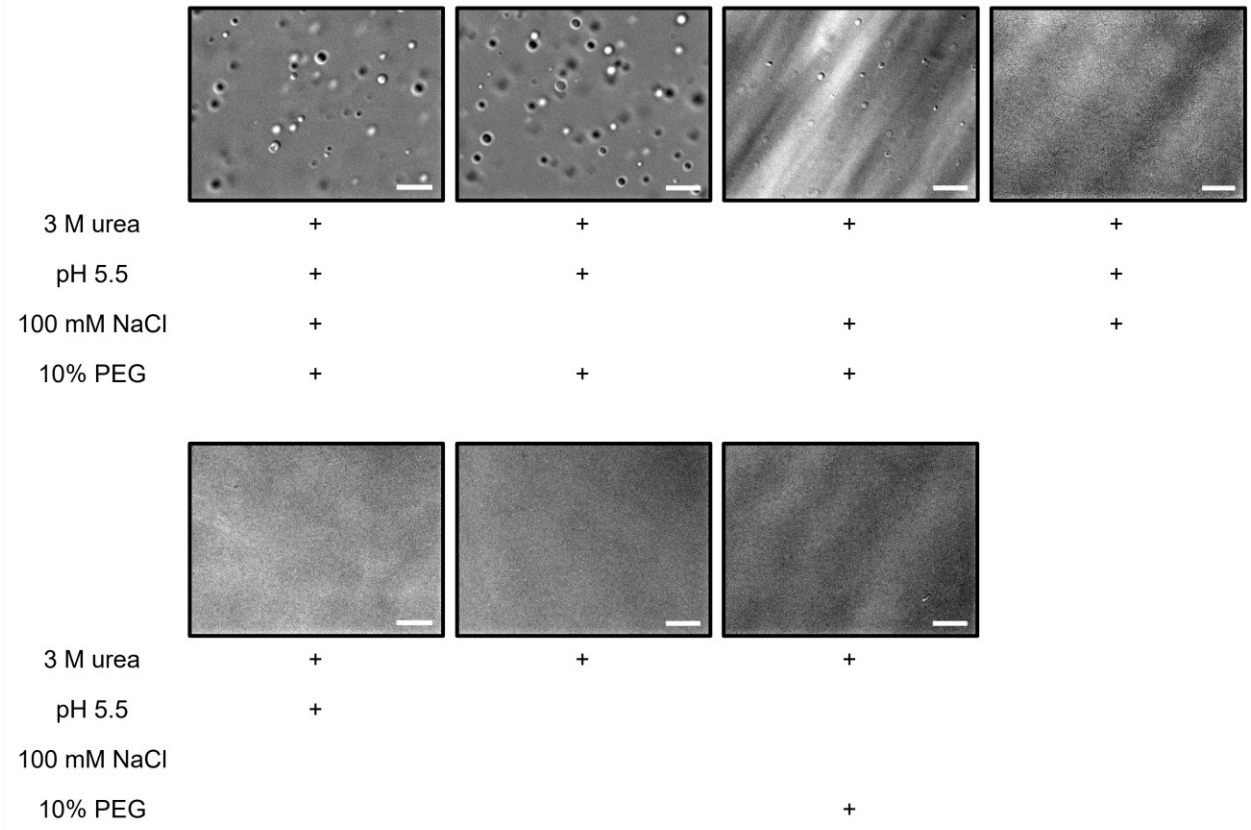

Supplementary figure 8.2-10*: Summary of DIC images of IM30* at varying conditions with urea. Experiments were performed in phase separation buffer and additional changes to the buffer such as 3M instead of 0 M urea, pH 5.5 instead of pH 7.5, 100 mM instead of 0 mM NaCl and 10% instead of 0% PEG are marked in the table below the images with a "+". The scale bar is 10 µm.*

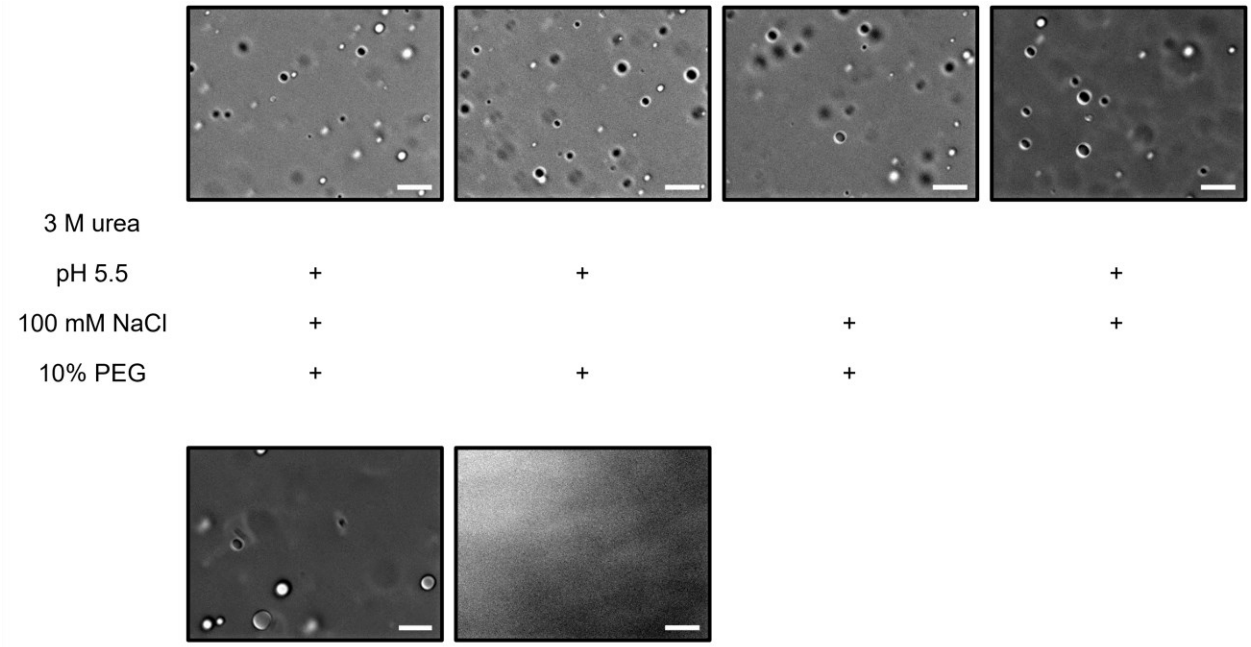

Supplementary figure 8.2-11*: Summary of DIC images of IM30* at varying conditions without urea. Experiments were performed in phase separation buffer and additional changes to the buffer such as 3M instead of 0 M urea, pH 5.5 instead of pH 7.5, 100 mM instead of 0 mM NaCl and 10% instead of 0% PEG are marked in the table below the images with a "+". The scale bar is 10 µm.*

8.3 Appendix to section 3.3

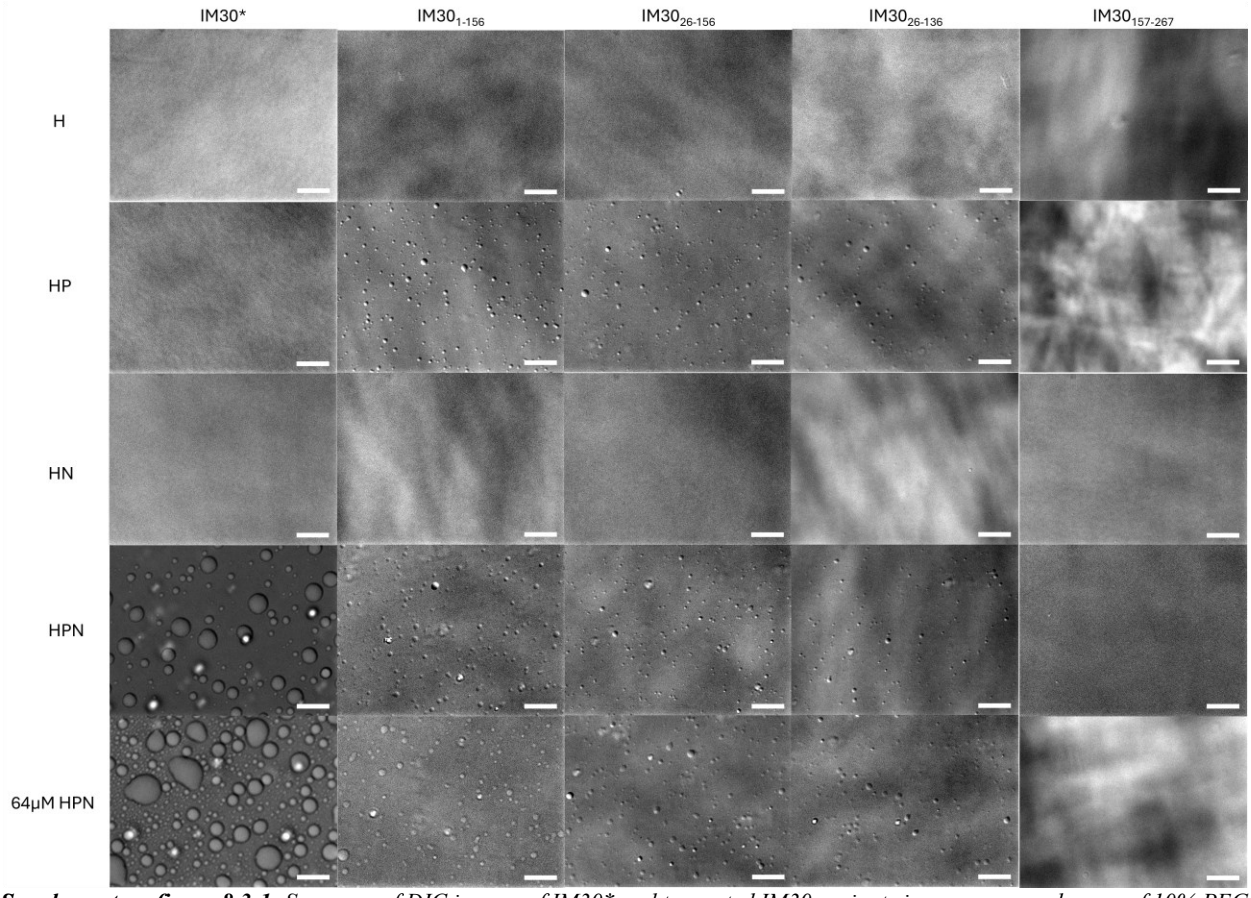

Supplementary figure 8.3-1*: Summary of DIC images of IM30* and truncated IM30 variants in presence or absence of 10% PEG and/or 100 mM NaCl. "H" indicated HEPES buffer, "P" indicates the presence of 10% PEG, "N" indicates the presence of 100 mM NaCl and 32 µM protein were used in all samples except for the last row where 64 µM protein were used.*

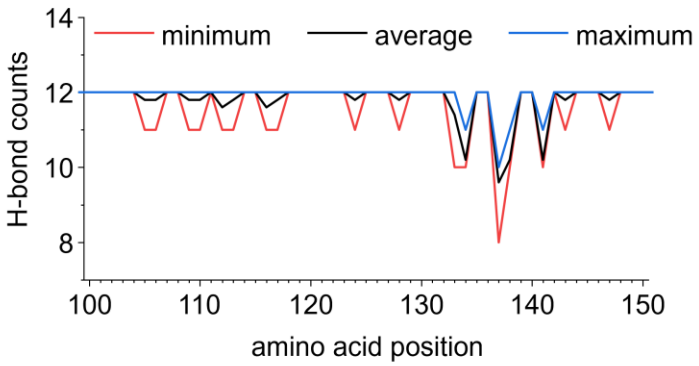

Supplementary figure 8.3-2*: Definition of the beginning of helix α3 in IM30. Number of unique H-bonds between backbone atoms participating in the formation of an alpha helix as determined in ChimeraX and averaged over all available SynIM30 models (PDB:*

7O3W, 7O3x, 7O3Y, 7O3z, 7O40); note that backbone atoms are counted twice resulting in 12 H-bonds for 6 layer and that model 7O3z and 7O40 contain only 6 layers despite the electron density showing 7 layers as outlined in the corresponding publication[96].

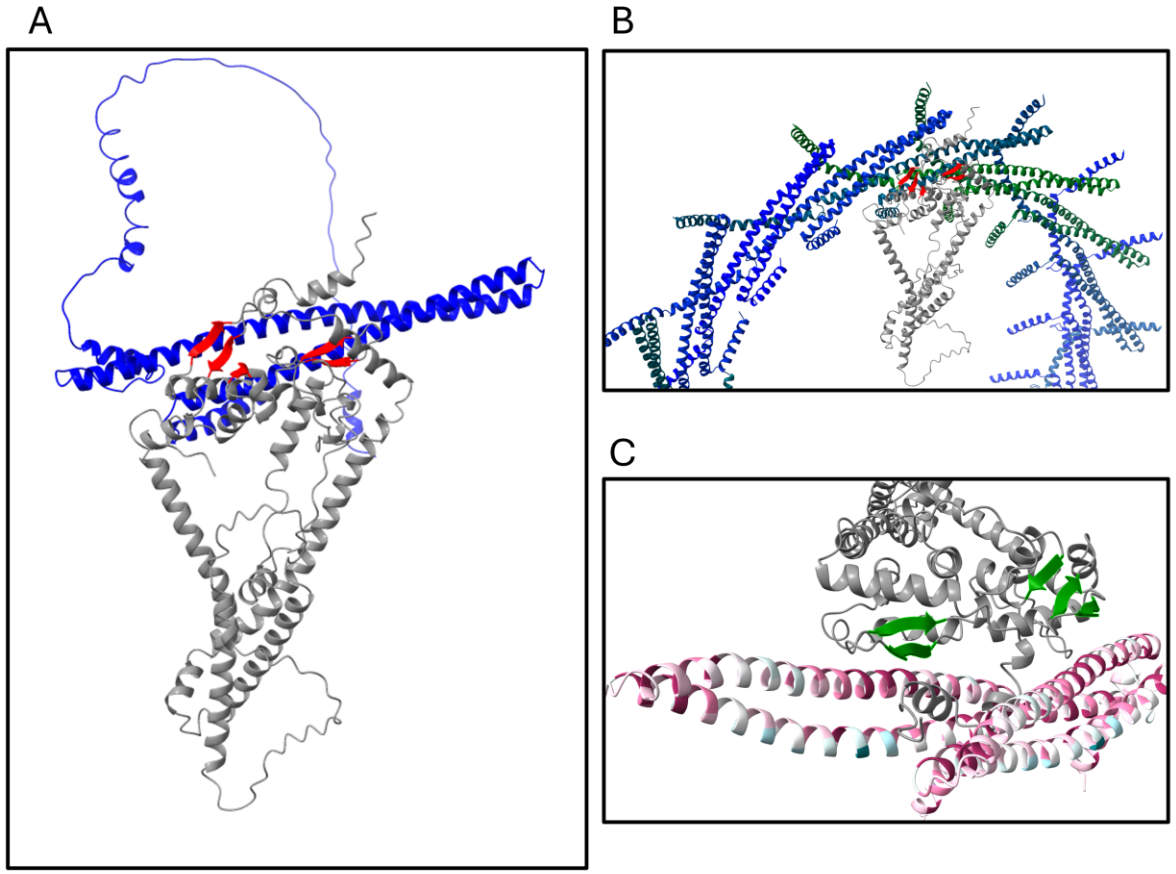

Supplementary figure 8.3-3*: SynVIA1-IM30 complex. SynVIA1-IM30 complex and proximity of winged helix domain of SynVIA1 to conserved residues in neighboring IM30 monomers in the barrel structure. (A) Alphafold2 model of SynVIA1-IM30 complex; (B) IM30 in SynVIA1-IM30 complex replaced by barrel layer (lowest layer of C16 in PDB 7O3Y); (C) Close up view of conserved regions (ConSurf server*[278]*) in IM30 forming a contact site between winged helix domains of VIA1 and helix 1 in the coiled-coil region of IM30.*

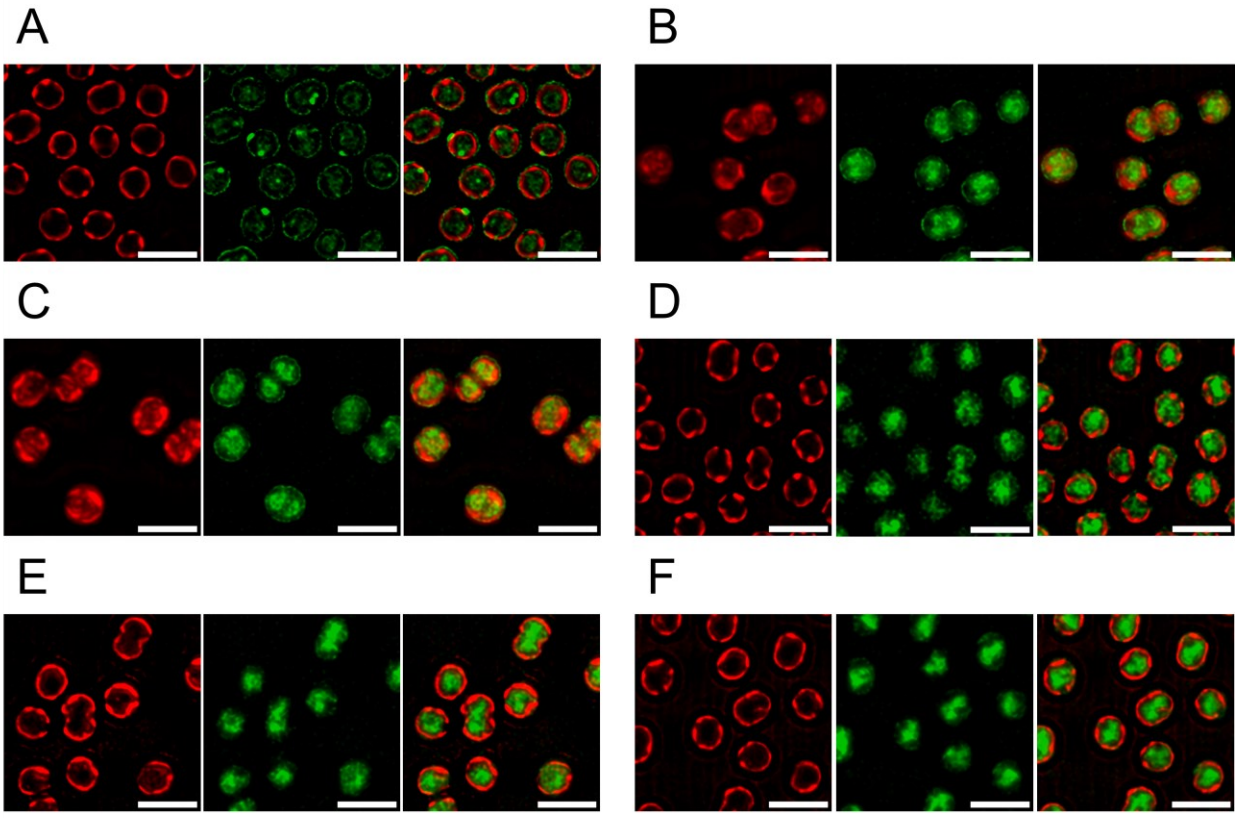

Supplementary figure 8.3-4*: Summary of individual channels for fluorescence microscopy images of Synechocystis cells expressing different IM30 variants tagged with mVenus and mV controls. Shown are the thylakoid channel in red (left), mVenus channel in green (middle) and an overlay of both channels (right) of structured illumination evaluated images (SIM² strong). (A) IM30₁₋₁₅₆-7GS-mVenus, (B) IM30₂₆₋₁₅₆-7GS-mVenus, (C) IM30₂₆₋₁₃₆-7GS-mVenus, (D) IM30₁₅₇₋₂₆₇-7GS-mVenus, (E) mVenus, (F) 7GS-mVenus. The scale bar is 3 µm. All in vivo fluorescence microscopy experiments were conceived and performed in collaboration with* [redacted] *and* [redacted] *(University of Liverpool, UK).*

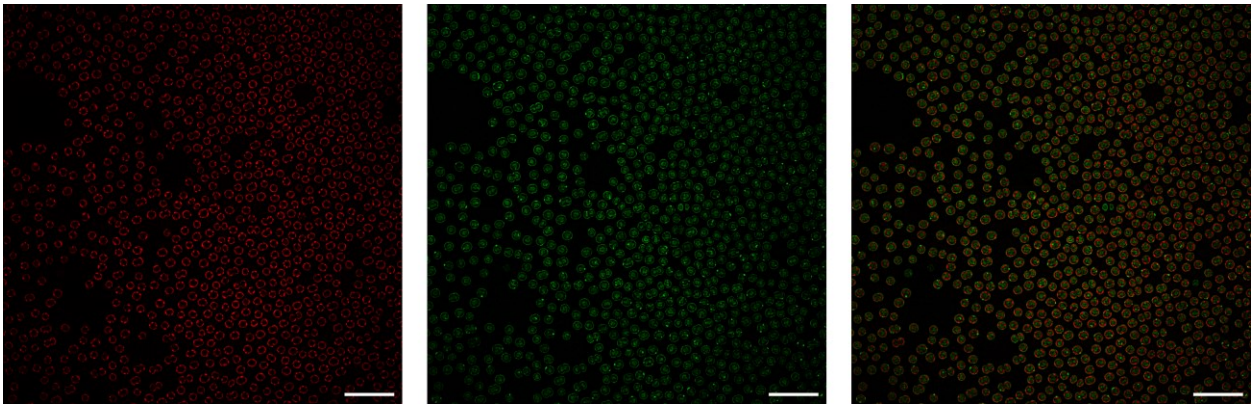

Supplementary figure 8.3-5*: Uncropped fluorescence microscopy images of Synechocystis cells expressing IM30$_{1-156}$-7GS-mVenus. Shown are the thylakoid channel in red (left), mVenus channel in green (middle) and an overlay of both channels (right) of structured illumination evaluated images (SIM^2 strong). The scale bar is 10 µm. All in vivo fluorescence microscopy experiments were conceived and performed in collaboration with [redacted] and [redacted] (University of Liverpool, UK).*

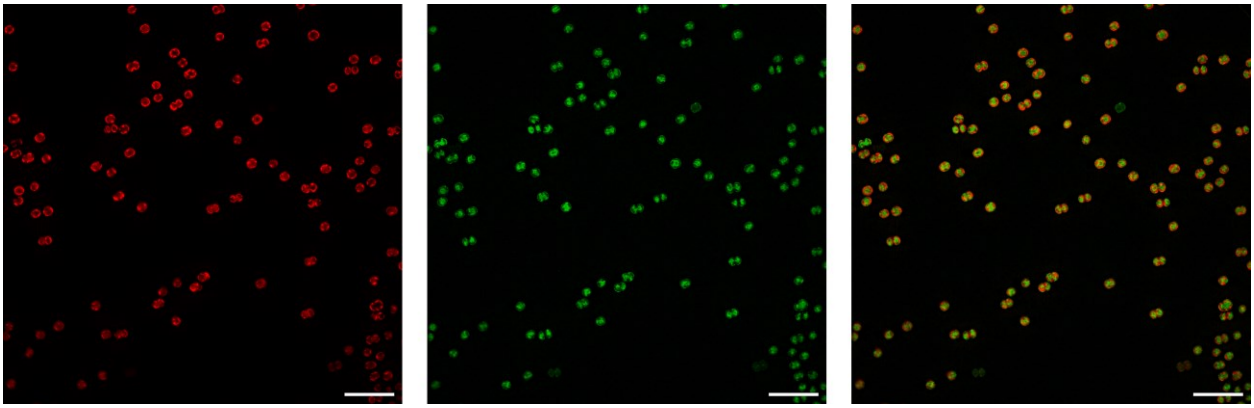

Supplementary figure 8.3-6*: Uncropped fluorescence microscopy images of Synechocystis cells expressing IM30$_{26-156}$-7GS-mVenus. Shown are the thylakoid channel in red (left), mVenus channel in green (middle) and an overlay of both channels (right) of structured illumination evaluated images (SIM^2 strong). The scale bar is 10 µm. All in vivo fluorescence microscopy experiments were conceived and performed in collaboration with [redacted] and [redacted] (University of Liverpool, UK).*

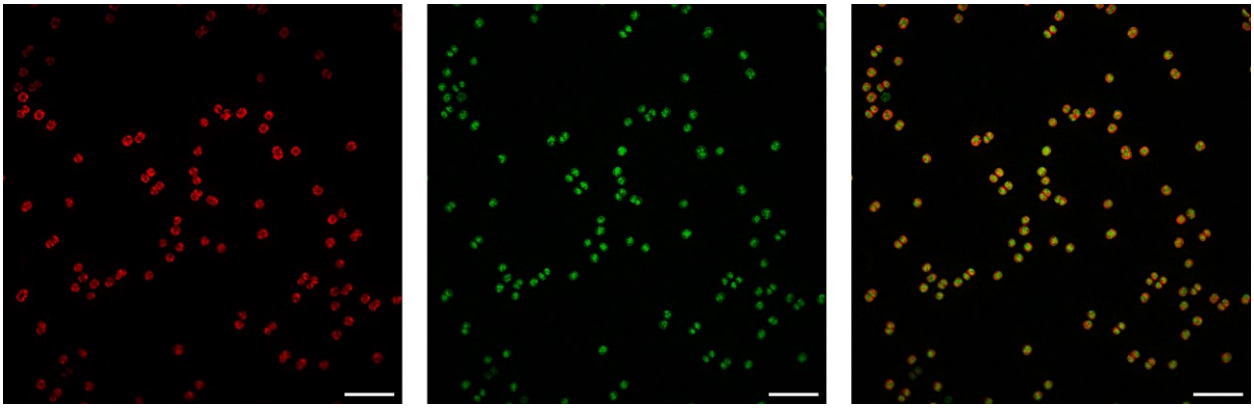

***Supplementary figure 8.3-7**: Uncropped fluorescence microscopy images of Synechocystis cells expressing IM30$_{26-136}$-7GS-mVenus. Shown are the thylakoid channel in red (left), mVenus channel in green (middle) and an overlay of both channels (right) of structured illumination evaluated images (SIM^2 strong). The scale bar is 10 µm. All in vivo fluorescence microscopy experiments were conceived and performed in collaboration with [redacted] and [redacted] (University of Liverpool, UK).*

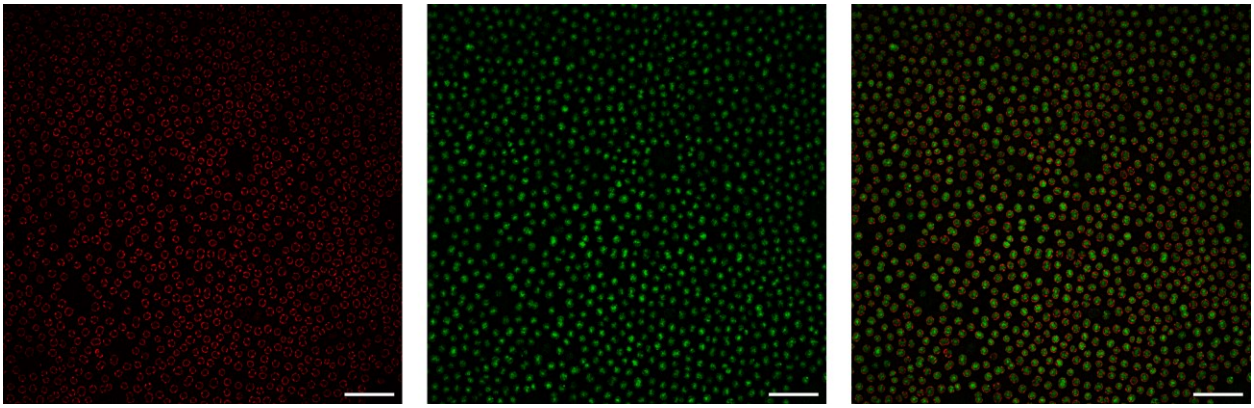

***Supplementary figure 8.3-8**: Uncropped fluorescence microscopy images of Synechocystis cells expressing IM30$_{157-267}$-7GS-mVenus. Shown are the thylakoid channel in red (left), mVenus channel in green (middle) and an overlay of both channels (right) of structured illumination evaluated images (SIM^2 strong). The scale bar is 10 µm. All in vivo fluorescence microscopy experiments were conceived and performed in collaboration with [redacted] and [redacted] (University of Liverpool, UK).*

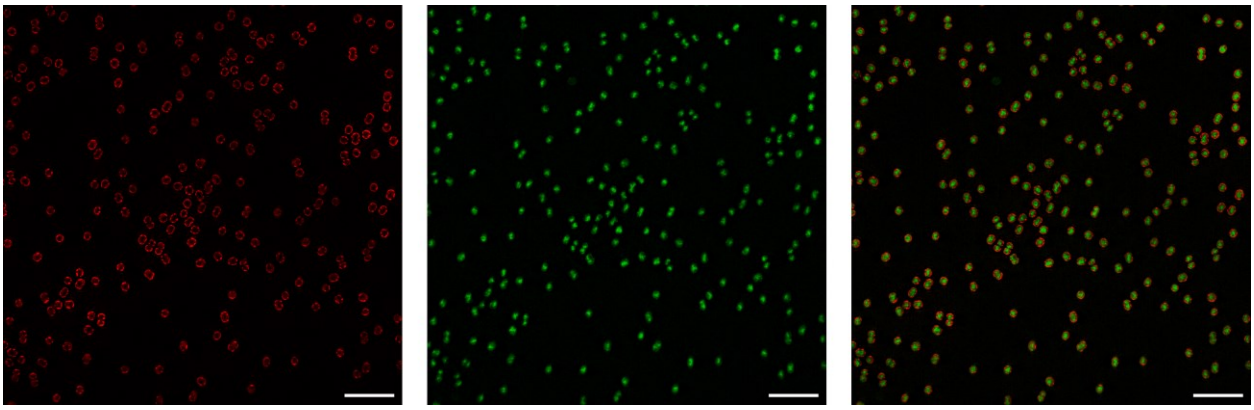

Supplementary figure 8.3-9*: Uncropped fluorescence microscopy images of Synechocystis cells expressing mVenus. Shown are the thylakoid channel in red (left), mVenus channel in green (middle) and an overlay of both channels (right) of structured illumination evaluated images (SIM² strong). The scale bar is 10 µm. All in vivo fluorescence microscopy experiments were conceived and performed in collaboration with* [redacted] *and* [redacted] *(University of Liverpool, UK).*

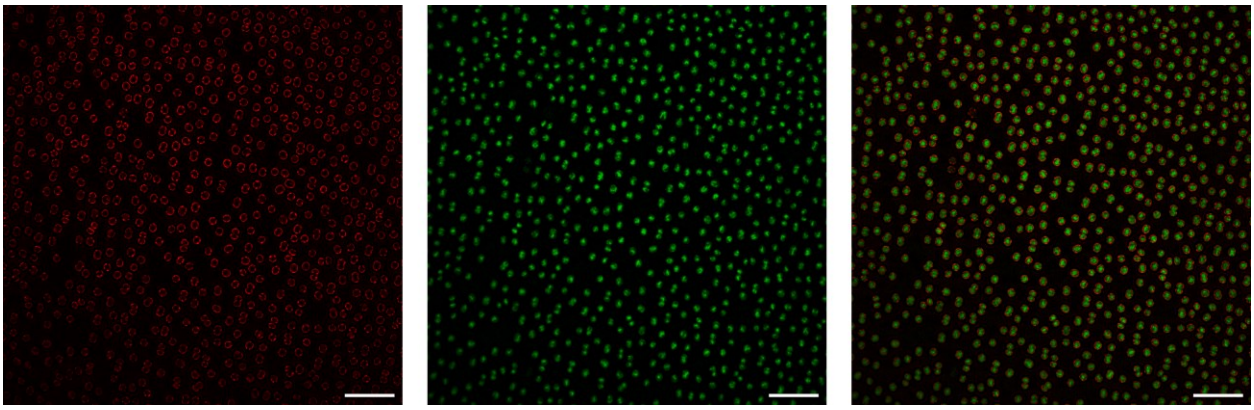

Supplementary figure 8.3-10*: Uncropped fluorescence microscopy images of Synechocystis cells expressing 7GS-mVenus. Shown are the thylakoid channel in red (left), mVenus channel in green (middle) and an overlay of both channels (right) of structured illumination evaluated images (SIM² strong). The scale bar is 10 µm. All in vivo fluorescence microscopy experiments were conceived and performed in collaboration with* [redacted] *and* [redacted] *(University of Liverpool, UK).*

9. Collaborations and author affiliations

Work that has been performed by others is indicated in the description of the figures and in the method section. Author contribution according to CRediT - Contributor Roles Taxonomy[277] is given for section 3.1 in Appendix to section 3.1.

[redacted]

Department of Chemistry – Biochemistry, Johannes Gutenberg University, Hanns-Dieter-Hüsch-Weg 17, 55128 Mainz, Germany

[redacted]

Max Planck Institute for Polymer Research, Ackermannweg 10, 55128 Mainz, Germany;

[redacted]

Institute of Molecular Physiology, Johannes Gutenberg University, 55099 Mainz, Germany

[redacted]

Department of Biochemistry and Systems Biology, University of Liverpool, L69 7ZB Liverpool, United Kingdom

Danksagung

Curriculum vitae